LUND UNIVERSITY

Magnetotransport Studies of Mn Ion-Implanted Nanowires

Paschoal, Waldomiro

2014

Link to publication

Citation for published version (APA):
Paschoal, W. (2014). *Magnetotransport Studies of Mn Ion-Implanted Nanowires*. [Doctoral Thesis (monograph), Solid State Physics].

Total number of authors:
1

General rights
Unless other specific re-use rights are stated the following general rights apply:
Copyright and moral rights for the publications made accessible in the public portal are retained by the authors and/or other copyright owners and it is a condition of accessing publications that users recognise and abide by the legal requirements associated with these rights.
• Users may download and print one copy of any publication from the public portal for the purpose of private study or research.
• You may not further distribute the material or use it for any profit-making activity or commercial gain
• You may freely distribute the URL identifying the publication in the public portal

Read more about Creative commons licenses: https://creativecommons.org/licenses/

Take down policy
If you believe that this document breaches copyright please contact us providing details, and we will remove access to the work immediately and investigate your claim.

LUND UNIVERSITY

PO Box 117
221 00 Lund
+46 46-222 00 00

Magnetotransport studies of Mn ion-implanted nanowires

Doctoral Thesis

Waldomiro Gomes Paschoal Junior

Principal Supervisor:

Prof. Håkan Pettersson

Faculty Opponent:

Dr. Jay Gupta
Ohio State University
USA

Divison of Solid State Physics
Department of Physics
Lund University
Lund, Sweden

Department of Mathematics,
Physics and Electrical Engineering
Halmstad University
Halmstad, Sweden

Department of Physics
and Electrical Engineering
Linneaus University
Kalmar, Sweden

Akademisk avhandling som för avläggande av teknisk doktorsexamen vid tekniska fakulteten vid Lunds universitet kommer att offentligen försvaras vid Fysiska institutionen, Sölvegatan 14, Hörsal B, fredagen den 4 april 2014, klockan 9.15.

Organizations
Lund University
Division of Solid State Physics
P.O. Box 118
SE-221 00, Lund

Halmstad University
Department of Mathematics, Physics and Electrical Engineering
P.O. Box 823
SE-301 18, Halmstad

Linneaus University
Department of Physics and Electrical Engineering
P.O. Box 451
SE-351 06, Växjö

Document name
Doctoral Dissertation

Date of issue
4 April, 2014

Sponsoring organization

Author(s)
Waldomiro Gomes Paschoal Junior

Title and subtitle
Magnetotransport studies of Mn ion-implanted nanowires

Abstract

This thesis focuses on the magnetotransport properties of highly Mn-doped crystalline GaAs nanowires. The GaAs nanowires were first grown by metal-organic vapor phase epitaxy from gold seed particles, and subsequently implanted with Mn ions under varying conditions, e.g., ion fluence and acceleration voltage. The implantation process was carefully analyzed and optimized within the research project. The resulting Mn-concentration in the nanowires ranges from 0.0001% to 5%. The implantation was carried out at elevated temperatures to facilitate dynamic annealing conditions at which most of the implantation-related defects are removed. After implantation, the nanowires were mechanically removed from the substrate to specially designed insulating SiO_2/Si substrates optimized for magnetotransport measurements. The single nanowires were supplied with four contacts, defined by electron-beam lithography, for accurate transport measurements.

The resistance of GaAs and GaAs: Zn nanowires was meticulously measured and analyzed in the temperature range from 300K to 1.6K, and with magnetic fields ranging from 0T to 8T. The magnetic field was applied both parallel and perpendicular to the nanowires. In addition, the magnetic properties of nanowires were probed using a superconductivity quantum interference device (SQUID) setup.

The typical resistance for a highly Mn-doped (5%) nanowire increases from a few MOhm at 300K to several GOhm at 1.6K. More specifically, the temperature-dependence of the resistance shows transport regimes described by different models. The current-voltage characteristics become strongly non-linear as the temperature decreases and shows apparent power-law behavior at low temperatures. The transport data, from 50K to 180K, are interpreted in terms of the variable range hopping (VRH) mechanism and from 180K to 300K in terms of a nearest neighbor hopping (NNH) mechanism; both occur due to the disorder in the nanowires resulting from the implantation of Mn. Below 50K, the magnetotransport data exhibit a large 40% negative magnetoresistance with the magnetic field applied either in parallel or perpendicular to the nanowire. Complementary SQUID measurements under zero-field-cooled and field-cooled conditions, recorded at low magnetic fields, exhibit clear signs of the onset of a spin-glass phase with a spin-freezing temperature of about 16K. The high magnetoresistance is explained in terms of spin-dependent hopping in a complex magnetic nanowire landscape of magnetic polarons, separated by intermediate regions of Mn-impurity spins, forming a paramagnetic/spin-glass phase. Finally, magnetotransport experiments were carried out in a series of in-situ Zn-doped (p-type) GaAs nanowires implanted with different Mn-concentrations. The nanowires with the lowest Mn-concentration exhibit a low resistance of a few kOhms at 300K and a 4% positive magnetoresistance at 1.6K, which is well described by invoking a spin-split sub-band model, unlike nanowires with the highest Mn-concentration which show a high resistance of several MOhms at 300K and a large negative magnetoresistance of 85% at 1.6K. Sweeping the magnetic field back and forth for the samples with highest Mn-concentration reveals a small hysteresis, which signals the presence of a weak ferromagnetic state. Thus, co-doping with Zn appears promising for the goal of realizing ferromagnetic GaMnAs nanowires for future nanospintronics. In summary, this thesis shows that Mn-implanted GaAs nanowires indeed represent an interesting novel type of nanometer-scale building block for miniaturized spintronic devices compatible with mainstream silicon technology.

Key words:
Nanowire, GaMnAs, ion-implantation, ferromagnetism, hopping conduction, magnetoresistance

Classification system and/or index terms (if any)

Supplementary bibliographical information:	**Language** English	
ISSN and key title	**ISBN** 978-91-7473-905-3	
Recipient's notes	**Number of pages** 182	**Price**
	Security classification	

Distribution by (name and address)

I, the undersigned, being the copyright owner of the abstract of the above-mentioned dissertation, hereby grant to all reference sources permission to publish and disseminate the abstract of the above-mentioned dissertation.

Signature: Waldomiro Gomes Paschoal Junior. **Date:** 2014-04-04

Magnetotransport studies of Mn ion-implanted nanowires

Waldomiro Gomes Paschoal Junior

Divison of Solid State Physics
Department of Physics
Lund University
Lund, Sweden

Department of Mathematics,
Physics and Electrical Engineering
Halmstad University
Halmstad, Sweden

Department of Physics
and Electrical Engineering
Linneaus University
Kalmar, Sweden

Lund, Sweden
April 2014

Copyright © Waldomiro Gomes Paschoal Junior

Division of Solid State Physics
Department of Physics
Lund University
221 00 Lund
Sweden

ISBN 978-91-7473-905-3 (for print)
ISSN 978-91-7473-906-0 (for the electronic pdf)

Printed in Sweden by Media-Tryck, Lund University
Lund 2014


In memoriam patris mei

Waldomiro Gomes Paschoal

"The beauty and clearness of the dynamical theory, which asserts heat and light to be modes of motion, is at present obscured by two clouds."

Lord Kelvin – 1900

Contents

Preface

The aim of this doctoral thesis is to summarize the magnetotransport studies on nanowires doped with manganese ions by ion-implantation, carried out for my Ph.D. project during 2008-2013 at the Division of Solid State Physics/The Nanometer Structure Consortium at Lund University, Lund, Sweden. The research work has been done in close collaboration with Halmstad University, Halmstad, Sweden, Linneaus University, Kalmar, Sweden, and Friedrich-Schiller University, Jena, Germany.

This thesis consists of seven chapters.

Chapter 1 gives a retrospect of the subject at hand, as well as the motivation and reasons for performing the research. This chapter also contains a brief introduction about the basic concepts of semiconductors, semiconductor nanowires, doping of semiconductors, disordered semiconductors and defects, and diluted magnetic semiconductors.

Chapter 2 provides a brief overview about properties of GaAs and GaMnAs semiconductor materials.

Chapter 3 reports on Mn ion-implanted GaAs nanowires of high crystalline quality doped by ion-beam implantation at high temperatures making use of in-situ dynamic annealing.

Chapter 4 describes, in detail, the nanofabrication techniques of nanodevices based on single nanowires.

Chapter 5 provides a brief description about the electrical and magnetic measurement setup.

Chapter 6 focuses on the temperature-dependent carrier transport mechanisms in Mn ion-implanted GaAs and Mn ion-implanted GaAs: Zn nanowires, specifically on two hopping mechanisms for carrier transport, namely, the nearest neighbor hopping and the variable range hopping.

Chapter 7 presents the magnetotransport studies on Mn ion-implanted GaAs and GaAs: Zn nanowires.

Acknowledgements

This thesis would not have been possible without all the brilliant colleagues and friends with whom I have had the honor to work.

First, I would like to thank my supervisors Prof. Håkan Pettersson, Prof. Lars Samuelson and Prof. Carlo M. Canali for inviting me to join the exciting research field of magnetic nanowires and for assisting me with great ideas.

I am very grateful to Father Fabrízio Meroni for believing in me and for introducing me to Carlo M. Canali and his wonderful family, Francesco Canali, Martina Canali and Susan Canali.

I gratefully acknowledge financial support from nmC@LU, Halmstad University, the Swedish Research Council (VR), the Knut and Alice Wallenberg Foundation, the Swedish National Board for Industrial, Technological Development, the Swedish Foundation for Strategic Research, the Nordforsk research network "Nanospintronics; theory and simulations", the Pará Education Secretary (SEDUC) and the Pará Government School (EGPA).

I would like to express my deepest thanks to my friend Dr. Sandeep Kumar for helping me a lot in my research and also to Dr. Ruisheng Liu for teaching me everything about nanofabrication, measurement techniques and cryogenics. Their help and guidance were very important to me. I would also like to thank Dr. Eric Hoffman, Dr. Henrik Nilsson, Dr. Marcus Larsson and Sofia Fahlvik Svensson for their help with the He_4 cryosystem.

I would like to thank all the members of the spintronics team, as well as my other collaborators, Dr. Anna Pertsova, Andreas Johannes, Prof. Carsten

Ronning, ChihHan Wang, Dr. Christian Borschel, Daniel Jacobsson, Dr. Jesper Wallentin, Kilian Mergenthaler, Dr. Kimberly Dick, Prof. Knut Deppert, Dr. Magnus Borgström, Dr. Maria Messing, Dr. MawKuen Wu and Dr Phillip Wu.

I am grateful to Prof. Anders Gustafsson, Dr. Anneli Löfgren, Dr. Claes Thelander, Dr. Dan Hessman, Prof. Heiner Linke, Dr. Jonas Johansson, Prof. Lars Montelius, Prof. Mats-Erik Pistol and Prof. Hongqi Xu for creating a great research environment at the Division of Solid State Physics. I would also like to thank the technical and administrative staff at the division for keeping everything running smoothly with their skillful support. Thanks to Aline Ribayrol, Anders Kvennefors, Bengt Bengtsson, Bengt Meuller, Dr. David Adolph, Dr. Dmitry Suyatin, Johan Stjernholm, Line Lundfald, Margareta Forsberg, Mari Lundberg, Monica Pålsson, Peter Blomqvist, Peter Ramvall, Thord Stjernholm, and special thanks to George Rydnemalm, Håkan Lapovski, Dr. Ivan Maximox, Janne Mårtensson, Lena Timby, Mariusz Graczyk, Mona Hammar and Sören Jeppesen for their close attention and care with my work. Also thanks to Leif Magnusson at Kryolab for the supplies of helium and nitrogen liquid, and his assistance regarding safety.

Thanks to all my colleagues for making the nice environment at the division. Thanks to Alexander Berg, Ali Nowzari, Anil Dey, Bahram Ganjipour, Cassandra Niman, David Göransson, David Lindgren, Fantao Meng, Fredrik Boxberg, Dr. Gabriela Conache, Gustav Nylund, Dr. Gvidas Astromskas, Dr. Jie Sun, Johannes Gooth, Karl Adolfsson, Dr. Karla Hillerich, Dr. Kristian Storm, Md Tarequzzaman, Magnus Heurlin, Mercy Lard, Dr. Mingtang Deng, Dr. Nicklas Anttu, Neimantas Vainorius, Ofogh Tizno, Reza Jafari Jam, Richard Sundberg, Stefan Holm and special thanks to my friends Chunlin yu, Guang-Yao Huang, Dr. Jason Beech, Dr. Javier Francisco Nozza Marquez, Dr. Lars-Henrik Skjolding and Vishal Jain.

I am also grateful to all my colleagues and friends outside of the Division of Solid State Physics; they made a great contribution to my life in Lund, supporting me and encouraging me in spending so long a time far away from my family. Thanks to my friends in Lund, Alan Preá, Alessandra Teixeira, Anastacia Korneva, Anna Nilsson, Camilla Persson, Carla Blomstrand Barbosa, Carolina Svensson, César Anúm, Cesar Pegado, Cleber Arruda, Danilo Lima, Eduardo Mauroy, Eduardo Miranda, Fábio Farias, Giuliano Vescovi, Gustavo Pinke, Günther Simonsson, Ian McGimpsey, Ingrid Kvelde, Irene Pala, Jean Baptiste Pouzet, João R. Almeida, Johannes Blomstrand, Jorge Luis, José Teles, Juliana Oestmann, Lawrence Nilsson, Leonardo Salinas, Luciana Villar, Padre Leonel, Luis Pegado, Luiza Lundin, Magnus Eriksson, Maria Paulina Santos, Mariana Almeida, Miguel Miranda, Nádia Parachin, Nicholas Evans, Ricardo Andrade, Rosa Aragão, Salomé Santos and Tiago Matos. Thanks to my colleagues and friends in Belém, Pará Federal University (UFPA), EGPA and SEDUC. Thanks to Adamor dos Santos, Maria Aparecida Cavalcante, Aldilene Souza, Alexandre Macêdo Jr (Grupo Remo é meu), Dir. Maria Patriarcha, Edson Cruz, GOU Maranatá-UFPA, Joel GCVS, Maria G^{ça} Rodrigues, Miríades Magrinelli, Lourdes GCVS, Orival Medeiros, Pedro Moutinho, Prof. Ângela Klautau, Prof. Edney Granhen, Prof. German Garabito, Prof. Glauber Tadaiesky Marques, Prof. Licurgo de Brito, Prof. José Bassalo, Prof. Luiz Crispino, Prof. Marcelo Lima, Prof. Paulo de Tarso, Prof. Petrus Alcântara Jr., Prof. Sergio Vizeu Pinheiro, Prof. Roberval Santos, Prof. Selma Leite, Prof. Waldeci Feio, Renildes Lima, Rubenita Gaspar, Sirley Queiroz, Socorro Coelho and Solano Reis. Thanks to my friends Adamor Marques, Anderson Ferreira, Albert Pereira, Aline Silva, Alysson Allen, Ana Barros, Ana Rocha, André Aragão, Anselmo Simões Jr., Antônio Brito Jr, Antônio Padeiro, Armindo Caldas, Bruno Rangel Costa,

César Marques, Cléa Cardoso, Charles Jean Rêgo, Claudionor Bastos nonô, Cleonildes Cardoso, Denilson Lobo, Edilson Silva Alf, Fábio Gil, Flávio Soerio, Frei Walben Monteiro, Helen Cardoso, Maria Helena Trindade, Ilda Correia, Janary Aragão, João Rodrigues, Jorge Brito, José Carlos Siqueira, Laurindinho Brasil, Marcus Duarte, Marcio Caldas, Mª Cardoso, Mª de Belém Lima, Mª do Carmo de Lima, Mª Raimunda Rodrigues, Mario Modesto Cajarana, Mauro Gonçalves, Narjara Brandão, Neyson Ferreira, Patrick Platini, Paulo Cunha, Paulo Ferreira, Pedro Queiroz, Reginaldo Calixto, Robson Gama, Sebastião de Lima, Raysa Correia, Rªi Norberto Correia, Robson Gama, Rocildo Oliveira, Ronaldo Sarmanho, Ronaldo Sarmanho Jr., Seu Raimundo Pedreiro, Telma Barros, Telma Freitas and Zuleide Silva. Special thanks to Alessandra Carvalho, Célio Costa, Celso Costa, Celton Costa, Delzira Costa, Durvalino Paschoal, Edson Lobato Bidão, Élcio Paschoal, Fernando Moller, Gabriela Carvalho, Hugo Gomes, Inete Brito, Ionete Brito, Isabela Carvalho, Ivan Brito, Ivanilson Brito, Jonatan Paschoal, Jonilton Paschoal, Kedma Paschoal, Letícia Merces, Lina Paschoal, Marcos Paschoal, Maria Ormezinda da Costa, Maria Pinheiro Miloca, Marllon Lopes, Oracildo Paschoal, Rodrigo Aragão, Rodrigo Canavieira, Titio Izaurico Brito and Ubiraci Paschoal.

I would like to thank my family. Thanks to Cleyciane Cerdeira, Izabela Paschoal, my brothers João Carlos Carvalho, Ivair Brito and my sister Walmira Paschoal Moller and and I express my deepest gratitude to my mother Maria de Nazaré and to my loving wife Carla Lima Paschoal.

Finally, I would like to thank God and the Lord Jesus for everything and for all the people mentioned above being a part of my life.

Waldomiro Gomes Paschoal Junior

Lund, April 2014

Abbreviations

1D	One-dimensional
2D	Two-dimensional
3D	Three-dimensional
AFM	Atomic force microscopy
As	Arsenic
AsH_3	Arsine
Au	Gold
BHF	Buffered hydrofluoric acid
BMP	Bound magnetic polaron
C	Carbon
DEZn	Diethylzinc
DMS	Dilute magnetic semiconductor
EB	Electron-beam
EBL	Electron beam lithography
ICP-RIE	Inductively coupled plasma reaction ion etching
IPA	Isopropanol
F	Fluor
FC	Field cooled
FCC	Face centered cubic
FET	Field-effect transistor
FFT	Fast-Fourier transformation
FIB	Focused ion beam

GaAs	Gallium arsenide
GaMnAs	Gallium manganese arsenide
GaAs: Zn	Gallium arsenide doped with zinc
GaMnAs: Zn	Gallium manganese arsenide doped with zinc
Ga	Gallium
Ge	Germanium
H_2O	Water
HCl	Hydrochloric acid
HR-TEM	High-resolution transmission electron microscopy
HV	High vacuum
IC	Integrated circuit
InP	Indium phosphide
LED	Light emitting diode
MBE	Molecular beam epitaxy
MIBK	Methyl isobutyl ketone
MIT	Metal-insulator transition
Mn	Manganese
MnAs	Manganese arsenide
MOVPE	Metal-organic vapor phase epitaxy
MR	Magnetoresistance
$(NH_4)_2S_x$	Ammonium polysulfide
NNH	Nearest neighbor hopping
NWs	Nanowires
Pd	Palladium
PMMA	Poly methyl methacrylate
RCR	Resist cleaning recipe

RKKY	Ruderman-Kittel-Kasuya-Yosida
RT	Room temperature
SEM	Scanning electron microscopy
Si	Silicon
SiF_4	Silicon tetrafluoride
SiO_x	Silicon oxide
SQUID	Superconducting quantum interference device
STEM	Scanning transmission electron microscopy
TEM	Transmission electron microscopy
Ti	Titanium
TMGa	Trimethyl gallium
UV	Ultraviolet
VRH	Variable range hopping
WZ	Wurtzite
XEDS	X-ray energy dispersive spectroscopy
ZB	Zincblende
ZFC	Zero-field cooled
Zn	Zinc

Abstract

This thesis focuses on the magnetotransport properties of highly Mn-doped crystalline GaAs nanowires. The GaAs nanowires were first grown by metal-organic vapor phase epitaxy from gold seed particles, and subsequently implanted with Mn ions under varying conditions, e.g., ion fluence and acceleration voltage. The implantation process was carefully analyzed and optimized within the research project. The resulting Mn-concentration in the nanowires ranges from 0.0001% to 5%. The implantation was carried out at elevated temperatures to facilitate dynamic annealing conditions at which most of the implantation-related defects are removed. After implantation, the nanowires were mechanically removed from the substrate to specially designed insulating SiO_2/Si substrates optimized for magnetotransport measurements. The single nanowires were supplied with four contacts, defined by electron-beam lithography, for accurate transport measurements. The resistance of GaAs and GaAs: Zn nanowires was meticulously measured and analyzed in the temperature range from 300K to 1.6K, and with magnetic fields ranging from 0T to 8T. The magnetic field was applied both parallel and perpendicular to the nanowires. In addition, the magnetic properties of nanowires were probed using a superconductivity quantum interference device (SQUID) setup. The typical resistance for a highly Mn-doped (5%) nanowire increases from a few MOhm at 300K to several GOhm at 1.6K. More specifically, the temperature-dependence of the resistance shows transport regimes described by different models. The current-voltage characteristics become strongly non-linear as the temperature decreases and shows apparent power-law behavior at low

temperatures. The transport data, from 50K to 180K, are interpreted in terms of the variable range hopping (VRH) mechanism and from 180K to 300K in terms of a nearest neighbor hopping (NNH) mechanism; both occur due to the disorder in the nanowires resulting from the implantation of Mn. Below 50K, the magnetotransport data exhibit a large 40% negative magnetoresistance with the magnetic field applied either in parallel or perpendicular to the nanowire. Complementary SQUID measurements under zero-field-cooled and field-cooled conditions, recorded at low magnetic fields, exhibit clear signs of the onset of a spin-glass phase with a spin-freezing temperature of about 16K. The high magnetoresistance is explained in terms of spin-dependent hopping in a complex magnetic nanowire landscape of magnetic polarons, separated by intermediate regions of Mn-impurity spins, forming a paramagnetic/spin-glass phase. Finally, magnetotransport experiments were carried out in a series of in-situ Zn-doped (p-type) GaAs nanowires implanted with different Mn-concentrations. The nanowires with the lowest Mn-concentration exhibit a low resistance of a few kOhms at 300K and a 4% positive magnetoresistance at 1.6K, which is well described by invoking a spin-split sub-band model, unlike nanowires with the highest Mn-concentration which show a high resistance of several MOhms at 300K and a large negative magnetoresistance of 85% at 1.6K. Sweeping the magnetic field back and forth for the samples with highest Mn-concentration reveals a small hysteresis, which signals the presence of a weak ferromagnetic state. Thus, co-doping with Zn appears promising for the goal of realizing ferromagnetic GaMnAs nanowires for future nanospintronics. In summary, this thesis shows that Mn-implanted GaAs nanowires indeed represent an interesting novel type of nanometer-scale building block for miniaturized spintronic devices compatible with mainstream silicon technology.

Populärvetenskaplig sammanfattning

Den pågående trenden att alltmer digital information skapas och lagras av ett ständigt ökande antal människor över hela världen driver på den formidabla utveckling vi idag ser av elektroniska apparater som t.ex. läsplattor, bärbara datorer och smartphones. För att möjliggöra en fortsatt utveckling i samma takt, krävs tillgång till nya typer av halvledarkomponenter och kretsar. Spinntronik är ett högaktuellt exempel som under senare år utvecklats till ett mycket intensivt forskningsområde. Det övergripande målet med denna forskning är att skapa nya typer av funktionella komponenter och kretsar som inte bara utnyttjar elektronernas laddning, utan också en annan fundamental egenskap hos elektroner som kallas spinn. I en enkel bild kan spinnet tänkas som en rotation av elektronen kring sin egen axel. Elektronen kan rotera med- eller moturs, vilket då brukar sägas svara mot spinn upp eller ned. Det finns ett naturligt samband mellan spinn och magnetism. En annan trend i modern elektronikutveckling är den fantastiska nedskalningen av komponenters storlek till en nanoskala.

Denna avhandling berör tillverkning, dopning och karakterisering av elektriska och magnetiska egenskaper hos ett av dom mest intressanta nanomaterialen för just framtidens elektronik - magnetiska nanotrådar. De nanotrådar som studeras är tillverkade av galliumarsenid i en ”bottom-up” process från små guldpartiklar som katalyserat växten av nanotrådarna. För att göra magnetiska halvledare i bulkform eller i tunna skikt, dopar/legerar man typiskt galliumarsenid med grundämnet mangan. Mangan tillför på samma gång både magnetiska moment (spinn) och laddningsbärare som förmedlar en

magnetisk koppling mellan spinnen. Tyvärr låter inte denna legeringsprocess sig göras på ett enkelt sätt i nanotrådar eftersom manganatomerna klumpar ihop sig på ett oönskat sätt. För att dopa/legera nanotrådarna med mangan har vi därför utvecklat en ny metod där manganjoner skjuts in i nanotrådarna (så kallad jon-implantering). Efter kristallväxten överförs nanotrådarna mekaniskt till ett elektronmikroskop för struktur- och sammansättningsanalys, alternativt till ett isolerat kiselsubstrat där de förses med avancerade kontakter för elektrisk och magnetisk karakterisering. Nanotrådar av hög kristallin kvalitet med upp till 5% mangan har för första gången tillverkats med denna metod. Omfattande studier har gjorts av de mekanismer som styr strömtransporten i dessa implanterade nanotrådar. Vi har demonstrerat att den dominerande transportmekanismen är olika typer av s.k. ”hopping”-processer där laddningsbärare fysiskt hoppar mellan olika diskreta lokaliserade defekter i trådarna. Denna typ av transportmekanismer är typisk för oordnade material. För nanotrådarna uppkommer denna oordning framför allt i samband med implanteringen av manganjonerna. Vi har utvecklat en modell där resistansens beroende på temperatur och magnetfält kan förstås i termer av magnetisk växelverkan mellan det pålagda magnetfältet och manganatomernas spinn, såväl som växelverkan mellan dessa spinn och spinnet hos laddningsbärarna. Den sistnämnda växelverkan resulterar i intressanta magnetiska ”bubblor” som kallas polaroner. Under inverkan av ett magnetfält uppvisar nanotrådarna typiskt en negativ magnetoresistans, d.v.s. resistansen sjunker med ökande fältstyrka. Detta fenomen har sitt ursprung i att sannolikheten för ”hopping”-processer beror på den relativa orienteringen mellan spinnet hos laddningsbärarna och manganatomernas spinn. Med ökat magnetfält linjeras dessa spinn upp, vilket ökar den effektiva rörligheten hos laddningsbärarna vilket i sin tur resulterar i en lägre resistans. En maximal negativ

magnetoresistans på cirka 85% har uppmätts vid låga temperaturer och höga magnetfält. De magnetiska trådar som studerats här har inte tillräckligt hög koncentration av laddningsbärare för att uppvisa ferromagnetism (d.v.s. att hela tråden beter sig som en magnet), framför allt beroende på defekter som skapas vid implanteringen. I den sista artikeln visar vi att implantering av mangan i nanotrådar där mängden laddningsbärare ökats genom att tillföra grundämnet zink vid växten resulterar i en svag ferromagnetism. Denna strategi lovar gott för den övergripande målsättningen med projektet att tillverka ferromagnetiska nanotrådar där en kontakt runt en nanotråd kontrollerar koncentrationen av laddningsbärare, och därmed möjliggör tillverkning av elektriskt styrda magnetiska halvledarbaserade nanostrukturer kompatibla med kiselteknologi.

List of papers

I. A New Route Toward Semiconductor Nanospintronics: Highly Mn-Doped GaAs Nanowires Realized by Ion-Implantation under Dynamic Annealing Conditions

Christian Borschel, Maria E. Messing, Magnus T. Borgström, **Waldomiro Paschoal, Jr**., Jesper Wallentin, Sandeep Kumar, Kilian Mergenthaler, Knut Deppert, Carlo M. Canali, Håkan Pettersson, Lars Samuelson, and Carsten Ronning.

Nano Letters, 11, 3935, **2011**.

I fabricated the nanodevices and performed the magnetotransport measurements. I participated in discussions and wrote the experimental part in the paper related to magnetotransport measurements.

II. Hopping Conduction in Mn Ion-Implanted GaAs Nanowires

Waldomiro Paschoal, Jr., Sandeep Kumar, Christian Borschel, Phillip Wu, Carlo M. Canali, Carsten Ronning, Lars Samuelson, and Håkan Pettersson.

Nano Letters, 12, 4838, **2012**.

I fabricated the nanodevices and performed the temperature-dependent transport measurements and conducted data analysis. I participated in discussions and in the writing of the paper.

III. Thermoelectric Characterization of Electronic Properties of GaMnAs Nanowires

Phillip M.Wu, **Waldomiro Paschoal Jr.**, Sandeep Kumar, Christian Borschel, Carsten Ronning, Carlo M. Canali, Lars Samuelson, Håkan Pettersson, and Heiner Linke.

Journal of Nanotechnology, 2012, 480813, **2012**.

I fabricated the nanodevices and performed the data analysis. I took part in discussions and in the writing of the paper.

IV. Magnetic Polarons and Large Negative Magnetoresistance in GaAs Nanowires Implanted with Mn Ions

Sandeep Kumar, **Waldomiro Paschoal, Jr.**, Andreas Johannes, Daniel Jacobsson, Christian Borschel, Anna Pertsova, Chih-Han Wang, Maw-Kuen Wu, Carlo M. Canali, Carsten Ronning, Lars Samuelson, and Håkan Pettersson

Nano Letters, 13, 5079, **2013**.

I fabricated the nanodevices and performed the temperature-dependent magnetotransport measurements, and I did the data analysis and development of the transport model. I took a lead part in discussions and in the writing of the paper.

V. Magnetoresistance in Mn ion-implanted GaAs: Zn nanowires

Waldomiro Paschoal Jr, Sandeep Kumar, D. Jacobsson, A. Johannes, V. Jain, C. M. Canali, C. Ronning, K. A. Dick, L. Samuelson and H. Pettersson

Submitted to Applied Physics Letters, February **2014**.

I fabricated the nanodevices and performed the magnetotransport measurements and conducted data analysis. I took a lead part in discussions and in the writing of the paper.

Chapter 1

Introduction

Nowadays, due to the popularization of personal electronic devices, e.g., tablets, notebooks, netbooks, ultrabooks, smartphones, etc., there is a rapid, sharp increase in the digital information being created, accessed, collected, and stored by many people worldwide. This fast and vast increase does not exhibit any sign of slowing down. If the processing power that leads this data creation obeys the exponential increase per year and if the storage density that drives data storage also follows the exponential increase per year [1], then the abrupt increase of the popularization of digital information can be a function of these two exponential tendencies. This popularization of ever-growing streams of digital information generates the constant quest to fabricate the smallest and most novel semiconductor materials that can keep up with such a demand.

This doctoral thesis deals with a very interesting new class of nanoscale materials that has been proposed for novel electronic devices and circuits – dilute magnetic semiconductor nanowires (NWs), and in particular, GaAs NWs doped with magnetic Mn ions by ion-implantation. More specifically, there are three main motivations behind the choice of this thesis project [2 - 6]. The first is, when semiconductor structures decrease in dimension from a micrometer scale, so-called bulk, to a few nanometers, so-called nanostructures such as NWs, their properties may drastically change [7 - 9] and new physical effects may occur in them [10, 11]. At the same time, these different properties and new physical effects permit the fabrication of novel nanoscale devices [12] and

new technology applications [13]. For example, if one million NWs were compacted together, their thickness would be something like a hair. Currently, semiconductor NWs are of great interest as versatile building blocks of high functionality for various devices [14], and their small footprint facilitates their direct growth on silicon substrates.

The second motivation is that, in bulk (3D) or as thin-films (2D), Mn-doped GaAs semiconductor materials typically exhibit ferromagnetic ordering when they are grown by non-equilibrium growth techniques such as low-temperature molecular beam epitaxy (MBE) [15]. These materials have generated immense interest in nanotechnology research, e.g., for the fabrication of novel spin-sensitive devices (spintronics), regarding the possibility of interplay between two fundamental physical quantities: the elementary magnetic moment, the so-called spin, as well as the charge of the carriers. Mn ions being substitutionally incorporated on Ga sites in the GaAs semiconductor crystal are responsible for uncompensated spins and also act as acceptors providing holes that mediate a ferromagnetic coupling between the spins; this is the basic concept of dilute magnetic semiconductors DMSs [16, 17].

Realizing magnetic NWs is fundamentally interesting due to the expected new physical effects connected to their quasi-1D character. Unfortunately, it turns out that it is extremely difficult to grow high-quality DMS GaMnAs NWs with standard gas phase or MBE techniques, even by non-equilibrium growth using low-temperature MBE, due to the low solubility limits of 3d-transition metals in III-V semiconductors. This is because the growth of semiconductor NWs necessitates significantly higher temperatures than the low-temperature MBE of thin-films.

In the literature, there are several attempts and different approaches to create high-quality DMS GaMnAs NWs [18 - 29], but MnAs phase segregation

during growth was the main problem with most of the reported approaches. This phase segregation (low solubility limit) can be understood from the phase diagram discussed by Ohno, for a $Ga_{1-x}Mn_xAs$ thin-film grown by MBE, where MnAs is formed at growth temperatures already above 300^{o}C, for x between 0.5% – 6% [30]. Thus, the question of how to incorporate Mn ions into GaAs NWs during growth, or in a post-growth diffusion process, is still open in the semiconductor industry.

One possibility of attaining DMS GaMnAs NWs would be an ion-beam implantation method. Such an approach is frequently utilized at lower processing temperatures, and it can be carried out to add any ion into any semiconductor material with virtually any solubility limit [1]; however, due to the high ion-implantation energies, defects are created in the semiconductor materials, and then annealing processes are frequently necessary post-implantation [31 - 33] or during implantation [2, 6]. Annealing processes have also exhibited good results in the introduction of Mn ions in GaAs (bulk and thin-film) for the fabrication of DMSs [34]. The annealing processes of bulk materials and thin-films cannot be completely applied in most cases of nanowire semiconductors, due to the small volume of semiconductor nanowires which tend to reduce the melting points to values lower than those of bulk or thin-film semiconductors. Recently, our research team has reported great results of the incorporation of Mn ions in GaAs NWs after growth by an ion-beam implantation method invoked at elevated temperatures to facilitate in-situ dynamic annealing processes [2 - 6, 35, 36].

Finally, the third motivation behind this thesis is that NWs can be monolithically integrated with silicon substrates due to their small footprint. GaAs NWs implanted with Mn ions therefore represent an eminent and

interesting novel type of nanometer-scale building block for miniaturized spintronic devices compatible with mainstream silicon technology.

This thesis describes a detailed study of the temperature-dependence and the magnetic field-dependence of different carrier transport mechanisms in single Mn ion-implanted GaAs NWs.

This first introduction chapter describes some basic concepts of semiconductors and semiconductor nanowires, doping of semiconductors, disordered semiconductors, and diluted magnetic semiconductors.

1.1 Basic concepts of semiconductors

In general, solid materials can exist in disordered (e.g. amorphous) or ordered (crystalline) forms. Amorphous materials have only short-range order within a length scale of a few atoms or molecules, while crystalline materials (crystals), ideally, have a regular geometric periodicity of the atoms or molecules throughout their entire volume. The atomic or molecular order within a solid material determines many of the physical properties, such as, optical, thermal, electrical and magnetic properties. An advantage of crystals is that, usually, their electrical properties are superior to those of non-crystalline materials. Solid materials can be grouped into three classes depending on their electrical conductivity: insulators, semiconductors, and conductors. The insulators are materials with low electrical conductivity. Semiconductors are a class of materials exhibiting an electrical conductivity in-between the insulators and highly-conductive conductors. At sufficiently low temperatures, pure semiconductors act as insulators. The electrical conductivity of a semiconductor is usually sensitive to temperature, magnetic field, and impurity concentration (doping). The possibility to tailor the electrical conductivity by

doping is the key property that makes semiconductors the most relevant materials for electronics.

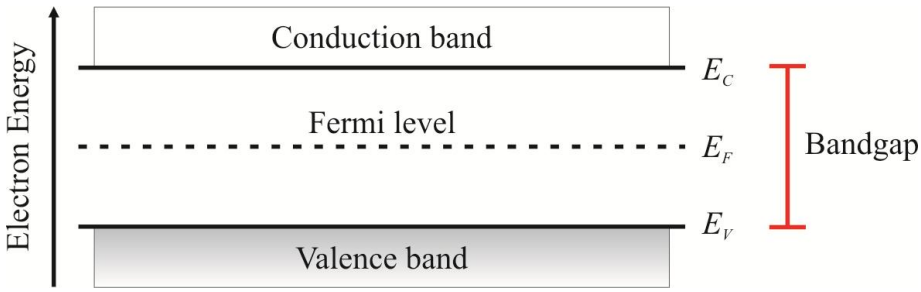

Figure 1.1: Schematics of the band structure of a pure semiconductor. E_F is the Fermi level.

In a semiconductor, the periodicity and the interaction of the atoms generate closely separated energy states, structured in energy bands. Between the energy bands, there is an energy interval in which electronic states are not allowed, the so-called bandgap. The states below the bandgap form the valence band and they are completely occupied by electrons at low temperatures, while the states above the bandgap are empty and form the conduction band (Figure 1.1). In semiconductors, where the bandgap is small enough, the electrons can gain sufficient energy to move up into the conduction band where they are free to move. This process, in which a free hole is left behind in the valence band, physically means that a crystal bond is broken in the crystal. Therefore, in semiconductors, electrical current is provided by free electrons in the conduction band and free holes in the valence band driven by an external electric field [37].

Semiconductor materials can usually be classified as elemental semiconductor materials or compound semiconductor materials. The elemental materials are composed of single atoms from group IV of the Periodic Table, such as Si and Ge. Si is by far the most used material for semiconductor

devices. The binary compounds are often formed of elements from groups III and V of the Periodic Table, the so-called III-V semiconductors, for example, GaAs and InP. GaAs is extensively studied in this doctoral thesis. For spintronic applications, the ternary compound semiconductor $Ga_{1-x}Mn_xAs$ is most widely used, where x is the fraction of Mn atoms occupying group III (Ga) sites. [38].

1.2 Semiconductor nanowires

Semiconductor NWs are thin semiconductor fibers with a typical length of a few micrometers and with diameters in a range from a few nanometers to hundreds of nanometers. Thin NWs, with a diameter comparable to the Fermi wavelength of electrons, behave as one-dimensional (1D) structures exhibiting strong quantum confinement effects. The semiconductor NWs studied in this thesis are made by a highly-controllable bottom-up technique by self-organized growth atom by atom. The resulting excellent crystalline structure quality leads to semiconductor NWs being used as nanodevices [39 - 44] and has generated great interest in the nanotechnology industry.

As previously mentioned, only Mn-doped GaAs NWs are studied in detail in this thesis. The GaAs NWs were grown by so-called metal-organic vapor phase epitaxy (MOVPE). Presently, MOVPE is the most important epitaxial growth technique to grow III-V semiconductor NWs for industry, with device applications such as solar cells, blue laser diodes and high-speed transistors. MOVPE uses metal-organic growth precursors. Metal seed particles are often utilized as a catalyst for the NW growth, though there are also particle-free growth modes [45]. Gold (Au) particles are the most commonly used metal seed particles [46 - 48], but other metal seed particles can also be used to grow NWs [49].

In this thesis, GaAs NWs are grown from Au particles. The Au particles are seeded on the surface of a GaAs substrate by an aerosol technique [50]. The GaAs substrate with Au-seeding is placed into the MOVPE system. When the substrate is heated up to the growth temperature, the Au particles melt and form an eutectic supersaturated alloy with the substrate. Injection of growth gases into the MOVPE system commences the NW growth (Figure 1.2).

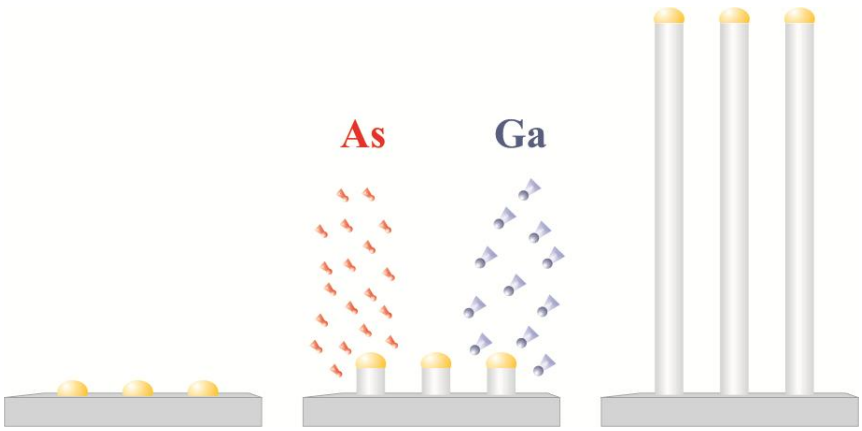

Figure 1.2: Growth process of NWs. Au particles are first seeded on a semiconductor substrate. Subsequent transfer of substrate to growth chamber and injection of precursor molecules under well-defined conditions (e.g. partial pressure and temperature), leads to crystal growth catalyzed by the Au particles.

MOVPE processes occur at low pressures with an inert carrier gas containing the precursor molecules flowing over the heated substrate [51]. For the growth of GaAs NWs, TMGa and AsH_3 are used as precursors. The GaAs NWs are usually grown in a temperature range of 350 ^{o}C – 550 ^{o}C.

1.3 Doping of semiconductors

A particular characteristic of semiconductors is that the electrical conductivity can be altered and controlled by introducing impurities into a pure semiconductor. The method of introducing impurity atoms to a semiconductor material is called doping. The doping controls the amount of free carriers in the bands available for transport and thus the electrical conductivity. The possibility to tailor the conductivity and the type of charge carriers, in a semiconductor, are the reasons why semiconductors are superior materials for the semiconductor industry, providing the basis for fundamentally important devices such as diodes, transistors [12], LEDs, sensors [43, 44], solar cells [13, 52], photodetectors and novel nanodevices.

Depending on the type of impurities (dopants), electronic impurity states are formed in the energy bandgap near the conduction band or valence band, respectively (see Figure 1.3). The two different types of dopants are referred to as donors and acceptors. Donors typically introduce energy states near the conduction band edge and provide electrons to the conduction band. The semiconductor material is then called *n*-type, where *n* denotes negatively-charged carriers. In contrast, acceptors introduce energy states near the valence band edge and accept electrons from the valence band, leaving behind holes in the valence band. In this case the semiconductor is called p-type, where *p* denotes positively-charged carriers. The Fermi-level is a reference level that basically states the energy position of the top-most filled energy states. In an n-type material the Fermi-level is close to the conduction band, whereas it comes close to the valence band for a p-type material. For an undoped material, referred to as an intrinsic material, the Fermi level is in the middle of the bandgap. In addition, dopants can be classified as deep or shallow dopants. The deep dopants have their energy states situated deep in the bandgap, while the

impurities are shallow if their energy states are very near to one of the energy band edges as discussed above and shown in Figure 1.3. This introduction of electrons and holes is an important issue in semiconductor nanomaterials fabrication [53], where devices soon can be realized where a single dopant atom is hosted in a device – such exotic devices are referred to as solotronics.

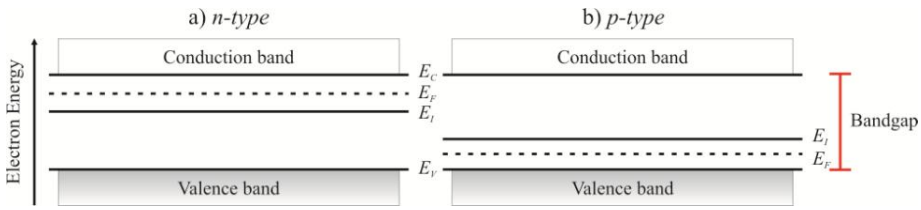

Figure 1.3: Schematic band structure of doped semiconductors. The solid lines in the bandgap represent impurity states which are located near to the band edges: a) *n*-type semiconductor, where donor states are near to the conduction band edge and b) *p*-type semiconductors, where acceptor states are near to the valence band edge.

As mentioned above, the electrical properties of a semiconductor material can be profitably modified by well-controlled incorporation of specific impurity atoms. There are two methods of doping: diffusion and ion-implantation. Diffusion and ion-implantation can be complementary to each other for doping. Diffusion is a method frequently used at high temperature and in so-called deep-junction processing, whereas the ion-implantation method is utilized for lower temperature shallow-junction processing [1, 38].

In general, the diffusion process depends on the semiconductor material, type of impurity (introduced in gaseous form) and temperature. Due to the elevated temperature, the impurity atoms can randomly move through the crystal to find energetically favorable substitutional, or interstitial, lattice sites to occupy. Using proper masking techniques, the diffusion method can control the doping in specific areas only of a semiconductor, thereby allowing the

fabrication of large numbers of different devices on a single semiconductor substrate.

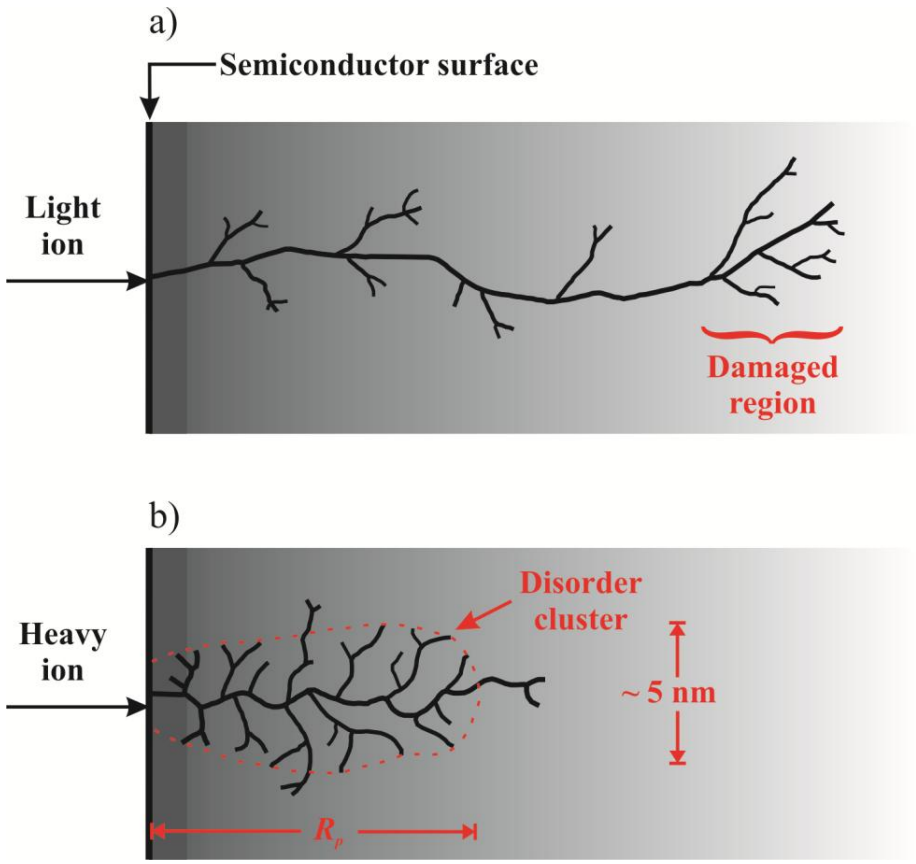

Figure 1.4: Implantation disorder caused by (a) light ions and (b) heavy ions. *Rp* is the projected range [1, 54, 55].

The ion-implantation method is usually carried out at a lower temperature than diffusion. A beam of impurity ions is accelerated in the direction of the surface of the semiconductor, and the implantation energies are between 1 keV to 1 MeV. One advantage of the ion-implantation method is that

controlled quantities of impurity ions can be added to selected areas of the semiconductor. One pertinent disadvantage of the ion-implantation method is that the incident high-energetic ions collide with the atoms of the semiconductor, resulting in several damaged areas and defects (see Section 1.4) in the crystalline structure (Figure 1.4) [1]. However, most defects and damage in the crystalline structure can be removed by thermal annealing. Chapter 3 in this thesis presents the approaches to dope GaAs NWs with Zn atoms by the diffusion method, as well as doping NWs with Mn using the ion-implantation method.

1.4 Disordered semiconductors

A disordered semiconductor in a general sense means that the ordering of the crystal structure is disrupted by the presence of defects. Common defects in semiconductors include, for example, antisites, vacancies, interstitial impurities, line dislocations, and impurities. Defects tend to modify the electrical properties of the semiconductor material, as previously described in the doping cases, where electrical conductivity can be controlled by impurities.

Common types of defects are the vacancies, which are lacking atoms in the semiconductor. In forming semiconductor materials, other defects can appear; for example, a line defect arises when a row of atoms is lacking from their regular crystalline structure, a so-called line dislocation. Impurity atoms exist both as unintentional, i.e. incorporated contaminations during growth, or intentionally added as dopants as discussed above. Impurity atoms situated exactly at regular sites in the crystalline structure are called, substitutional impurities. Impurity atoms situated between regular sites in the crystalline structure are called, interstitial impurities. All defects described here are schematically shown in Figure 1.4 [38].

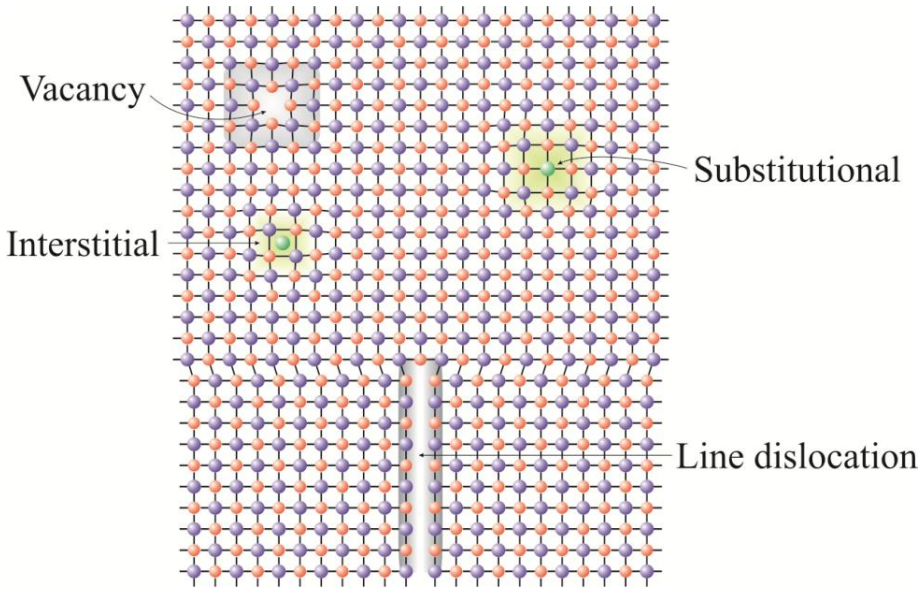

Figure 1.5: Two-dimensional schematics of a GaAs crystalline structure showing a vacancy defect, an interstitial Mn impurity, a substitutional Mn impurity and a line dislocation.

Vacancies, interstitial defects and line dislocations perturb the regular geometric periodicity of the crystalline structure and the atomic bonds in the crystal. The dislocation defects can alter the electrical properties of the material more strongly than the point defects. Other types of disorder can also exist in a semiconductor, for example, stacking faults, twins, grain boundaries, precipitates and voids, though the focus of this introduction only presents the basic types of defects [38]. The physical implications of disorder in NWs is one main focus of this thesis and it is discussed at length in Chapter 6.

1.5 Dilute magnetic semiconductors

Dilute magnetic semiconductors (DMSs) are a type of compound semiconductors, e.g. GaAs, in which a determined quantity of non-magnetic group III atoms (cations) are randomly substituted by magnetic atoms, thus inserting local magnetic moments (spins) in the compound semiconductor (Figure 1.6). These spins originate from 3d-transition metals or 4f-rare earth elements of the Periodic Table. The most common magnetic element used for DMSs is Mn, but also other elements like Cr and Fe have been utilized [56, 57].

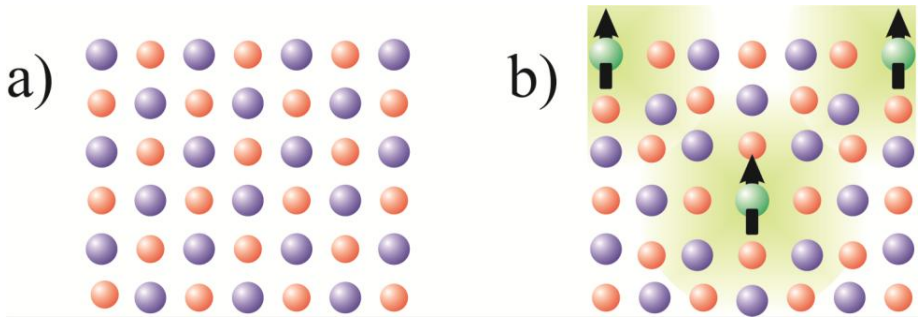

Figure 1.6: Two-dimensional schematics of a) a non-magnetic GaAs crystal and b) a DMS GaMnAs crystal where some Ga atoms have been replaced by Mn atoms.

DMSs can show a vast range of magnetic properties, from paramagnetism and spin-glass behavior to ferromagnetism [58]. They can span a wide conductivity range from insulator to metal. The ordered ferromagnetic phase in DMSs is generated due to an effective exchange interaction between the localized spins of the magnetic atoms mediated by free charge carriers (electrons or holes). The exchange interaction strongly influences the temperature-dependence and the magnetic field-dependence of the electrical properties of the magnetic semiconductors. For example, in high magnetic

fields and below the critical temperature for ferromagnetic ordering, the so-called Curie temperature (T_C), ferromagnetic semiconductors exhibit a band splitting where spin-up and spin-down sub-bands are generated. [59]. Moreover, at T_C, the resistivity typically shows a peak, which disappears in strong magnetic fields for samples exhibiting a large negative magnetoresistance [60 - 63]. Chapter 7 discusses magnetoresistance effects in GaMnAs NWs.

Chapter 2

Electronic properties of GaMnAs

The main focus of this thesis deals with fabrication and characterization of Mn-implanted GaAs NWs, with the goal of realizing ferromagnetic NWs. This chapter first provides a brief description of fundamental electronic properties of GaAs. Next, alloying GaAs with Mn is discussed with an emphasis on the physical coupling mechanisms responsible for the ferromagnetic interactions present in GaMnAs.

2.1 Fundamentals of GaAs

Gallium arsenide (GaAs) is a compound semiconductor of two elements, gallium and arsenic, from the groups III and V, respectively. GaAs is technically an important semiconductor material for high-speed and optical devices, as for example, diodes, FETs, LEDs, and lasers which are used in optical communication and control systems. So, GaAs is a very important substitute for silicon in the fabrication of digital ICs. It is also of paramount importance for fabrication of optical devices, since silicon is a very poor emitter of electromagnetic radiation due to its indirect bandgap. One drawback of GaAs-based devices is the relatively high cost of the (GaAs) substrates. Interesting approaches to circumvent this problem are fabrication of GaAs (or other III-V) devices on cheaper substrates, e.g. silicon, using wafer bonding techniques or direct epitaxial growth. Such alternatives are in line with the well-known *"More than Moore"* concept.

Crystalline bulk GaAs has the well-known zincblende structure, similar to the diamond structure, where Ga and As atoms occupy two displaced face-centered cubic lattices (fccs), respectively (see Figure 2.1). The lattice constant (a) of the conventional unit cell is 0.5653 nm. The electron configurations for Ga and As are [Ar] $3d^{10}$ $4s^2$ $4p^1$ and [Ar] $3d^{10}$ $4s^2$ $4p^3$, respectively [64]. The crystal bonds have both covalent and ionic bond character. Some important electronic parameters of bulk GaAs at 300K include: a direct bandgap of 1.42 eV (at the Γ point in Figure 2.2), mobilities of around 8500 $cm^2/(V \cdot s)$ and 400 $cm^2/(V \cdot s)$ for electrons and holes, respectively, a static dielectric constant of about 12.9, and effective masses of $0.063m_o$ and $0.51m_o$, for electrons and (heavy) holes, respectively [64, 65].

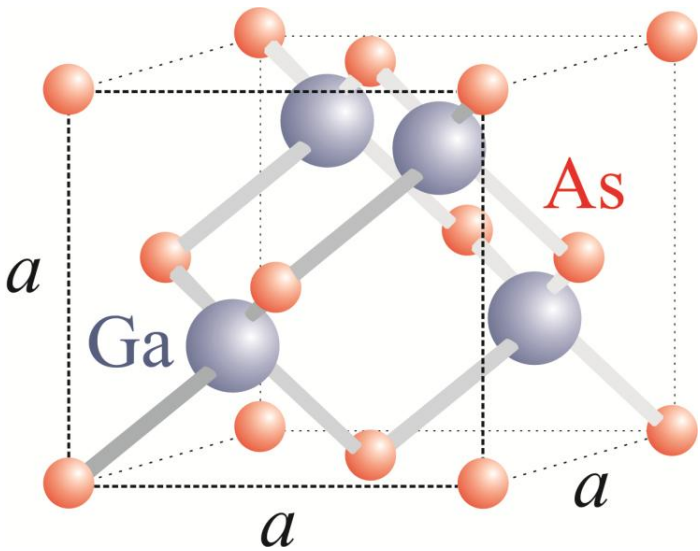

Figure 2.1: The zincblende structure of GaAs.

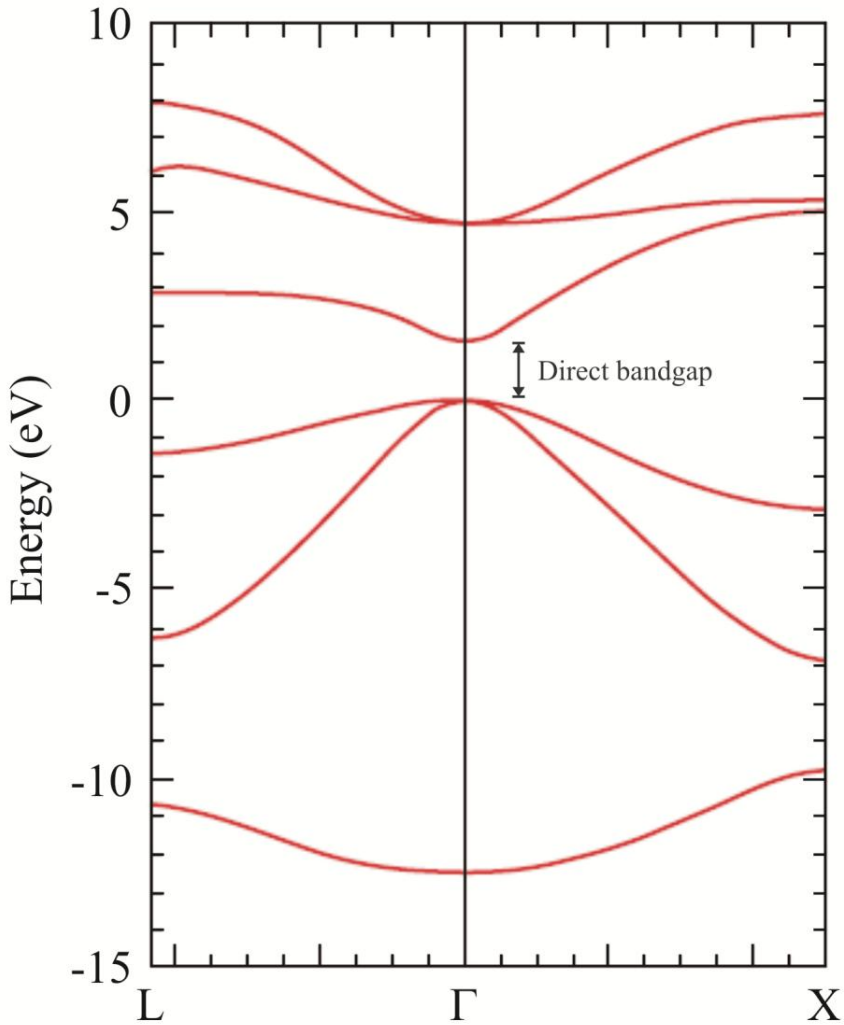

Figure 2.2: Electronic band structure of GaAs[66]. The fundamental bandgap is direct, i.e., without any mismatch in momentum of holes in the valence band and electrons in the conduction band.

Today, there are a lot of research activities to fabricate GaAs nanostructures/devices in general and nanowires in particular. In this thesis, all

experimental work was performed on GaAs NWs. The NWs were grown by MOVPE (see Section 1.2) from Au seed particles deposited on GaAs (111) B substrates by an aerosol technique. The diameter of the gold particles basically determines the diameter of the grown NWs. [47]. In this thesis, NWs with diameters in the range 40nm-80nm were investigated.

2.2 Fundamentals of magnetic GaMnAs

Currently, GaMnAs is the most extensively investigated III-V DMS material and the best understood magnetic semiconductor. In the ideal case, Mn (electron configuration [Ar] $3d^5$ $4s^2$) doping of GaAs results in Mn^{2+} ions replacing substitutional Ga^{3+} ions in the GaAs crystal (Figure 2.3). Since a Mn^{2+} ion has a negative charge relative to the cation sub-lattice, it can bind a hole thus acting as an acceptor in the crystal. The hole binding energy is energetically situated about 110 meV above the valence band edge. In contrast to conventional acceptors used for p-type doping, Mn^{2+} has a half-filled d-shell which results in a local spin of 5/2. Moreover, the holes provided by the Mn acceptors couple anti-ferromagnetically to the localized 5/2 spins, which thus results in an effective ferromagnetic coupling between the 5/2 spins mediated by the holes. This interaction is referred to as the Rudermann-Kittel-Kasuya-Yosida (RKKY) interaction [67]. The main open issue regarding the origin of hole-mediated ferromagnetism in GaMnAs is if the carriers reside in the valence band of the host or if they form a narrow impurity band in the band gap. Evidence for both mechanisms has been claimed, making a consensus difficult [61]. Ferromagnetism in GaMnAs induced by holes requires a typical hole concentration of > 1%. The critical temperature for ferromagnetic ordering, the so-called Curie temperature T_C, grows with the hole concentration. To obtain a high T_C thus requires a very high Mn-concentration.

Unfortunately, there are severe limiting factors preventing an ideal incorporation of high concentrations of substitutional Mn in GaAs. One complicating fact is that transition metals (e.g. Mn) as dopants show a very low solubility in GaAs when they are grown by standard procedures.

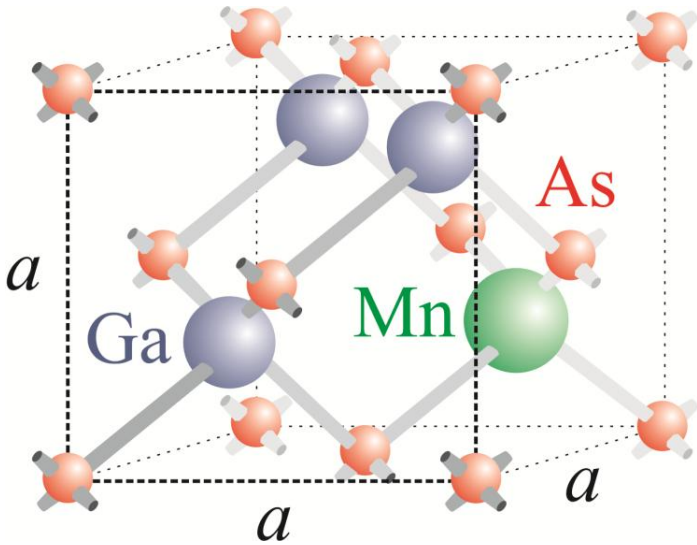

Figure 2.3: The zincblende structure of GaMnAs with a Mn atom replacing a Ga atom.

A phase diagram of GaMnAs (Figure 2.4) [30] shows the effects of growth temperature. Mn-concentrations between 0.1% and 10% have been frequently investigated and shown to result in critical temperatures (T_C) between 10K and 173K [68]. Another complication at high Mn-concentrations is that undesired defects, e.g., interstitial Mn, form in the crystal which act as double donors compensating the holes provided by the substitutional Mn dopants. Despite the fact that the obtained Curie temperatures are still far below what is necessary for room temperature applications, GaMnAs is an important model system for III-V diluted magnetic semiconductors.

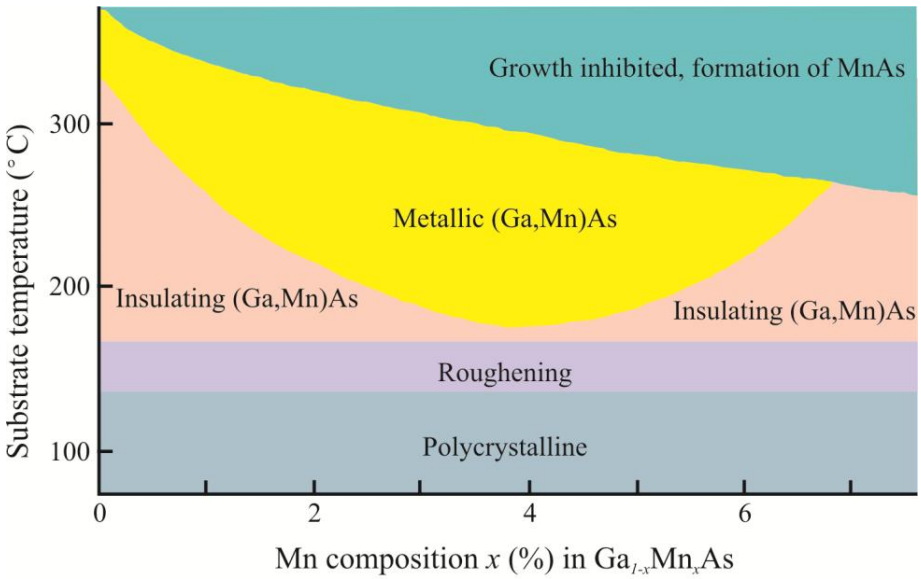

Figure 2.4: Schematic phase diagram showing the relation between growth parameters (substrate temperature and Mn-concentration) and the properties of (Ga,Mn)As grown by molecular beam epitaxy [30].

As mentioned above, Mn ions in the low concentration range ideally form acceptor levels with an ionization energy of 110 meV above the valence band edge [69]. A further increase of the Mn-concentration forms an impurity band that eventually overlaps the valence band. The further widening of the impurity band leads to a significant mixing of localized impurity levels with delocalized valence band levels..

Chapter 3

GaMnAs nanowires

To grow highly Mn-doped crystalline GaAs NWs is tremendously difficult due to the segregation effects already mentioned. We have therefore developed a novel technique based on implantation of Mn ions in as-grown GaAs NWs. In order to investigate the effects of Mn implantation on the crystal quality it is important to characterize their structure by transmission electron microscopy before and after implantation. Firstly, in this chapter, the ion-beam implantation method is described. Secondly, TEM characterization of Mn ion-implanted GaAs and GaAs: Zn NWs is summarized. The ion-implantation experiments described in this chapter were performed by the team of Prof. Dr. Carsten Ronning and Dr Christian Borschel at the Friedrich-Schiller-University in Jena, Germany. More details can be found in [2, 36].

3.1 Ion-beam implantation method

For the ion-implantation experiments in this thesis, the NWs were irradiated with Mn ions using a general purpose implanter, at the Friedrich-Schiller-University in Jena, Germany. The implanter supplies an unfocused broad beam, which can homogeneously implant large areas of some cm^2 and the targets can be heated to several hundred ^oC during implantation to facilitate a dynamic annealing of the samples.

The single-crystalline GaAs NWs of about 1.5µm – 2µm length were grown by MOVPE using mono-disperse Au seed particles as catalysts [47]. The latter were deposited by an aerosol technique [70] with an areal density of 0.6 μm^{-2} and diameters in the range of 20 – 80 nm onto GaAs ⟨111⟩ substrates leading to a perpendicular growth direction relative to the substrate. The GaAs NWs were grown at a temperature of 550°C with TMGa and AsH_3 as precursors. Prior to nucleation of the NWs, the epi-ready substrate was annealed in-situ at 650°C in an AsH_3/H_2 atmosphere to remove surface oxides. The NWs were grown with an initial nucleation step at 440°C for 1min. After the nucleation step, the supply of TMGa was closed and the temperature was reduced to the growth temperature (400°C), and after thermal stabilization the precursors were introduced to initiate a growth period of 15min [71]. Figure 3.1 (a) shows SEM images of grown single-crystalline GaAs NWs.

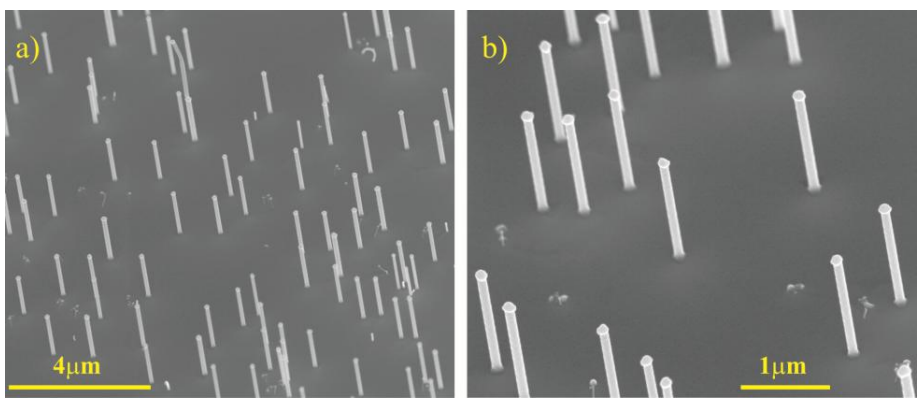

Figure 3.1: 45°-tilted SEM images of a) as-grown non-implanted GaAs NWs and b) GaAs NWs after Mn-implantation.

In order to obtain single-crystalline Zn doped *p*-type GaAs NWs, the growth method follows the same previous growth steps, but after thermal

stabilization, TMGa and AsH_3 were reintroduced together with DEZn and HCl, to commence the growth of GaAs: Zn NWs. The total growth time was 30min, after which the sample was cooled down in an AsH_3/H_2 atmosphere [6]. The Zn-concentration estimated from growth parameters, and from subsequent resistance measurements, is about ~ 10^{19} cm^{-3} [72].

The single-crystalline GaAs NWs were implanted with Mn ions under an angle of 45° with respect to the NW axis with implantation energies in the range of 40 – 100 keV using a general purpose implanter. Implantation doses of 2×10^{15} to 1×10^{16} Mn ions/cm^2 resulted in nominal Mn-concentrations from 0.5% to 2.9% (corresponding to $Ga_{1-x}Mn_xAs$ with x = 1% to x = 5.8%) (Table 3.1) as calculated with our own developed *iradina* code [73]. The GaAs NWs were implanted at elevated temperatures ranging from 100°C to 350°C, which resulted in high crystalline quality of the NWs due to an efficient in-situ dynamic annealing (Figure 3.1(b)) effect. Other doping attempts, such as implantation at room temperature and subsequent annealing for 30min either in vacuum at temperatures up to 500°C, or in an AsH_3 atmosphere from 350°C to 650°C, resulted in amorphous regions in the NWs [2].

Also, the single-crystalline GaAs: Zn NWs were implanted on a rotating sample holder under an angle of 45° with respect to the NW axis with 40keV Mn ions using a general purpose implanter. The sample temperature was in this case kept at 300°C to facilitate efficient dynamic annealing during implantation. A series of GaAs: Zn NWs were implanted with three different Mn ion fluencies of 2.65×10^{11} ions/cm^2, 2.65×10^{14} ions/cm^2 and 1.32×10^{16} ions/cm^2 at 300°C, and subsequently kept at 300°C in vacuum for 12h after implantation. Results from computer simulations of the implanted ion profile using the *iradina* code imply that the present implantation conditions lead to fairly homogeneous Mn-concentrations of x = 0.0001%, 0.1% and 5% in the

NWs as shown in Table 3.1 [6]. The NWs were characterized by TEM after implantation using Jeol 3010 and Jeol 3000F microscopes. The Mn-concentration was monitored by X-ray energy dispersive spectroscopy (XEDS) [2, 6].

Semiconductor materials	**NW diameters [nm]**	**Implantation parameters**				**Remarks (annealing time, geometry)**
		Temp. [°C]	**Energy [keV]**	**Fluence [ions/cm^2]**	***x* (%) (Mn concentration)**	
GaAs	40	250	40	1.00×10^{16}	5	No extra annealing, 45°
GaAs	80	300	100	1.80×10^{16}	5	No extra annealing, 45°
GaAs: Zn (10^{19}cm^{-3})	80	300	40	2.68×10^{11}	0.0001	12h @ 300 C and HV/ 45°/ rotating holder
GaAs: Zn (10^{19}cm^{-3})	80	300	40	2.64×10^{14}	0.1	12h @ 300 C and HV/ 45°/ rotating holder
GaAs: Zn (10^{19}cm^{-3})	80	300	40	1.32×10^{16}	5	12h @ 300 C and HV/ 45°/ rotating holder

Table 3.1: Parameters of the implanted NW samples investigated in this thesis. HV: high vacuum conditions pressure < 5×10^{-6} mbar.

3.2 Characterization by transmission electron microscopy

For high-resolution imaging, to assess the crystal structure and to verify the Mn content, the NWs were broken off and mechanically transferred to a holey carbon TEM grid. The XEDS provides information on chemical composition of the NWs with high spatial resolution. Also, details on the crystallinity can be extracted from Fourier transformations (FFT) of these HR-TEM images. Figure 3.2(a) shows an HR-TEM micrograph of a typical non-implanted, as-grown, NW for comparison. The single-crystalline zincblende NWs were grown in the <111> direction, showing twin planes perpendicular to the growth direction, as usually observed for III-V semiconductor NWs. Figures 3.2(b) and 3.2(c) show HR-TEM images of a nanowire implanted with 10^{16} ions/cm^2 at 250°C, corresponding to a total Mn-concentration of 2.9% (x = 5.8%). Even at these high concentrations, the NWs were observed to remain single-crystalline and no secondary phases were observed.

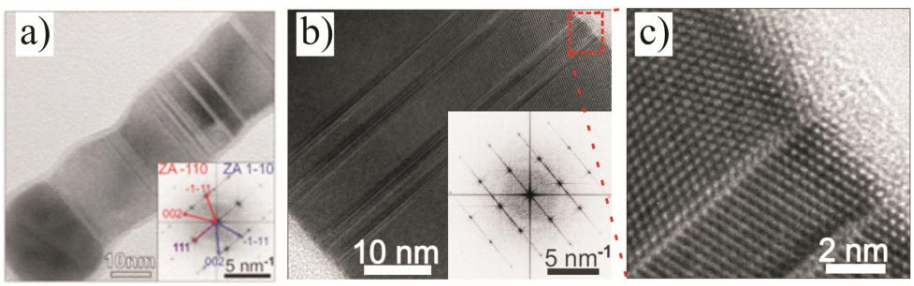

Figure 3.2: (a) TEM image of an as-grown (non-implanted) GaAs NW. The Au droplet is visible at the bottom left. Inset shows the corresponding FFT, reflexes are labeled; two directions occur due to twin planes. b) TEM image of a GaAs NW implanted with 10^{16} Mn ions/cm^2 at 250°C. The single-crystallinity with original twin-plane structure is maintained. Inset shows the FFT. (c) HR-TEM image of the same nanowire shown in b) [2, 36].

XEDS measurements were performed on several areas on these NWs (Figure 3.3). They confirmed a Mn-concentration of about 2% – 5%, showing that Mn has not out diffused during implantation at elevated temperatures.

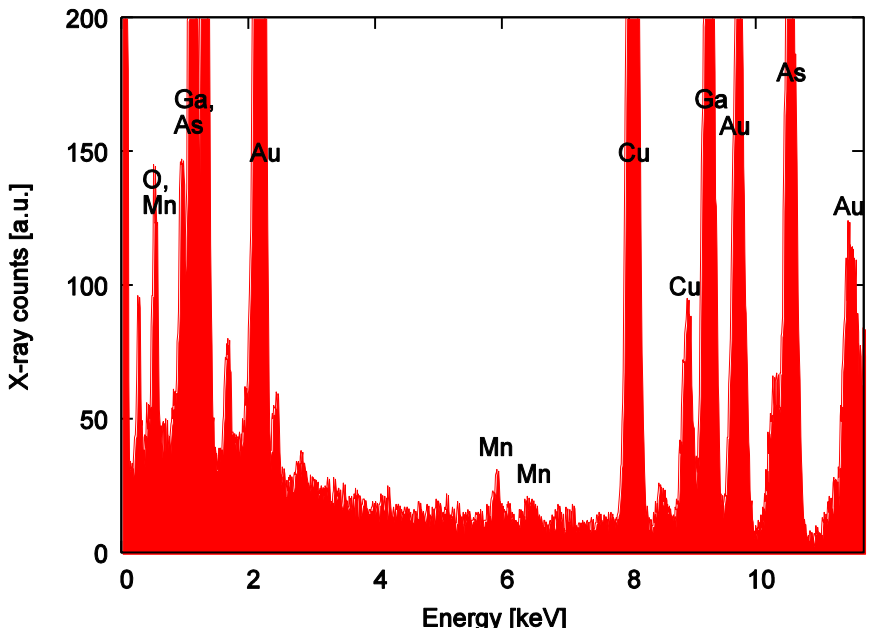

Figure 3.3: XEDS spectrum of a single GaAs NW implanted with 10^{16} Mn ions/cm^2 at 250 °C. The Mn-concentration can be estimated to 2.5 at.% [2, 36]. The Cu signal stems from the TEM grid.

Figure 3.4(a) shows a low resolution TEM image of a typical 80 nm diameter $Ga_{0.95}$ $Mn_{0.05}$As: Zn NW with less than 10 twin planes per µm. Figure 3.4(b) exhibits the corresponding diffraction pattern indicating an overall ZB crystal structure. The twin segments are responsible for the additional ZB diffraction spots. Between the few twin planes, the structure is pure ZB with no other polytype crystal structure as seen in the high resolution TEM image in Figure 3.4(c). XEDS was carried out by switching to scanning TEM mode with a

probe size of 0.6nm. Overlaid on Figure 3.4(a) is a linescan of Ga (Kα), As (Kα) and Mn (Kα) signals along the full length of the NW. The average Mn content along the scan line is 1.9 (standard deviation 0.2) at % (stoichiometric $Ga_{0,95}Mn_{0,05}As$).

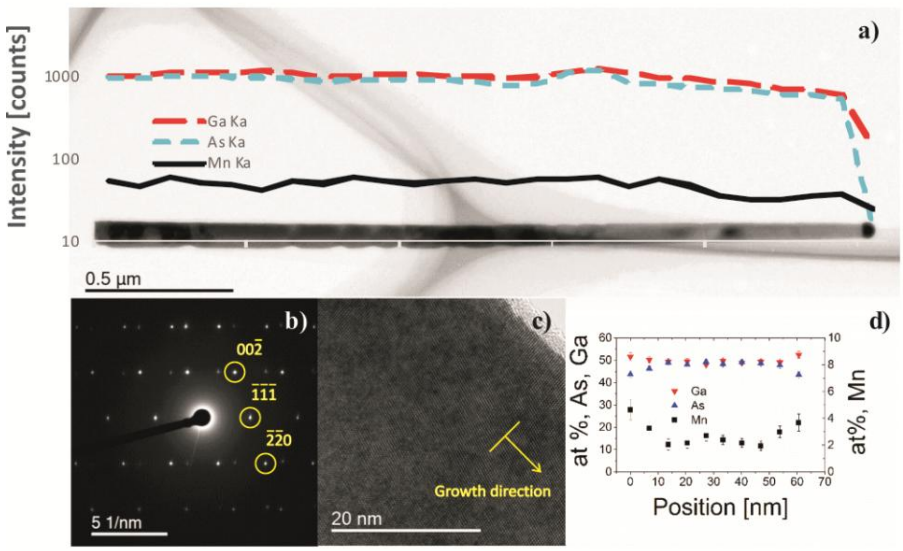

Figure 3.4: a) TEM image of Mn-implanted NW with a nominal Mn composition of 5 %. An XEDS line scan using the Ga (Kα), As (Kα) and Mn (Kα) peaks as reference is inserted. The diffraction pattern in b) indicates a single-crystalline ZB structure with few twin planes. c) HR-TEM image and d) radial XEDS line scans [6].

In addition to the linescan, a map along 300nm and full width of the NW was recorded. Interestingly, a radially non-uniform Mn content was found with slightly higher Mn content close to the NW surface, as seen in Figure 3.4(d). This non-uniformity, which was not expected from the *iradina* simulations, could stem from a weak segregation effect. Additionally, a small decrease in

As content is observed at the surface. Careful comparative analysis of the As distributions in as-grown GaAs NWs and annealed non-implanted NWs shows that the main reason for the As depletion in the implanted annealed NWs stems from selective sputtering of As versus Ga during implantation due to different surface binding energy. An additional smaller As surface depletion effect is caused by the outgassing of As during the vacuum annealing and TEM investigations [6].

Chapter 4

Nanofabrication techniques

The nanofabrication techniques described in this chapter are used for contacting of single-NW devices from GaAs, GaMnAs, GaAs: Zn and GaMnAs: Zn NWs, mechanically deposited on top of SiO_x/Si substrates [2 - 6].

In order to obtain single-NW devices suitable for magnetotransport measurements, the nanodevices need to be processed using rather advanced fabrication techniques, such as, wet cleaning processes and oxygen plasma ashing, dry- and wet-etching processes, lithography techniques (UV and electron beam), resist development processes [74], thermal metal evaporation processes and lift-off processes. The following sections describe the details of all these fabrication techniques.

4.1 Substrate preparation

For the electrical and magnetic measurements in this thesis, the as-grown NWs need to be transferred from the growth substrate to a suitable insulating measurement substrate where they are supplied with selective contacts. Moreover, to facilitate straight-forward alignment of the deposited and contacted single NWs with the external magnetic field, specially designed trenches are defined in the measurement substrate where the NWs are trapped. The measurement substrates are fabricated from highly n-type Si wafers. The NWs and electrical metal contacts must necessarily be insulated from the highly-doped wafer. Therefore, the top surface of the Si wafer is thermally

oxidized to grow a SiO_x-layer, about 200 nm in thickness [75]. Afterwards, the back-gate metal contacts are fabricated on the backside of the wafer by thermal metal evaporation. First, the top surface of the Si wafer is spin-coated with a layer of S-1813 photoresist spun for 60 s at 3000 RPM, and baked on a hotplate at 120 °C for 2 min. To remove possible residual resist from the backside of the Si wafer, it is cleaned with tissue paper wetted with acetone, and also etched by oxygen plasma ashing for 60 s. In order to etch away the natural oxide layer on the backside surface of the Si wafer, it is immersed in buffered hydrofluoric acid (BHF – 10:1) for 4 min; when the BHF forms droplets on the surface of the Si-wafer, then the oxide layer is completely etched away. Afterwards, the wafer must be rinsed carefully in water and dried in a N_2 flow. Then, by thermal evaporation, the 50 nm Ti layer, followed by the 100 nm Au layer are evaporated on the backside surface of the Si wafer. In order to remove the layer of the S-1813 photoresist on the top surface, the following resist cleaning recipe (RCR) is used: 10 min in hot mr Rem 400 resist remover (80 °C), 5 min in hot acetone (80 °C), and 2 min in an ultrasonic bath at high power, followed by rinsing in IPA and drying in a N_2 flow (Figure 4.1).

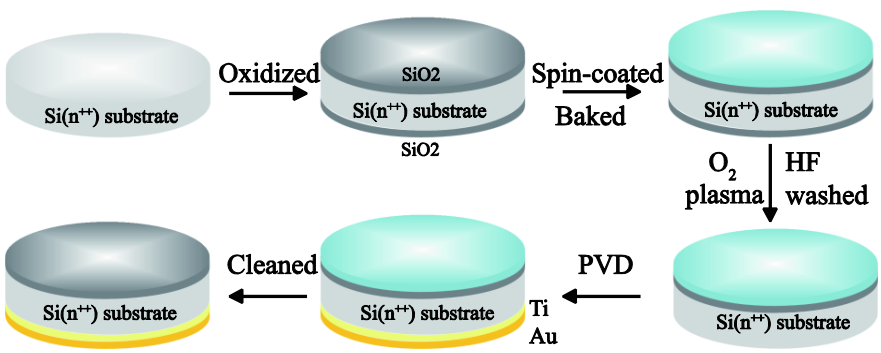

Figure 4.1: Schematics of measurement substrate fabrication: definition of top-oxide layer and back-gate metal, respectively. Figures are courtesy of Chunlin Yu.

The as-grown NWs are broken off the growth substrate and mechanically transferred to the measurement substrate in a wipe-off/wipe-on procedure using a cleanroom wipe. To locate the transferred NWs on top of the measurement substrate, an array of dots and alignment crosses are needed as a coordinate system. To fabricate these markers, the wafer is spin-coated with a thin layer of EB-resist ZEP520 A7 spun for 1 min at 6000 RPM, and baked on a hotplate at 180 °C for 15 min. The pattern of the alignment crosses and the array of dots are exposed in the EB-resist using EBL, and the EB-resist development is made in O-xylene for 5 min, followed by rinsing in IPA and drying in a N_2 flow. In order to remove any possible residual resist in the exposed patterns, the EB-resist is etched for 45 s in an oxygen plasma asher. Subsequently, by thermal metal evaporation, a 3 nm Ti layer is evaporated, followed by a 30 nm Au layer on the exposed patterns. The lift-off process is done in hot mr Rem 400 resist remover (10 min at 80 °C), 10 min in an ultrasonic bath at low power, followed by rinsing in IPA for 3 min and drying in a N_2 flow (Figure 4.2).

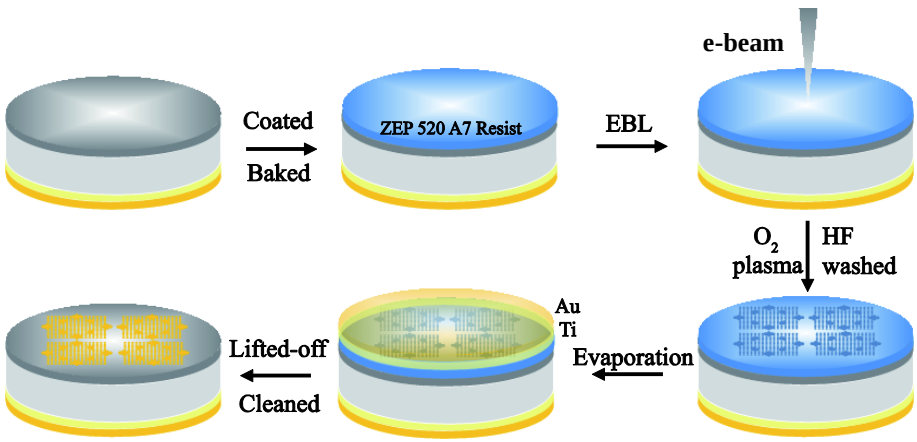

Figure 4.2: Schematics of fabrication of alignment crosses on the measurement substrate. Figures are courtesy of Chunlin Yu.

To realize the interface between the single nanowires and the measurement setup, it is necessary to fabricate macroscopic electrical contacts (bonding pads) on the measurement substrate. For this, the substrate is spin-coated with two layers of resist. The first layer is a thick layer of lift-off resist, LOR 7B, spun for 2 min at 5000 RPM and baked on a hotplate at 150 °C for 15 min. The second layer is a thin layer of photoresist, S-1813, spun for 2 min at 5000 RPM and also baked on a hotplate at 150 °C for 60 s. The bonding pad patterns are exposed using UV lithography, and the two layers of resist are developed in MF-319 for 5 min, followed by rinsing in H_2O and drying in a N_2 flow. In order to strip any possible residual resist in the exposed patterns, the two layers of resist are etched in an oxygen plasma asher for 45 s. Afterwards, a 5 nm Ti-layer followed by a 100 nm Au-layer are thermally evaporated on the exposed patterns. The lift-off process is again done in hot mr Rem 400 resist remover (10 min – 80 °C), 5 min in an ultrasonic bath at low power, followed by rinsing in H_20 and drying in a N_2 flow. Following this, the measurement substrate is finally cleaned by RCR (Figure 4.3), and cut into 3.5 x 5.0 mm pieces; each piece has 24 gaps for 12 nanowires supplied with 4-probe terminal contacts (Figure 4.4).

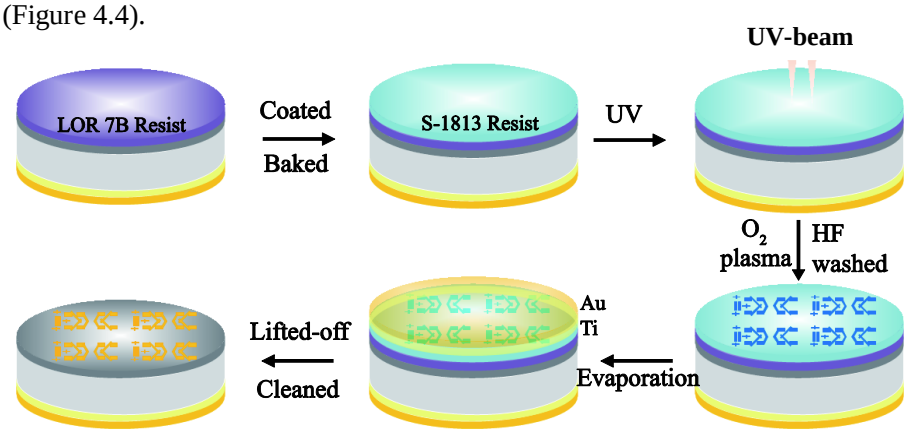

Figure 4.3: Schematics of fabrication of bonding pads and alignment crosses on the measurement substrate. Figures are courtesy of Chunlin Yu.

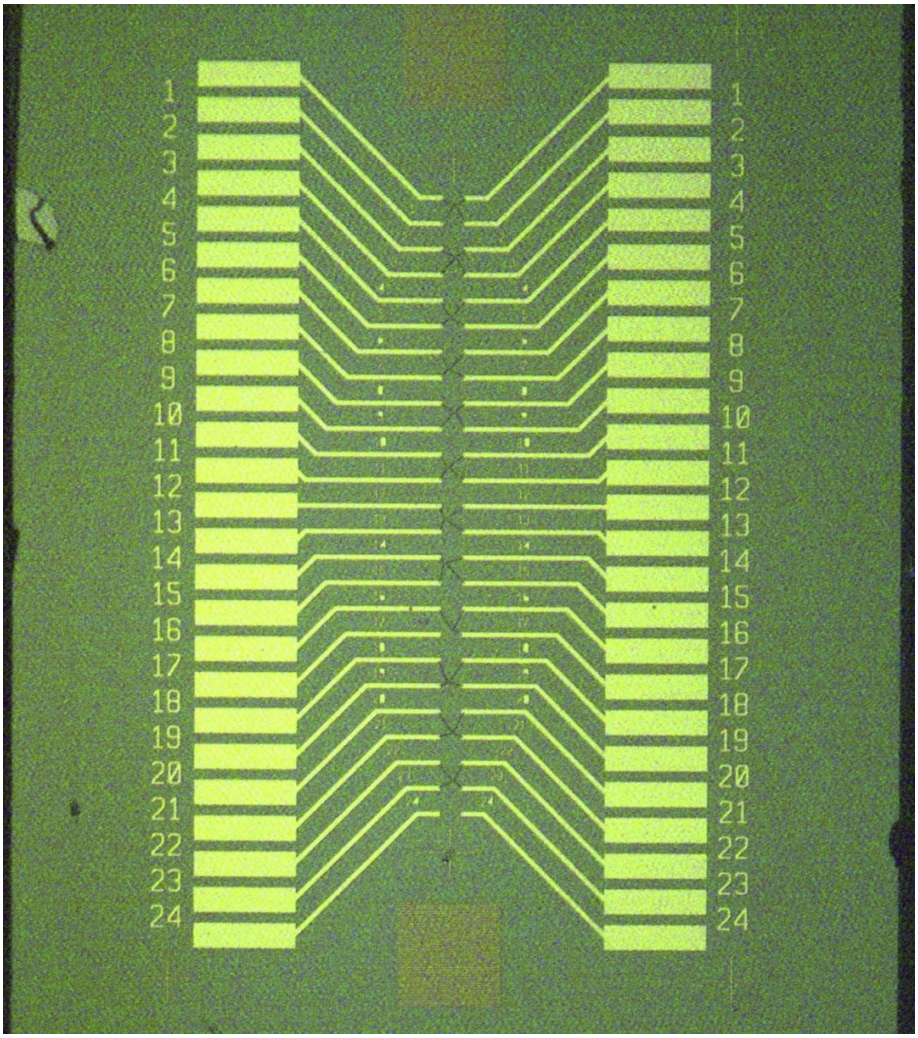

Figure 4.4: Optical microscopy image of a measurement substrate (3.5 x 5.0 mm) with 50 bonding pads and 24 gaps for 12 nanowire devices supplied with 4-probe terminal contacts.

4.2 Nanodevice fabrication

4.2.1 Etching of substrate alignment trenches

As already mentioned, the deposited NWs should be buried in etched trenches for simple alignment with the external magnetic field. Such a design also mitigates any NW dislocation during the lift-off process invoked in the fabrication of the 4-probe contacts. These trenches are patterned by EBL in an EB-resist spun on the top of the measurement substrates.

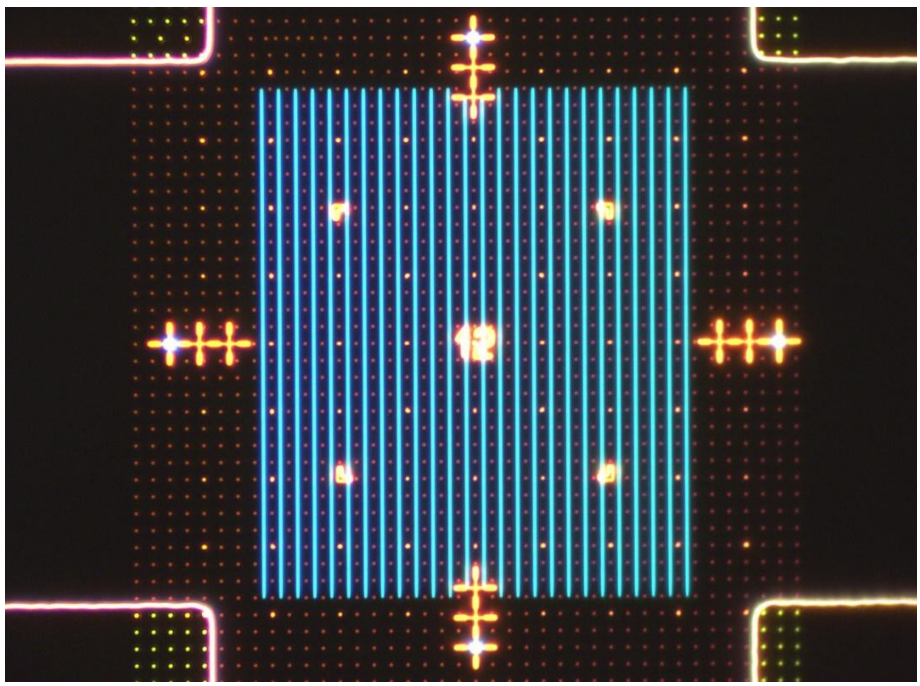

Figure 4.5: Optical microscopy bright field image showing the EBL pattern of the trenches after development and plasma preen.

To fabricate the trenches, the measurement substrate, shown in Figure 4.4, is first spin-coated with a thin layer of EB-resist PMMA 950 A4 spun for

30s at 6000 RPM, and baked on a hotplate at 180 °C for 10 min; the thin layer of EB-resist acts as a protective mask on the SiO_x-layer. After aligning the measurement substrate in the EBL using the alignment crosses, 12 patterns with 26 lines (50nm x 75µm) are exposed in the EB-resist PMMA 950 A4 by EBL. The PMMA 950 A4 development is done in MIBK:IPA (1:3) for 60 s, rinsed for 30 s in IPA, and dried in a N_2 flow. Subsequently, the substrate is treated for 45 s in the oxygen plasma asher to remove any possible residual EB-resists in the exposed patterns (Figure 4.5).

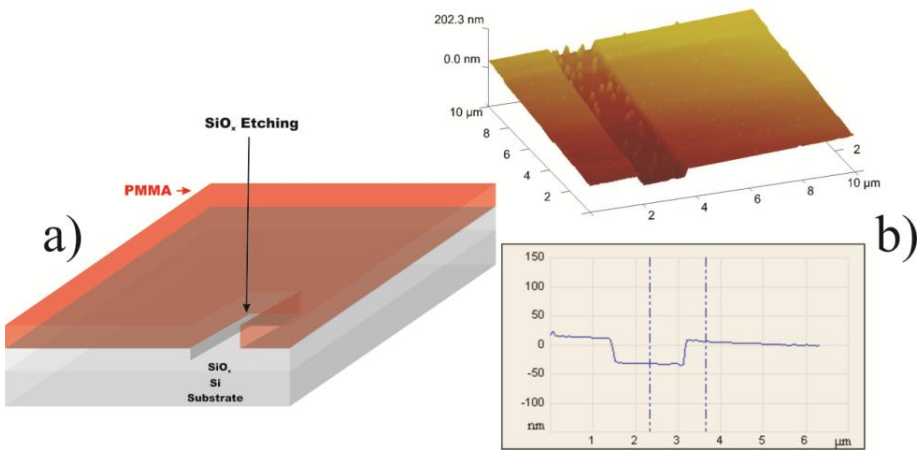

Figure 4.6: a) Schematics of trench etching using a thin layer of PMMA as protective mask. b) AFM image of an etched trench in SiO_x with a depth of approximately 38 nm.

Finally, the trenches are etched in the SiO_x-layer through anisotropic dry etching using ICP-RIE with CF_4, for 17s to a depth of approximately 38 nm (Figure 4.6). In the absence of oxygen in the plasma, released F atoms via reaction (1) below, react with Si atoms according to the etching reaction (2) producing volatile SiF_4:

$$CF_4 \rightarrow CF_3 + F \quad (1)$$
$$4F + Si \rightarrow SiF_4 \quad (2)$$

Afterwards, the PMMA 950 A4 is removed by RCR (Figure 4.7).

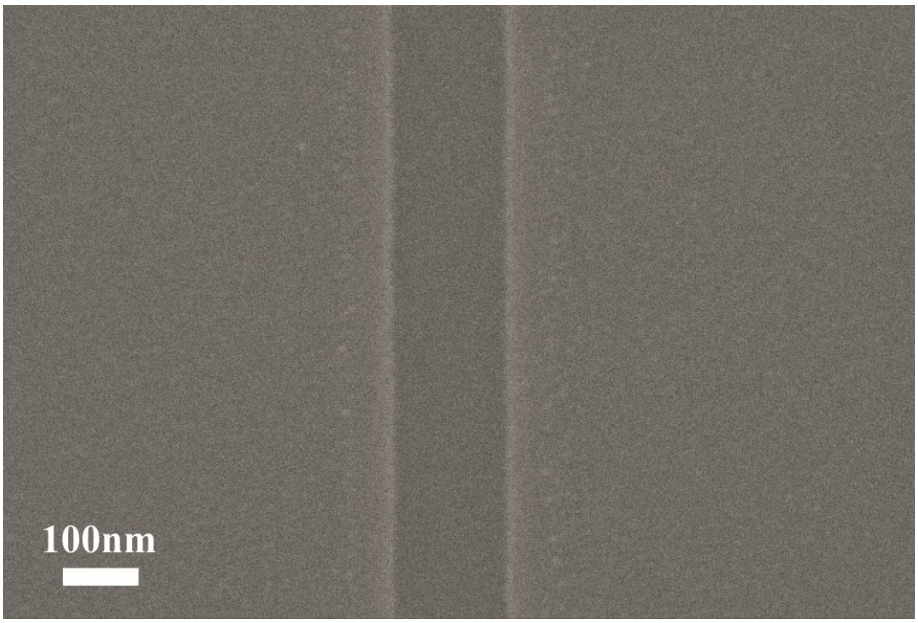

Figure 4.7: The SEM image shows a trench in SiO_x. The trench has a width of about 150 nm, while the nominal width is only 50nm.

4.2.2 Fabrication of selective 4-probe contact to nanowires

The NWs are mechanically transferred from the growth substrate to the trenches in the measurement substrate via gentle brushing with a small piece of cleanroom wipe. An optical microscope is used to locate the NWs properly trapped in the trenches, and also to record images of the whole sample (24 gaps on the measurement substrate with buried NWs) to perform the device design for each NW by a specific design program. Afterwards, the sample is cleaned in acetone under ultrasonic agitation at low power, followed by rinsing in IPA and drying in a N_2 flow, in order to remove all NWs not trapped in the trenches (Figure 4.8).

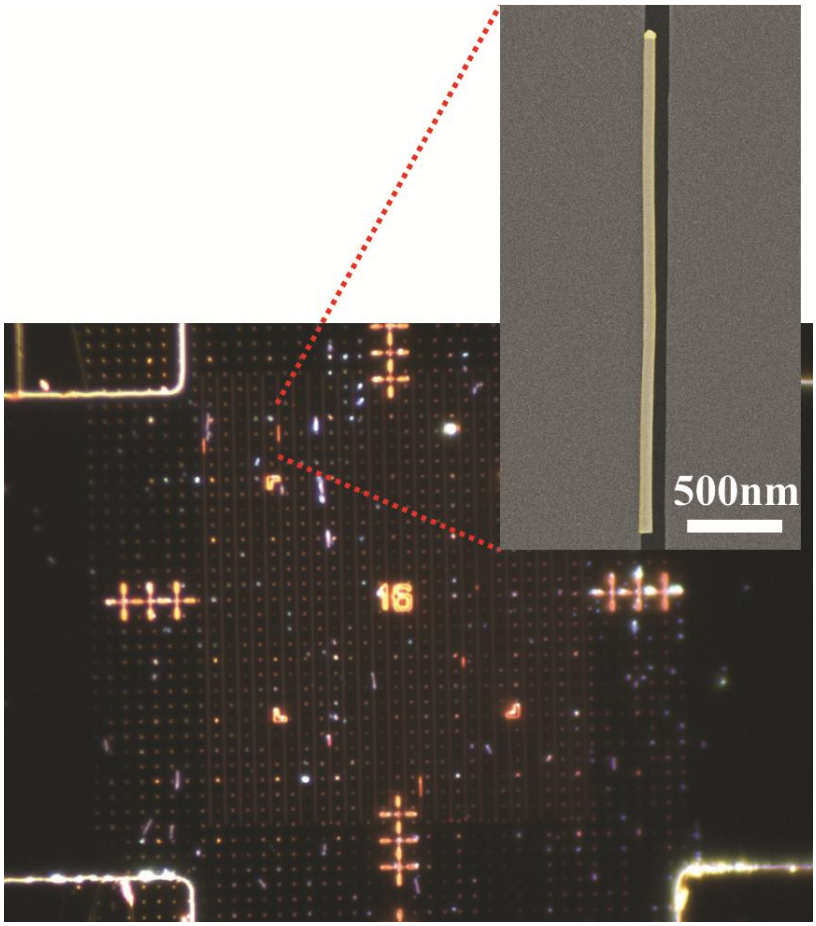

Figure 4.8: Optical microscopy bright field image showing NWs transferred to the measurement substrate. The inset SEM image shows a NW trapped in a trench etched in the SiO_x layer.

In order to fabricate selective metal contacts to the trapped NW**s**, the sample is spin-coated with a thin layer of EB-resist PMMA 950 A4 spun for 50s at 6000 RPM, and baked on a hotplate at 180 °C for 10 min. After aligning the sample in the EBL using the alignment crosses, individual contact patterns for each NW, designed by a specific program, are exposed in the PMMA 950 A4 by EBL, and subsequently developed in MIBK:IPA (1:3) for 60 s,

followed by rinsing in IPA for 30 s and drying in a N_2 flow. In order to remove any residual resist in the exposed patterns, the sample is etched in an oxygen plasma asher for 45 s.

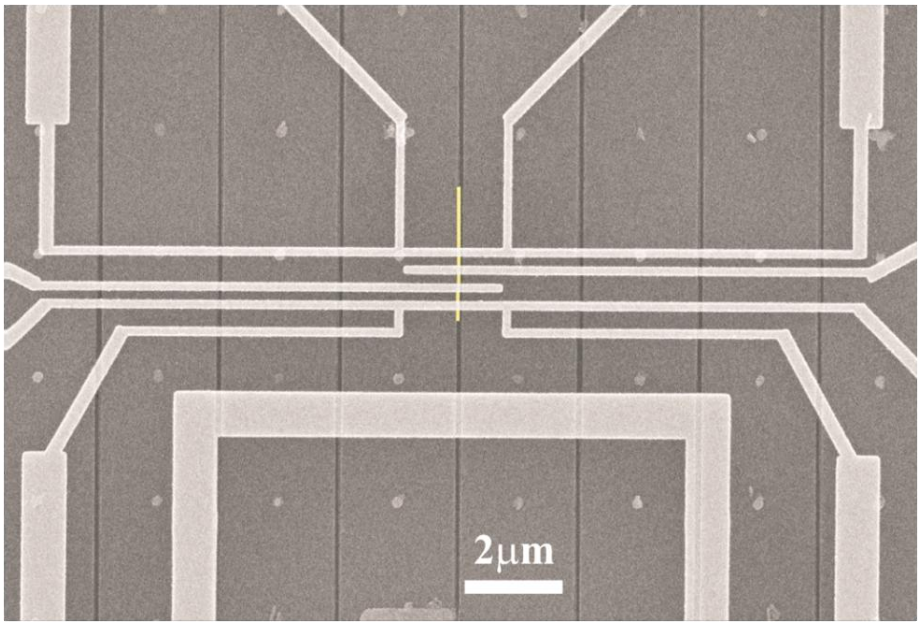

Figure 4.9: SEM image of a single GaMnAs NW trapped in a trench in the SiO_x layer. The more complicated sample layout used here is for thermoelectric measurements.

To make good metal-semiconductor contacts, a chemical treatment of the NW surface is necessary to remove the native oxide layer always present. The native oxide layer is removed by etching and passivation to avoid a re-oxidation. For the NWs used in this work, the oxide layer etching and the surface passivation are done by a wet etch-passivate process using $HCl:H_2O$ (1:1) for 20 s, followed by $(NH_4)_2S_x:H_2O$ (1:1) at 40 °C for 2 min. Immediately

after this process, the sample is placed in the thermal metal evaporator for metal deposition. To achieve good Ohmic contacts to the p-type GaAs NWs, a thin layer of Pd followed by, respectively, Zn and Pd, are deposited. [76]. Finally, the lift-off process is carried out in hot acetone for 10 min at 80 °C, followed by an ultrasonic bath at lower power for 30 s, rinsing in IPA, and drying in a N_2 flow. The finalized nanodevices are ready for magnetotransport or thermoelectric measurements (Figure 4.9). The samples must be placed promptly in the measurement setup or kept in a vacuum to avoid any stages of degradation.

Chapter 5

Electrical and magnetic measurement setup

This chapter provides a brief description of the electrical and magnetic measurement setup for the measurements conducted in this thesis.

The magnetotransport measurements were performed in a He_4 cryostat equipped with a superconducting magnet from Janis Research Co, model 8T-SVM. (Figure 5.1a) [77]. The cryomagnet system has a toroidal superconducting magnet with a vertical symmetry axis (along the dewar). The vertical magnetic field can be swept between –8T and 8T, and the temperature can be varied from 1.6K to 300K. In addition, the equipment used to carry out the magnetotransport measurements includes a Stanford lock-in amplifier (model SR830), a Hewlett-Packard multimeter (model 34401A), a Stanford low-noise current pre-amplifier (model SR570) and a FEMTO low-frequency and high-input impedance voltage amplifier (model DLPVA -100-B-S).

To investigate the possible influence of contact resistance between the contacts and NW, 4-probe terminal measurements were carried out as shown in the SEM micrograph in Figure 5.1b, with the magnetic field applied both parallel and perpendicular to the NW.

Also, the magnetic properties of the NWs were measured using a SQUID-VSM magnetometer manufactured by Quantum Design Corporation. The combination of the SQUID and VSM technology provides superior sensitivity (standard deviation 10^{-8} emu) and fast measurement cycles. The magnetic field is applied perpendicular to the measurement substrate

comprising large ensembles of randomly deposited NWs. The SQUID experiments were carried out in collaboration with the team of Prof. Dr. Maw-Kuen Wu from Taipei in Taiwan [5].

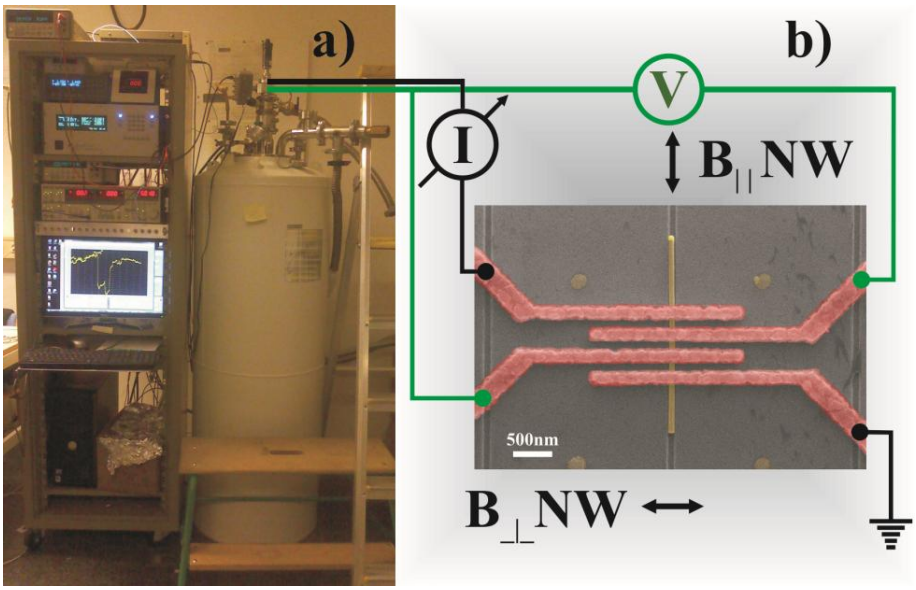

Figure 5.1: a) Janis VariTemp superconducting cryomagnet system (model 8T-SVM) and b) SEM micrograph of a single NW supplied with 4-probe terminal contacts for magnetotransport measurements.

Figure 5.2 shows the device layout used for thermoelectric measurements. In order to provide a temperature gradient for the thermopower measurements, a heater is integrated with the NW sample. The NW and heater are electrically isolated from each other to avoid any electrical influence; however there is a thermal contact through the substrate. The substrate leads the thermal energy from the heater, generating a temperature gradient along the surface and nanowire. In addition, 4-probe thermometers are necessary to

measure the temperatures accurately at both ends of the nanowire. The transport measurements were done with a standard 4-probe design, to investigate possible influence of contact resistance at low temperatures.

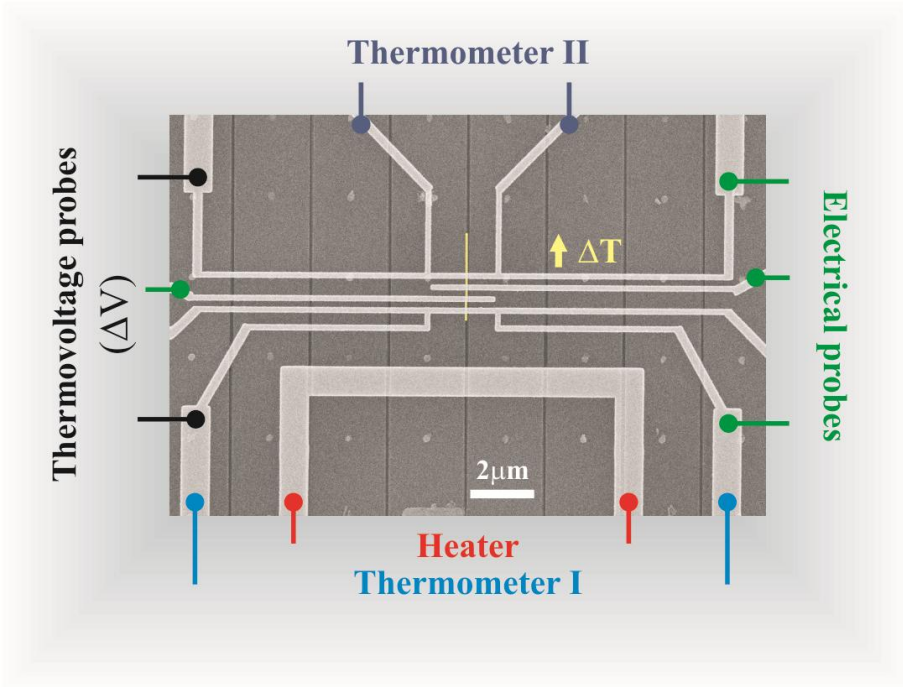

Figure 5.2: SEM image of a single GaMnAs NW trapped in a trench in the SiO_x layer. The more complicated sample layout used here is for thermoelectric measurements. The yellow arrow indicates the temperature gradient.

Chapter 6

Carrier transport mechanisms in Mn ion-implanted GaAs nanowires

The temperature-dependent carrier transport mechanisms in Mn ion-implanted GaAs NWs are governed by hopping conduction. Hopping conduction in semiconductors is typically associated with a significant degree of disorder, which in the case of NWs is created during the implantation. The Mn ions impact the nanowires with an energy in the range of several tens of keV, which creates many different types of defects such as antisites, vacancies and interstitials. In this chapter, nearest-neighbor hopping conduction and variable-range hopping conduction in low and high electric field regimes are discussed at length. Based on meticulous 4-probe resistance measurements, combined with analysis, important parameters such as characteristic hopping energies and corresponding hopping lengths have been extracted. At low temperatures, a strongly non-linear conductivity is observed, which reflects a modified hopping conduction driven by the high electric field at large bias. Also, hopping conduction has been studied in the context of temperature-dependent thermopower measurements. It is shown that the thermopower coefficient is strongly enhanced at low temperatures. A modified model for the thermopower which includes a hopping term provides good agreement between theory and experiments.

6.1 Temperature-dependent and electric field-dependent carrier transport in disordered semiconductors

Experimental facts show that temperature-dependent carrier transport in disordered semiconductors is driven by hopping conduction [3]. Hopping conduction was proposed by Mott [78] and similar and complementary ideas were also independently developed by Abrahams, Anderson, Convell, Efros, Miller, Pines and Shklovskii [79]. Doped semiconductors have an electrical conductivity governed by thermal emission of carriers from the impurity states to the conduction band or to the valence band. Above the intrinsic temperature, band-to-band transitions determine the carrier concentration in the bands, and thus the conductivity. At low temperatures and sufficiently high concentrations of impurities, the electrical conductivity is determined by carriers hopping directly between impurities rather than by drift motion of free charge carriers thermally excited to the bands. Hopping conduction is characterized by a low mobility, since the carrier hops are related to a small overlap of wave function tails from neighboring impurities.

Figure 6.1 shows schematically the temperature-dependence of the resistance of a doped/disordered semiconductor, divided into four ranges (A, B, C and D). The range A indicates intrinsic conduction governed by band-to-band transitions. The range C corresponds to the freeze-out range, where a decrease in temperature leads to a progressive freeze-out of the free carriers in the bands which are recaptured by impurities. The ranges B and D represent extrinsic conductance. If the impurities are shallow, there is a range B, called the saturation range, in which all the impurities are ionized, and therefore the carrier concentration is temperature-independent except for a weak dependence of the mobility (scattering rate) on the temperature. For example, the decrease

in resistance with decreasing temperature in Figure 6.1 is related to a reduced phonon scattering [80].

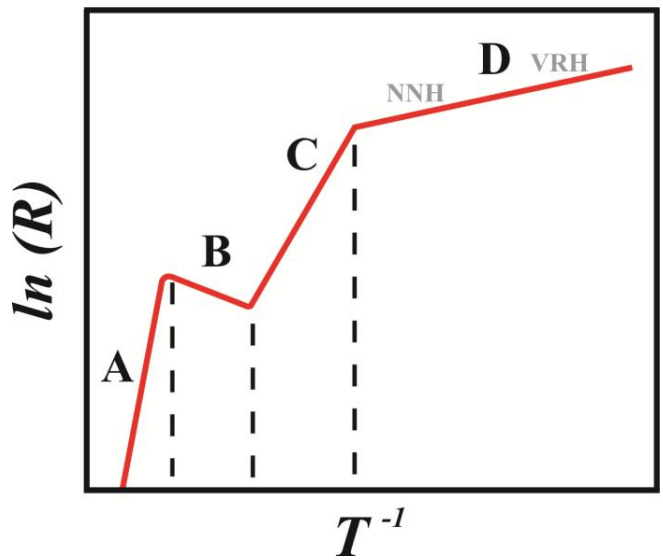

Figure 6.1: Schematic temperature-dependence of the resistance of a doped/disordered semiconductor, divided into four ranges: A – intrinsic conduction range, B – saturation range of impurity conduction, C – freeze-out range and D – hopping conduction range.

In disordered systems, there is often a temperature range where the electrical conductivity is governed by carriers hopping directly between impurities without being excited to the conduction band or the valence band (range D in Figure 6.1). Carriers hop from filled localized states to empty ones, and thus the existence of empty localized states is an essential condition. Two different conduction hopping mechanisms through localized states in a disordered semiconductor are schematically shown in Figure 6.2: (a) Nearest-neighbor hopping (NNH) conduction and (b) Variable-range hopping (VRH) conduction.

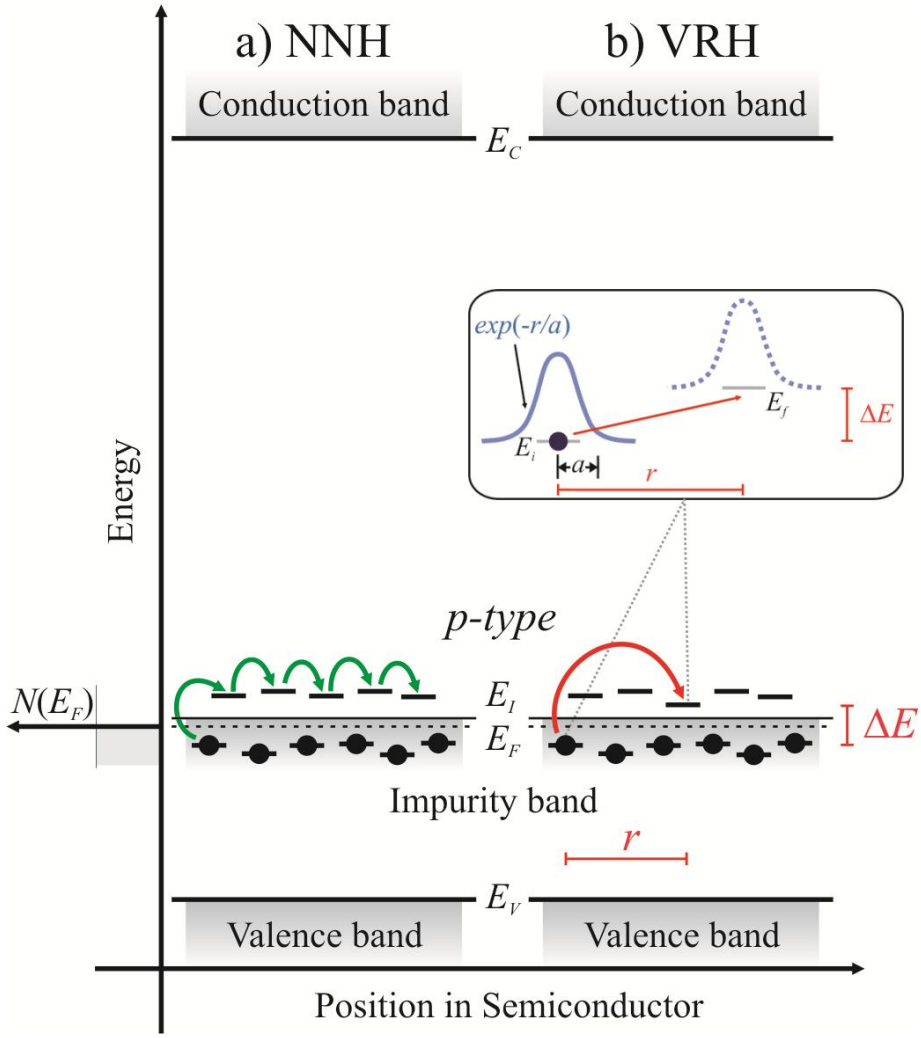

Figure 6.2: Schematics show two different conduction hopping mechanisms for carrier transport through localized states in disordered semiconductors: (a) NNH conduction and (b) VRH conduction.

The hopping conduction (NNH and VRH) shown in range D in Figure 6.1 sets in at low temperatures where the thermal energy is insufficient to excite the carriers from the impurity bands to the conduction band or to the

valence band, but large enough to overcome the barriers associated with hopping between localized states connected to the impurity band.

Figure 6.2 (a) shows NNH conduction in which the carrier transport is principally carried out by hops between nearest neighbor localized energy states. In NNH conduction, the thermal activation energy (ΔE) of the hop is constant up to a specific temperature.

In some disordered semiconductors, where the disorder is not too strong, there is another important process indicated in Figure 6.2 (b). This process, introduced by Mott, is known as VRH conduction. Here, the hops do not take place between nearest-neighbor localized energy states, instead the carriers can opt for an energy state further away in space, but closer in energy. Figure 6.2 (b) shows VRH conduction, typically occurring at lower temperatures than NNH (see range D in Figure 6.1). VRH is characterized by a temperature-dependent $\Delta E(T)$ and an increased average carrier hopping distance $r(T)$ [80 - 82].

The NNH mechanism shown in Figure 6.2 (a) involves thermal excitation of a carrier from one localized state to the nearest localized state in space, above the Fermi level. This mechanism can be used to explain the carrier transport in disordered semiconductors [79] at low temperatures. To estimate the resistance, the carrier wave function is chosen as [81]

$$\psi = \exp\left(-\frac{r}{a}\right), \tag{6.1}$$

where a is the localization length of the carrier wave function in the impurity band and r is the hopping distance, which can be much longer than the localization length at low temperatures. Hopping conduction is governed by the hopping probability between impurity sites. A hopping carrier will always try

to find the lowest activation energy ΔE, given by the energy separation between adjacent localized impurity states, and the corresponding shortest hopping distance. There is an optimum hopping distance r, which maximizes the hopping probability. At thermal equilibrium (at sufficiently low bias), the hopping probability is given by

$$P \propto \exp\left(-\frac{2r}{a}-\frac{\Delta E}{k_B T}\right), \tag{6.2}$$

where k_B is the Boltzmann constant and T is the temperature. Thus, the temperature-dependence of the resistance (R) can be described by [80]

$$R = R_0 \exp\left(-\frac{2r}{a}-\frac{\Delta E}{k_B T}\right), \tag{6.3}$$

where R_0 is a resistance constant. When hopping conduction is governed by Eq. 6.3 with a constant activation energy ΔE, the average hopping distance is of the order of the mean separation between impurities, and it does not vary with temperature.

The current is proportional to the overlap between the wave functions, the density of states at the Fermi level $N(E_F)$, the width of the Fermi distribution $k_B T$, the effective transport velocity denoted as v_T, and the average spacing r between the states. If ΔE is the average energy separation between two states and V the applied bias, then the current is given by [81]

$$I = 2ek_B TN(E_F) r \mathrm{S} v_T \exp\left(-\frac{2r}{a}-\frac{\Delta E}{k_B T}\right)\sinh\left(\frac{eVr}{\mathrm{L}k_B T}\right), \tag{6.4}$$

where e is the electron charge, S is the cross-sectional area of the semiconductor device and L is the distance between two contacts to which a bias is applied (for example, the distance between the contacts to a NW). For a small bias, the sinh function can be expanded and the conductivity becomes

$$\sigma = 2e^2 r^2 \nu_T N(E_F) \exp\left(-\frac{2r}{a} - \frac{\Delta E}{k_B T}\right). \tag{6.5}$$

In 1969, Mott derived a theoretical description of another type of hopping conduction in disordered systems with localized states based on the hopping rate calculated by Miller and Abrahams [82]. Mott introduced the concept of variable-range hopping (VRH), where considerably longer hops govern the conductivity at low temperatures. The VRH conduction can be described as a carrier's preference for a more spatially distant state with a smaller activation energy than a nearby state with a larger activation energy. At decreased temperature, the thermal energy decreases and thereby also the accessible activation energy $\Delta E(T)$. Thus, only the carriers with energy states near to the Fermi level E_F are allowed to hop. Empty energy states with $\Delta E(T)$ are rare and separated by larger spatial distances; see Figure 6.2 (b). The lower the temperature is, the fewer available energy states there are, and the larger is their spatial separation. Thus, the hopping distance increases with decreasing temperature.

The hopping distance r, which can be much longer than the localization length (a) at low temperatures [80], depends on the temperature according to

$$r(T) = \left(\frac{9a}{8\pi N(E_F) k_B T}\right)^{1/4}, \tag{6.6}$$

for a 3D system. Here $N(E_F)$ is the density of states near the Fermi level. The corresponding activation energy is given by

$$\Delta E(r) = \frac{3}{4\pi r(T)^3 N(E_F)}. \tag{6.7}$$

According to the theory of VRH proposed by Mott [82, 83], if the effect of electron-electron interactions is negligible, and a constant $N(E_F)$ is

assumed, the temperature-dependence of the resistance in the linear (Ohmic) region can be expressed as

$$R = R_0 \exp\left(\frac{T_0}{T}\right)^p, \tag{6.8}$$

where $p = \frac{1}{4}, \frac{1}{3}$ or $\frac{1}{2}$ for 3D, 2D, and 1D systems, respectively. Here R_0 and T_0 denote material parameters. The exponent p in Eq. 6.8 is determined by the slope of the double logarithmic plot of $W = \frac{d[\log(G)]}{d[\log(T)]}$ versus T, where $G = \frac{1}{R}$ is the conductance of the material [3, 84]. T_0 is related to the carrier localization length a and density of states near the Fermi level $N(E_F)$ according to

$$T_0 = \frac{18}{k_B a^3 N(E_F)}. \tag{6.9}$$

The conduction mechanism of VRH is modified at large biases. Under high electric field (F) conditions, a carrier can hop from a filled state to an empty state along the field direction with the activation energy reduced by an amount, $e.F.r$ [85, 86]. When the electric field reaches a critical value F_C, such that the energy $e.F_C.r$ gained during a hop becomes comparable to the activation energy for hopping, carriers can move along the electric field. The resistance which becomes temperature-independent can then be expressed in the form

$$R = R_{0F} \exp\left(\frac{F_0}{F}\right)^p, \tag{6.10}$$

where R_{0F} and F_0 are material constants. F_0 is proportional to T_0 as

$$F_0 = \frac{k_B T_0}{2ea}, \tag{6.11}$$

where a is the localization length as stated before.

6.2 Hopping conduction in GaMnAs nanowires

This section provides insight into the carrier transport properties of doped Mn ion-implanted GaAs NWs. From meticulous measurements of the temperature-dependent resistance, in combination with detailed analysis, it is shown that the transport is governed by different hopping mechanisms within an impurity band of localized Mn states. With decreasing temperature, there is a clear transition from NNH to VRH conduction. It is also shown that electric field-driven VRH dominates at sufficiently low temperatures and high electric field strengths.

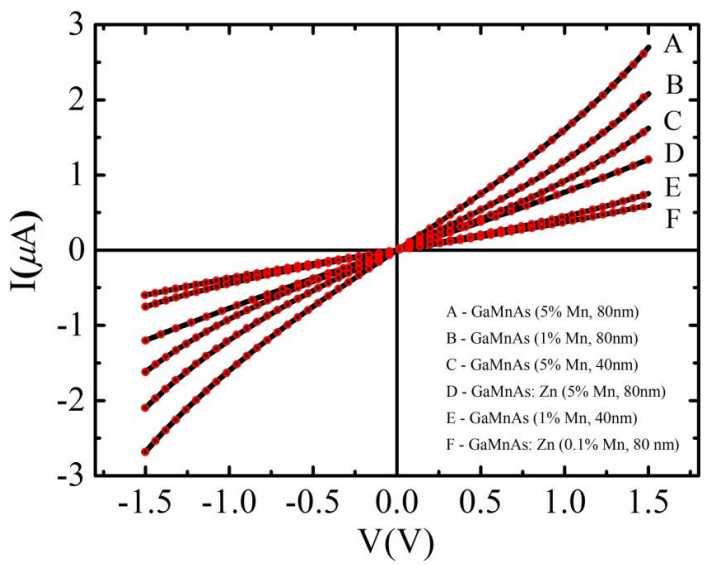

Figure 6.3: $I-V$ characteristics of single $Ga_{1-x}Mn_xAs$ (x = 1% and 5%) and $Ga_{1-x}Mn_xAs$: Zn (x = 0.1% and 5%) NW devices of 40 nm and 80 nm diameter. Black solid curves represent the experimental data, while the red circles are fitted by Eq. 6.4.

Figure 6.3 shows current voltage ($I - V$) characteristics of single $Ga_{1-x}Mn_xAs$ (x = 1% and 5%) and $Ga_{1-x}Mn_xAs$: Zn (x = 0.1% and 5%) NW devices of 40 nm and 80 nm diameter. At 300K (RT), the slightly non-linear and anti-symmetric $I - V$ curves suggest that the transport could be governed by incoherent carrier hopping between spatially adjacent energy states in the impurity band formed by the Mn ion-implantation. The expected $I - V$ relation for such a hopping process is governed by Eq. 6.4 [81].

For a single $Ga_{1-x}Mn_xAs$ (x = 5%) NW device of 80 nm diameter, all $I - V$ curves for T > 50K could be fitted by Eq. 6.4. At lower temperatures, the $I - V$ curves become increasingly nonlinear, however, with maintained anti-symmetry with respect to the bias (Figure 6.4).

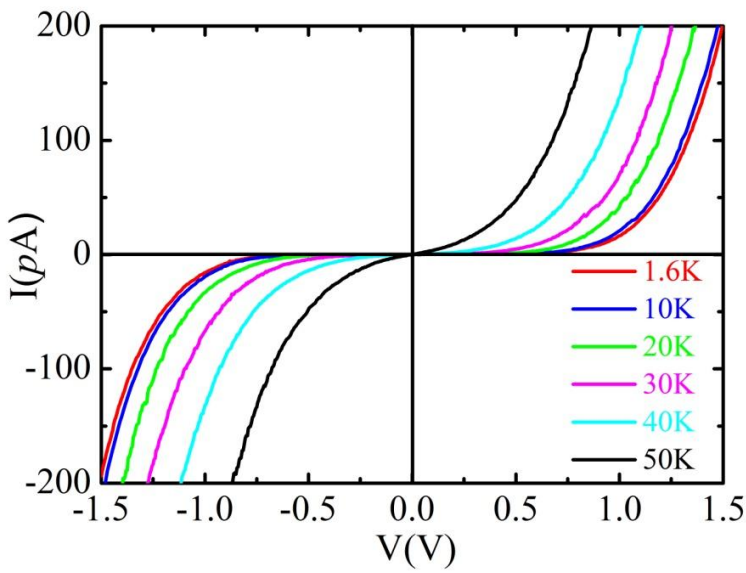

Figure 6.4: The strongly nonlinear $I-V$ characteristics at lower temperatures for a single $Ga_{1-x}Mn_xAs$ (x = 5%) NW device of 80 nm diameter.

At elevated temperatures, the hopping length r eventually becomes equal to the nearest-neighbor distance d . The hopping probability then becomes

$$P \propto \exp\left(-\frac{\Delta E_A}{k_B T}\right), \tag{6.12}$$

which resembles an Arrhenius relation describing a nearest-neighbor hopping mechanism with an activation energy ΔE_A. Different transport mechanisms have been proposed in the literature for disordered semiconductors [81]. For a *p*-type semiconductor at low temperatures, most of the free holes are recaptured by the acceptors. As a result, hole conduction in the valence band becomes less important, and hole hopping directly between acceptors in the impurity band provides the main contribution to the conductivity, as NNH and VRH mechanisms.

In order to further unravel the electronic transport mechanism of a single $Ga_{1-x}Mn_xAs$ (x = 5%) NW device of 80 nm diameter, the temperature-dependence of the resistance from 1.6K to 300K is studied. As shown in Figure 6.5, a change of slope of $log(d(log(G))/d(log(T)))$ versus $log(T)$, where G is the conductance, is observed around 180K. The value of p amounts to about 0.25 in the temperature region 50K < T < 180K and to 0.9 above 180K, respectively. A value $p = 1/4$ corresponds to the 3D VRH mechanism, whereas $p = 0.9$ is consistent with a NNH mechanism. The extracted *p*-factor of 0.9 for T > 180K is close to 1, also valid for a thermally stimulated transport mechanism involving valence band conduction whereby a contribution from this type of conduction cannot be excluded. The NWs used here have a diameter of ~ 80 nm, which is much larger than the hopping length, so the hole transport is expected to exhibit a predominantly three-dimensional character [3].

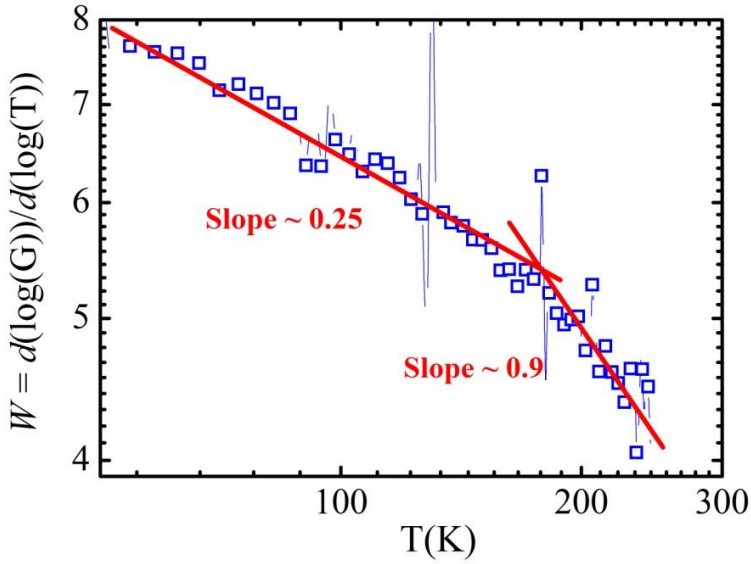

Figure 6.5: Double log plot of $\frac{d[\log(G)]}{d[\log(T)]}$ versus T for a single $Ga_{1-x}Mn_xAs$ (x = 5%) NW device of 80 nm diameter at a bias of 100 mV. The red solid fitting lines are used to extract the *p*-factors.

Figure 6.6 shows ln(R) versus T^{-1} in the temperature range 50K to 300K at a constant bias of 100mV (within the linear region of the $I - V$ curve as seen in Figure 6.4). Fitting of the resistance data to Eq. 6.12 in the temperature interval 180K < T < 300K is also shown in Figure 6.6. Above 180K, the NNH mechanism dominates with an activation energy of ΔE_A = 90 meV [3]. As already mentioned, a contribution to the conductivity from holes excited to the valence band cannot be excluded.

From the data presented in Figure 6.6, the fit to ln(R) versus $T^{-1/4}$ curve, between 50K and 180K, can be estimated the parameter T_0, a value of T_0 = 5.2×10^{7}K, which corresponds to a $N(E_F)$ = 4.0×10^{18} (eV.cm^3)$^{-1}$ by Eq.

6.9. The value of a is assumed to be of the same order as the acceptor Bohr radius for GaMnAs ($\sim$ 1nm), and then, the hopping length r and corresponding hopping energies ΔE can be extracted. Figure 6.7 shows r and ΔE versus T. At 50 K, an average hopping energy ΔE of 34 meV and a hopping length of r = 12.0 nm are estimated. At 180 K, ΔE increases to 90 meV, while the hopping length decreases to 8.7 nm. Within a single-particle hopping scenario, the hopping length r should eventually become of the order of the average impurity distance [3].

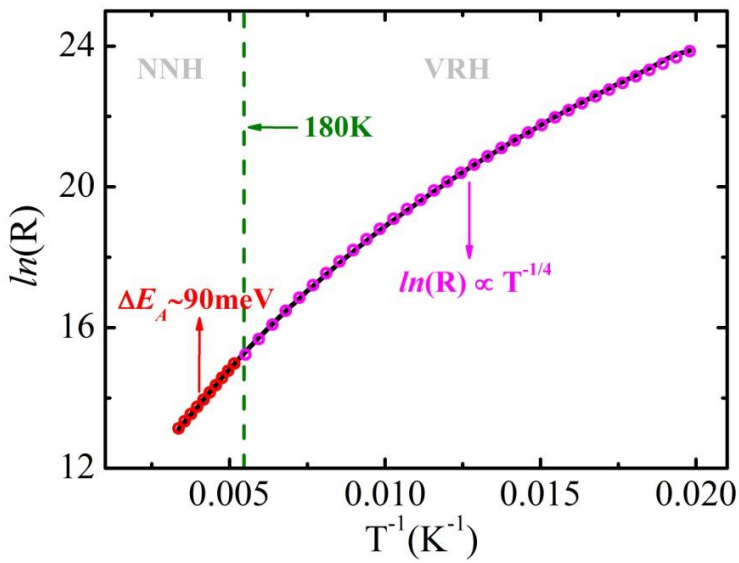

Figure 6.6: $ln(R)$ plotted versus T^{-1} for a single $Ga_{1-x}Mn_xAs$ (x = 5%) NW device of 80 nm diameter at a constant bias of 100 mV. The resistance data (black solid curve) is fitted to the VRH model with $p = 1/4$ (Eq. 6.8) in the temperature range 50K < T < 180K (magenta circles) and to the Arrhenius relation (Eq. 6.12) in the temperature interval 180K < T < 300K (red circles).

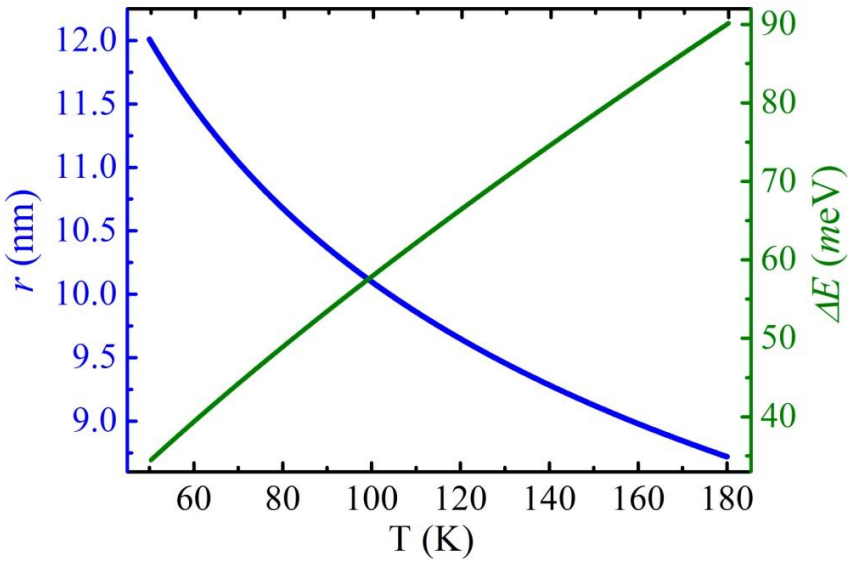

Figure 6.7: Hopping length r versus T (blue solid line) and ΔE versus T (green solid line) for a single $Ga_{1-x}Mn_xAs$ (x = 5%) NW device of 80 nm diameter.

At sufficiently low temperatures and large bias, a strongly non-linear conductivity is observed (Figure 6.4) which reflects a hopping mechanism modified by the high electric field strength. Following Eq. 6.10 is plotted $\ln(R)$ versus $F^{-1/4}$ in Figure 6.8. Here it is readily observed that the high-field data recorded at different temperatures merge on a single line at a temperature-dependent F_C. From the slope of the fitted line, the factor F_0 = 2.0×10^{12} Vm^{-1} is extracted. Inserting the values of F_0 and T_0 into Eq. 6.11 gives the localization length a = 1.1 nm, which is in very good agreement with the

expected Mn acceptor Bohr radius [3]. Also, from Eq. 6.6 is estimated r = 28.1 nm and a corresponding ΔE = 2.66 meV at 1.6 K by Eq. 6.7.

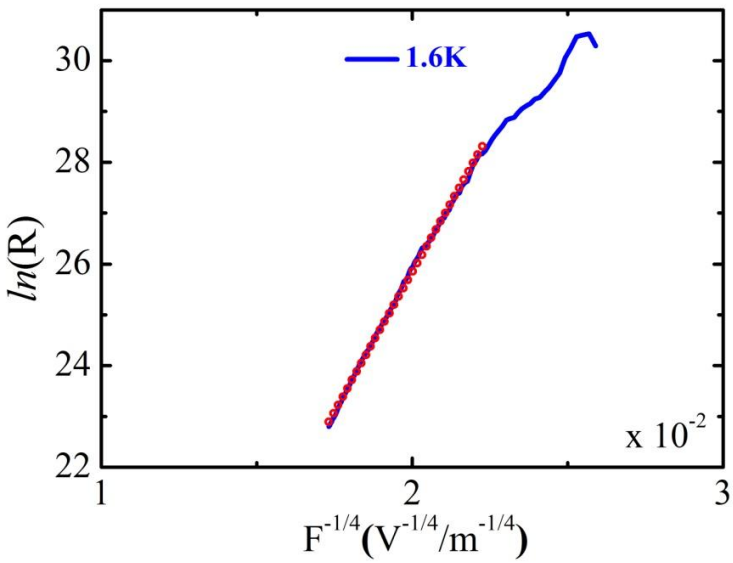

Figure 6.8: Plot of $ln(R)$ versus $F^{-1/4}$ at 1.6 K for a single $Ga_{1-x}Mn_xAs$ (x = 5%) NW device of 80 nm diameter. The red solid line is a least square fit to the high-field data.

The analysis of the resistance at high field strengths has also been carried out for GaMnAs NWs co-doped with Zn (GaMnAs: Zn) at low temperatures. Figure 6.9 shows the plotted ln(R) versus $F^{-1/4}$ at 1.6K, for a single $Ga_{1-x}Mn_xAs$: Zn (x = 5%) NW device of 80 nm diameter. Following the same analysis as above is extracted the factor F_0 = 2.2×10^{12} Vm^{-1} from the slope of the fitting curve. Substituting into the Eq. 6.11 the values of F_0 and a = 1nm is calculated T_0 = 5.17×10^{7}K, and the $N(E_F)$ = 4.04×10^{18} $(eV.cm^3)^{-1}$ by Eq.

6.9. From Eq. 6.6 is extracted a hopping length r = 28.1 nm and a corresponding hopping energy ΔE = 2.65 meV at 1.6 K by Eq. 6.7.

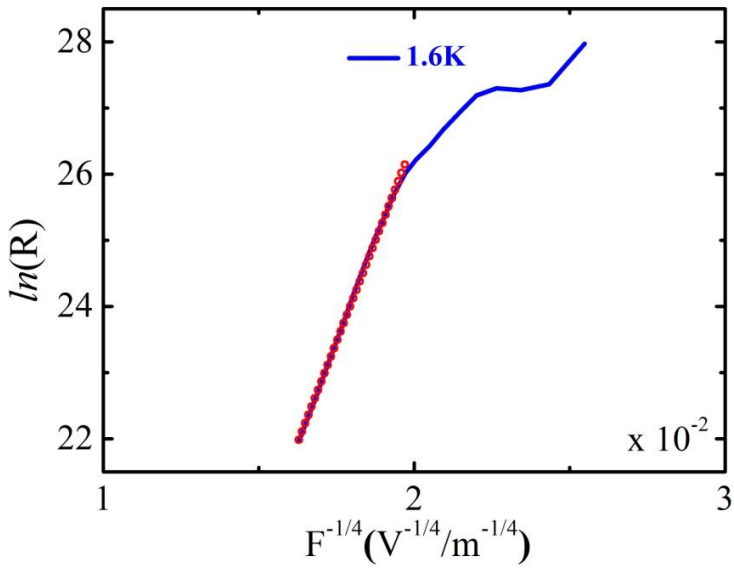

Figure 6.9: Plot of $ln(R)$ versus $F^{-1/4}$ at 1.6 K for a single $Ga_{1-x}Mn_xAs$: Zn (x = 5%) NW device of 80 nm diameter. The red solid line is a least square fit to the high-field data.

Similarly, in Figure 6.10 is plotted ln(R) versus $F^{-1/4}$ for a single $Ga_{1-x}Mn_xAs$: Zn (x = 0.1%) NW device of 80 nm diameter. From the fitting at high electric fields is extracted a parameter $F_0 = 1.64\times10^{12}Vm^{-1}$. Replacing the values of F_0 and a = 1nm in Eq. 6.11 is estimated $T_0 = 3.80\times10^{7}K$, and by Eq. 6.9 is calculated the $N(E_F) = 5.48\times10^{18}$ $(eV.cm^3)^{-1}$, which yields a hopping length r = 26 nm (Eq. 6.6) and a corresponding hopping energy ΔE = 2.46 meV at 1.6 K (Eq. 6.7).

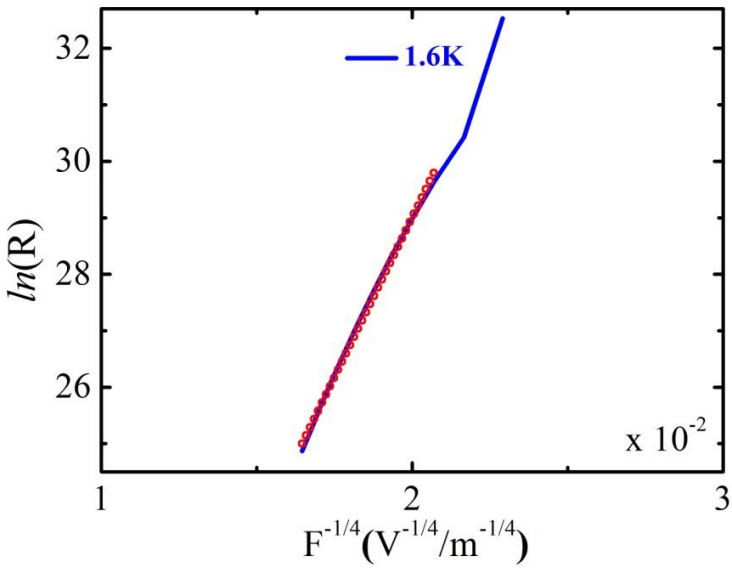

Figure 6.10: Plot of $ln(R)$ versus $F^{-1/4}$ at 1.6 K for a single $Ga_{1-x}Mn_xAs$: Zn (x = 0.1%) NW device of 80 nm diameter. The red solid line is a least square fit to the high-field data.

Although the detailed R versus T has not been measured for the Mn-implanted GaMnAs: Zn NWs, it is still noticeable that the hopping length and activation energy at 1.6 K are quite similar for NWs with and without Zn, and also, with quite different Mn-concentrations (0.1% Mn compared to 5% Mn). Although more measurements are needed to confirm any predictions, our results imply that the defect landscape experienced by the charge carriers is fairly similar for the different types of NWs discussed above. However, as discussed in the next chapter, the influence of magnetic field on the hopping transport is vastly different for the different samples indicating the importance of Mn-related defects on the transport.

6.3 Thermoelectric characterization of GaMnAs nanowires

This section outlines the measurements and analysis of the thermopower and conductance of $Ga_{1-x}Mn_xAs$ (x = 5%) NWs of 40nm diameter.

The thermopower, or Seebeck effect, is the occurrence of a voltage gradient ΔV along a sample exposed to a temperature gradient ΔT. The so-called Seebeck coefficient (S) is defined as

$$S = -\frac{\Delta V}{\Delta T}. \tag{6.13}$$

If S is positive, the sample end with the higher temperature has the lower potential, and vice-versa. Thus, the voltage gradient in the material is opposite to the temperature gradient. In *p*-type semiconductors, where holes are majority carriers, S is positive, and in *n*-type semiconductors, where electrons are majority carriers, S is negative.

A microscopic picture of the Seebeck effect is that a temperature gradient creates a particle flow form hot to old, which establishes a voltage difference, whereby the charge carriers diffuse from the hot to the cold end of the sample. This causes a difference in charge between the two ends and consequently a voltage difference (gradient). The semiclassical diffusive thermopower can be described by Mott's law [87]

$$S_{\text{diff}} = -\frac{\pi^2 k_B m^*}{(3\pi^2)^{2/3}\hbar^2|e|}\frac{T}{n_h^{2/3}}, \tag{6.14}$$

where $\hbar$ is the reduced Planck constant, and n_h is the carrier concentration and m^* is the hole or electron effective mass [88].

In a paramagnetic regime, the thermopower Eq. 6.14 is not complete (even without taking into account hopping transport).

Eq. 6.15 shows that in paramagnetic regime, the thermopower consists of the following two terms:

$$S = S_{\text{diff}} + S_{\text{exch}}, \tag{6.15}$$

where

$$S_{\text{exch}} = \underbrace{\left(\frac{4\pi^2 k_B}{e} N(E_F) I_{pd} V \frac{\rho_{\text{exch}}}{\rho} \right)}_{S_0} \left(\frac{T}{T + T_0} \right), \tag{6.16}$$

and I_{pd} is the exchange integral between carriers and magnetic centers, V is the nonmagnetic scattering potential, ρ_{exch}/ρ is the ratio between exchange contributions to the resistivity and total resistivity, and T_0 is a material-dependent parameter with weak temperature and magnetic impurity dependence, which amounts to about 150 K for thin-films [89].

In disordered semiconductors, hopping conduction is another important mechanism that needs to be considered in the thermopower Eq 6.15. After inclusion of this factor, the thermopower is given by

$$S_{\text{tot}} = S_{\text{diff}} + S_{\text{exch}} + S_{\text{hop}}. \tag{6.17}$$

The hopping term is suggested to be of the form [89]

$$S_{\text{hop}} = \left(F_{\text{corr}} \frac{k_B}{e} \right) \left(\frac{\Delta E}{k_B T} + A \right), \tag{6.18}$$

where A is a constant without significant temperature-dependence and includes an additional factor, F_{corr}, to account for electron correlations. Without F_{corr}, Eq. 6.18 expresses that, in the simple case of single particles, i.e., non-interacting transport, the thermopower of a device essentially measures the average energy (here assumed to be the activation energy ΔE) associated with the transport.

In order to confirm the carrier type and to determine the carrier concentration of a single $Ga_{1-x}Mn_xAs$ NW (x = 5%) of 40nm diameter, the temperature-dependence of the thermopower and resistance of our devices were studied from 60 K to 300 K. As shown in Figure 6.11, the data implies that VHR may likely be at play [3, 90]. Deviation from a straight line occurs around $T^{-1/4}$ = 0.32 or T ~ 95 K. From this data, a carrier concentration of approximately 3×10^{18} cm^{-3} is deduced. Furthermore, a hopping length of about 11 nm and a hopping energy of ΔE = 62 meV at 100 K is extracted. In Section 6.2, similar behavior is found for larger 80 nm diameter nanowires, though the hopping transport was found to persist down to T ~ 50 K [3].

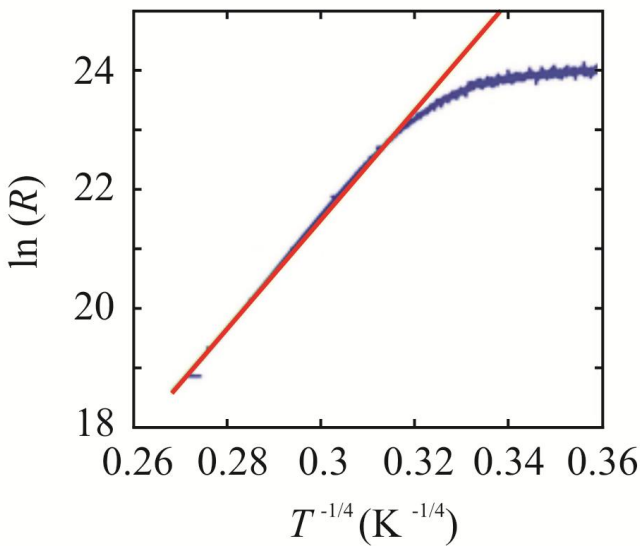

Figure 6.11: Experimental $ln(R)$ versus $T^{-1/4}$ data (blue dots) for a single $Ga_{1-x}Mn_xAs$: Zn (x = 5%) NW device of 40 nm diameter.

Figure 6.12 shows the measured thermopower, where the positive sign indicates that the charge carriers are holes. A *p*-type NW is expected since substitutional Mn is an acceptor in GaAs.

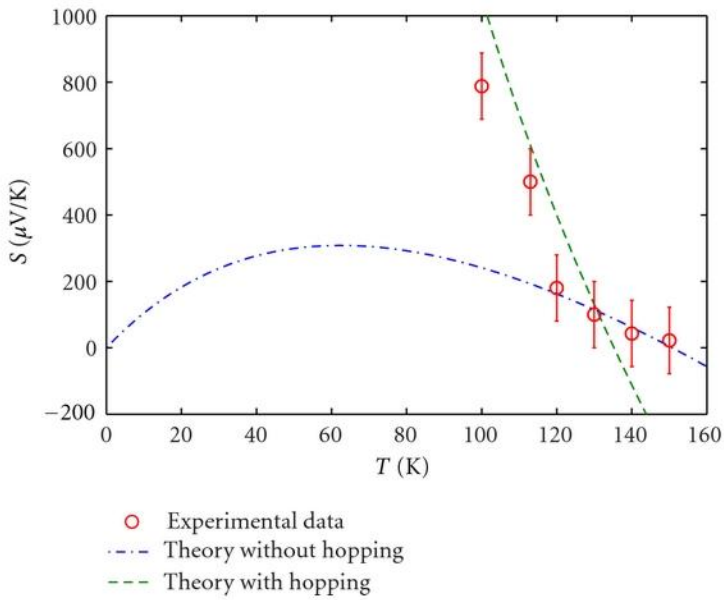

Figure 6.12: Thermopower for a single $Ga_{1-x}Mn_xAs$: Zn (x = 5%) NW device of 40 nm diameter, as a function of temperature. The experimental data matches well at high temperatures with values calculated using a model without hopping [89]. Below 120 K, the nanowire thermopower deviates strongly from the model without hopping. Addition of a hopping term qualitatively accounts for the rise in thermopower [4].

By plotting the thermopower versus T^{-1} (Figure 6.13), and using the correlation factor, $F_{\text{corr}} \sim 5$, an activation energy of $\Delta E \sim 63$ meV is extracted, in good agreement with that one deduced from the plot of ln(R) versus $T^{-1/4}$ in Figure 6.11. Based on this was calculated the full theoretical line using Eq.

6.17, and fitted the model to the experimental data as shown in Figure 6.12 (green-dashed line). The inclusion of this hopping mechanism indeed explains the observed rise in thermopower below 120 K. Further discussions can be found in [4].

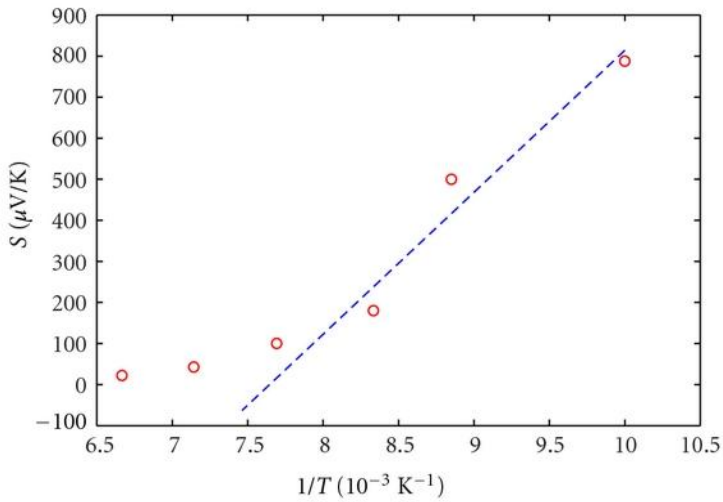

Figure 6.13: Thermopower versus 1/T, plotted together with blue-dashed fitting line used to extract the hopping activation energy. Further discussion can be found in [4].

Chapter 7

Magnetoresistance in Mn ion-implanted GaAs nanowires

This chapter presents a brief discussion of the magnetotransport results obtained for single-crystalline Mn ion-implanted GaAs NWs. The investigated NWs exhibit very different dependence of the magnetoresistance (MR) on Mn content, both with respect to magnitude and sign. Firstly, a large negative magnetoresistance (MR) was observed in $Ga_{1-x}Mn_xAs$ and $Ga_{1-x}Mn_xAs$: Zn nanowires (x = 5%) [2, 5, 6]. These results were interpreted in terms of spin-dependent hopping conduction through a landscape of magnetic polarons and spin glass textures. Secondly, a spin-split two-band model was proposed to explain the small positive magnetoresistance observed in GaAs: Zn and $Ga_{1-x}Mn_xAs$: Zn nanowires (x = 0.0001%) [6]. Finally, hopping conduction was studied in $Ga_{1-x}Mn_xAs$: Zn nanowires (x = 0.1%) [6], where a significant positive MR was observed and explained in terms of magnetic compression of wavefunctions of impurity states.

7.1 Large negative MR in $Ga_{1-x}Mn_xAs$ and $Ga_{1-x}Mn_xAs$: Zn NWs (x = 5%)

In this section a description of theoretical models is given that describes the large negative MR observed in $Ga_{1-x}Mn_xAs$ and $Ga_{1-x}Mn_xAs$: Zn NWs with 80nm diameter and with x = 5%.

A magnetic polaron is a kind of magnetic bubble that consists of a spin-polarized carrier that interacts with surrounding spin-carrying impurities, e.g., magnetic ions via exchange interactions. In general, the evidence of bound magnetic polarons is more accepted than that for free magnetic polarons [91]. Bound magnetic polarons (BMPs) appear when the carriers are localized, for example, because they are bound to a donor or to an acceptor. The BMP then originates from the exchange interaction between the localized carrier and the spins of the surrounding magnetic ions [92].

Spin glasses are disordered magnetic systems where the interaction between the localized magnetic moments can be both ferromagnetic and antiferromagnetic with approximate equal frequency. These competing interactions lead to a frustrated magnetic ground state, typically due to some kind of frozen-in structural disorder. Thus no conventional long-range ferromagnetic or anti-ferromagnetic ordering can be established. Instead, these systems exhibit a "freezing transition" to a state with a new type of ordering, in which the spins are aligned in random directions [93].

Kaminski and Das Sarma [94] have proposed a magnetic polaron percolation model to explain the magnetotransport properties of DMSs exhibiting a strong insulating character. This model assumes a heavily compensated material with both strongly localized charge carriers and a random spatial distribution of magnetic impurities. The strong exchange interaction between localized holes and magnetic impurities leads to the formation of BMPs. Yuldashev et al. [95] used a polaron model to estimate the critical concentration of holes required to form a ferromagnetic phase in (GaMn)As thin-films co-doped with Te donors. It was demonstrated that an increased Te-concentration (compensation) gradually reduces T_C, eventually

replacing the long-range ordered ferromagnetic state with a paramagnetic-to spin-glass phase.

In most magnetic insulators the exchange interaction between magnetic ions can be described by the Heisenberg model

$$H = \sum_{j,k} J_{jk} S_j S_k, \tag{7.1}$$

where the nearest-neighbor coupling J_{jk} is usually dominant, and effectively represents direct, indirect and super-exchange interaction [96].

For the present case, the antiferromagnetic exchange interaction between a magnetic ion and the spin of a localized hole is described by the Heisenberg Hamiltonian

$$H = -J_0 \sum_{j,k} s_j S_k, \tag{7.2}$$

where J_0 is the (negative) exchange energy between a magnetic ion and the localized hole, and s_j and S_k are the absolute values of the hole and impurity spins, respectively.

In the mean-field approximation of the Heisenberg Hamiltonian, the energy for a cluster of magnetic ions surrounding a single spin-polarized hole localized at point j can be written as

$$E_j = -J_0 s_{h_j} \sum_{k}^{N} S_k \tag{7.3}$$

$$E_j = -J_0 s_{h_j} N \langle S \rangle, \tag{7.4}$$

where N is the number of nearest-neighbor impurity spins and the average nearest-neighbor polarization $\langle S \rangle$ is given by

$$\langle S \rangle = S\beta\left(\frac{g_i S \mu_B B}{k_B T}\right), \tag{7.5}$$

where g_i is the impurity gyromagnetic ratio, μ_B is the Bohr magneton and B is the external magnetic field. The Brillouin function $\beta_S(x)$ is defined by

$$\beta_S(x) \equiv \frac{2S+1}{2S}\coth\left(\frac{2S+1}{2S}x\right) - \frac{1}{2S}\coth\left(\frac{1}{2S}x\right) \tag{7.6}$$

with

$$x = \frac{g_i S \mu_B B}{k_B}\frac{1}{T}. \tag{7.7}$$

By inserting Eq. 7.5 into Eq. 7.4, the single hole energy at point j becomes

$$E_j = -J_0 s_{h_j} NS\beta\left(\frac{g_i S \mu_B B}{k_B T}\right). \tag{7.8}$$

The physical picture emerging from Chapters 3 and 6 [2 - 6] is the one of a system composed of relatively few quasi-localized holes, each surrounded by a large number of Mn impurities. In this regime, the possible onset of a ferromagnetic transition can be analyzed by means of a theoretical model of magnetic polarons, proposed by Kaminski et al. [94]. According to this model, the exchange interaction between carriers (holes) and magnetic impurities leads to the formation of BMPs, consisting of individual localized holes surrounded by magnetic impurities, whose magnetic moment is anti-ferromagnetically coupled to the hole magnetic moment.

Figure 7.1 shows temperature-dependent zero-field-cooled (ZFC) and field-cooled (FC) magnetization curves of large $Ga_{1-x}Mn_xAs$ NW ensembles (80nm, x = 5%) deposited on an insulating Si/SiO_x substrate. In the temperature range 20 K < T < 100 K, the magnetization is the same for both cases, and it

increases with decreasing temperature. Interestingly, the two curves start to diverge below 20 K, and while the ZFC magnetization goes rapidly to zero, the FC does not and in fact shows a hint of further increasing with decreasing temperature. Also, it is observed that the peak temperature, the so-called blocking temperature, in ZFC curves decreases with increasing magnetic field strength. The divergence of FC and ZFC curves is less pronounced at increasing field strength, and completely vanishes at applied fields > 20 mT. This behavior is commonly associated with a phase transition from a paramagnetic state to a spin-disordered or spin-glass state in DMSs [97] and in semi-insulating $Ga_{1-x}Mn_xAs$ thin-films [95].

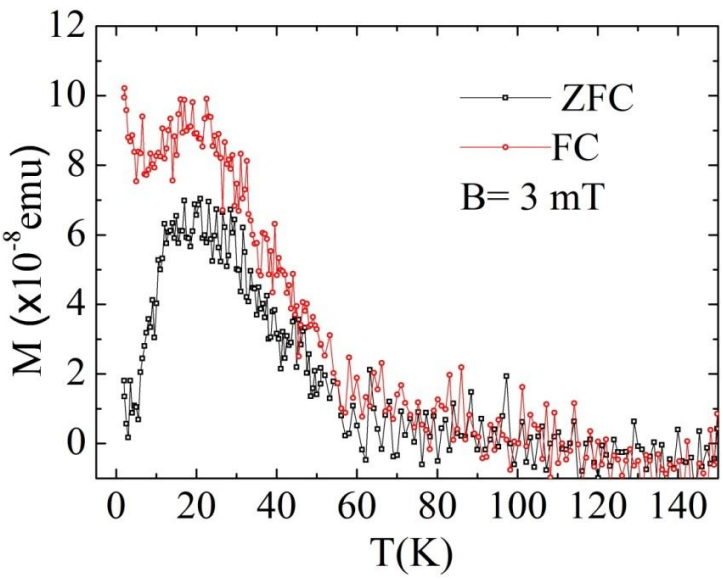

Figure 7.1: Temperature-dependent ZFC and FC magnetization curves of $Ga_{1-x}Mn_xAs$ NW ensembles with 80nm diameter and x = 5% at an applied magnetic field of 3mT perpendicular to the substrate surface with deposited NWs [5].

Figure 7.2 shows the temperature-dependence of the resistance of a typical single $Ga_{1-x}Mn_xAs$ NW (80nm, x = 5%). Evidently there is a small kink in the resistance at T ~ 16 K, which is close to the peak temperature observed in Figure 7.1. Thus, the peaks observed in the resistance and in the magnetization curves might be associated with some kind of magnetic transition.

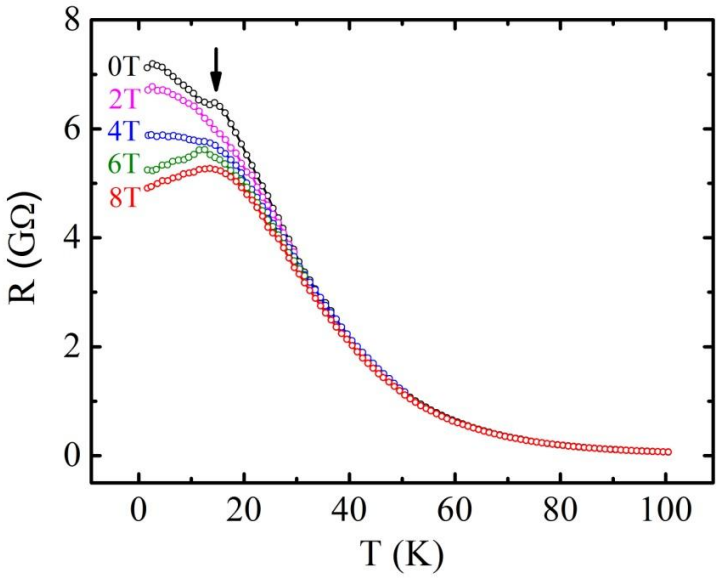

Figure 7.2: Magnetoresistance traces for a single $Ga_{1-x}Mn_xAs$ NW with 80 nm diameter and x = 5% at 0T, 2T, 4T, 6T and 8T, respectively. Arrow at 0 T line indicates a transition from a high-temperature paramagnetic to low-temperature spin-glass phase. The local maximum observed in the 8 T line possibly signals the onset of a weak ferromagnetic phase.

In order to interpret this phenomenon, the BMP model must be somewhat modified [98] to the case of a very low hole concentration where the average distance between two localized holes, that is, the distance between the centers of two distinct adjacent polarons, is large. The radius of a BMP, containing magnetic impurities all aligned along the opposite direction of the

hole spin, increases with decreasing T. However, the radius can clearly not increase indefinitely by decreasing T. Beyond a certain size L, the long-range exchange coupling between the hole spin and impurity spins far away from the polaron center becomes comparable to the relatively weaker direct exchange interaction between nearby impurities, which is usually anti-ferromagnetic. The interplay between these two competing interactions in the intermediate regions between magnetic polarons prevents the onset of long-range order and can result in a spin-disordered ground state. In this scenario, well-defined BMPs are still present, but they are separated by large intermediate unpolarized regions where the impurity spins at low-temperature freeze into a spin-glass-like state.

A phenomenological model is proposed, incorporating the ideas above, which is able to capture the decrease of the resistance at finite magnetic fields and elevated temperatures, and in addition, provides insight into which mechanism is most likely responsible for the negative MR. In the presence of a magnetic field, the hopping of a hole is assumed to have an activation form

$$R \propto \exp\left(\frac{\Delta E}{k_B T}\right), \tag{7.9}$$

where ΔE is the change of the hopping energy with magnetic field. It is further postulated that ΔE is proportional to the interaction energy between the spin of the hole s and an average spin $\langle S \rangle$ of a magnetic object, which can represent a magnetic polaron or Mn ion in the unpolarized region. Since both mechanisms are relevant, the spin angular momentum S of the magnetic object is left as a variable parameter in our model. Although the value of the interaction energy is also not known, it is taken proportional to the only energy scale in our problem that is the exchange interaction between (J_0) the hole and the

magnetic object. To account for the presence of BMPs, it is assumed that the hopping distance might still be regulated by the effective hole (and indeed polaron) separation, and therefore ΔE will be proportional to n_h. The hopping event is also likely to be proportional to the typical interaction range of the hole wavefunction a_B. Finally, the average spin of the magnetic object in the presence of a magnetic field is given by Equation (7.5).

Then, a possible form of ΔE is therefore

$$\Delta E = -A\frac{4\pi}{3}a_B^3 n_h J_0 sS\beta\left(\frac{gS\mu_B B}{k_B T}\right), \tag{7.10}$$

where A is constant. The resulting magnetic field-dependence of the resistance is given by

$$R(B,T) = R(0,T)\exp\left[-A\frac{4\pi a_B^3 n_h J_0 sS}{3k_B T}\beta\left(\frac{gS\mu_B B}{k_B T}\right)\right], \tag{7.11}$$

In Figure 7.3 is shown the result of the fitting of Eq. 7.11 to the measured resistance data for different values of the magnetic field [4]. Interestingly, the best fitting for all relevant values of the magnetic field is obtained for S = 5/2 (spin of single Mn impurity).

Also, the fitting predicts that the negative MR should saturate at B ~ 20 T. Furthermore, at 100 K all the MR signal has disappeared even in the presence of a magnetic field of 8 T. The fitting performs remarkably well in the temperature range roughly between 20 and 100 K, but fails to predict the MR below 20 K where a glitch in the experimental data signals the aforementioned phase transition. Figure 7.3 suggests that above the spin-glass transition temperature, $R(B,T)$, can be described mainly by a paramagnetic state of magnetic impurities in the intermediate regions between BMPs, while below the transition temperature the system enters into a spin-glass state. In the

presence of a strong magnetic field, the transition to a spin-glass state is transformed to a transition into a state that is most likely close to being ferromagnetic. This is brought about by the alignment of the impurity spins in the intermediate regions, as well as the magnetic moments of the polarons. Equation (7.11) can also be used to calculate the expected MR ratio versus magnetic field.

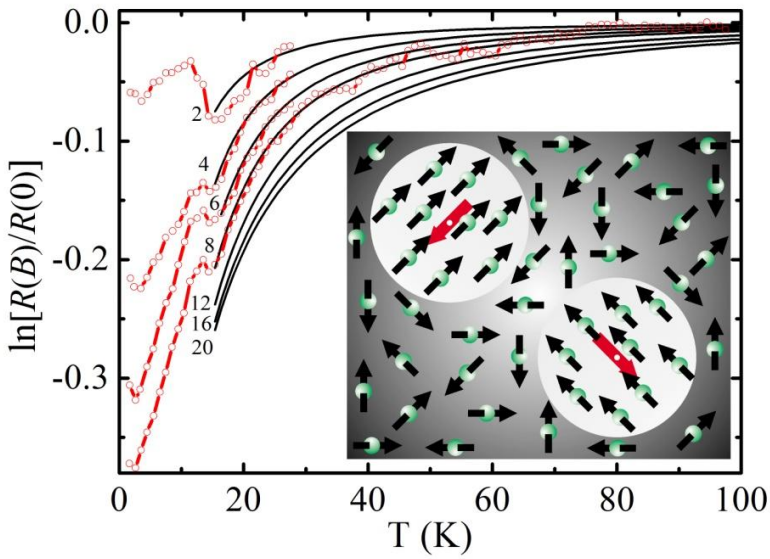

Figure 7.3: Red lines show experimental magnetoresistance ratios at 2T, 4T, 6T and 8T, respectively, for a single $Ga_{1-x}Mn_xAs$ NW with 80 nm diameter and x = 5%. Black lines correspond to theoretical curves at different magnetic fields from 2 to 20T, calculated from Eq. 7.11. Inset shows a schematic picture of two BMPs (white circles). The black and red arrows show impurity and hole spins, respectively.

Figure 7.4 [5] shows the temperature-dependence of the magnetoresistance defined as $\mathrm{MR}(\%) = \dfrac{R(B,T) - R(0,T)}{R(0,T)} \times 100$, where $R(B,T)$

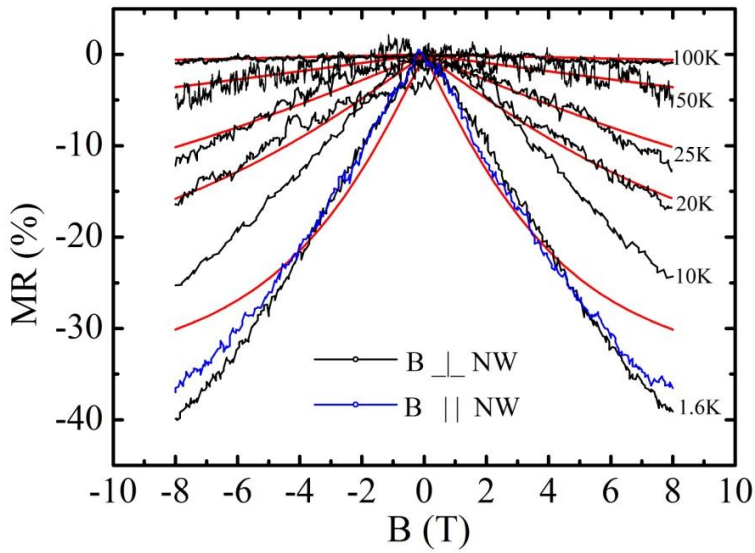

Figure 7.4: Magnetoresistance (black) lines recorded for a single $Ga_{1-x}Mn_xAs$ NW (x = 5%) with the magnetic field applied perpendicular to the NW. Red lines are theoretical MR curves calculated from Eq. 7.11 (10−100K). The blue line shows the corresponding temperature-dependence of the magnetoresistance with the magnetic field applied parallel to the NW (1.6 K).

is the resistance at magnetic field strength B. Evidently, there is a good agreement between experiment and theory for temperatures above 20 K. At lower temperatures, there is a significant deviation related to the phase transition discussed above. There is a large negative MR reaching 40% at 8 T. Furthermore, MR data for magnetic fields applied perpendicular and parallel to a NW, respectively, display no significant differences as also shown in Figure 7.4. The observed MR is about 10 times larger than typically observed in metallic GaMnAs thin-films [60, 99], pointing to the fact that strong spin-dependent scattering mechanisms are involved in hopping transport in comparison to valence band transport.

To increase the ferromagnetic coupling after Mn implantation, heavy p-type NWs were fabricated by in-situ doping with Zn as previously discussed. For $Ga_{1-x}Mn_xAs$: Zn nanowires (x = 5%), a negative MR was observed that increased to a more or less saturated value of about 85% at 8T and 1.6K. This remarkably large MR is almost twice as large as observed for NWs with similar Mn-concentration, but without Zn doping as seen in the comparative plot in Figure 7.5.

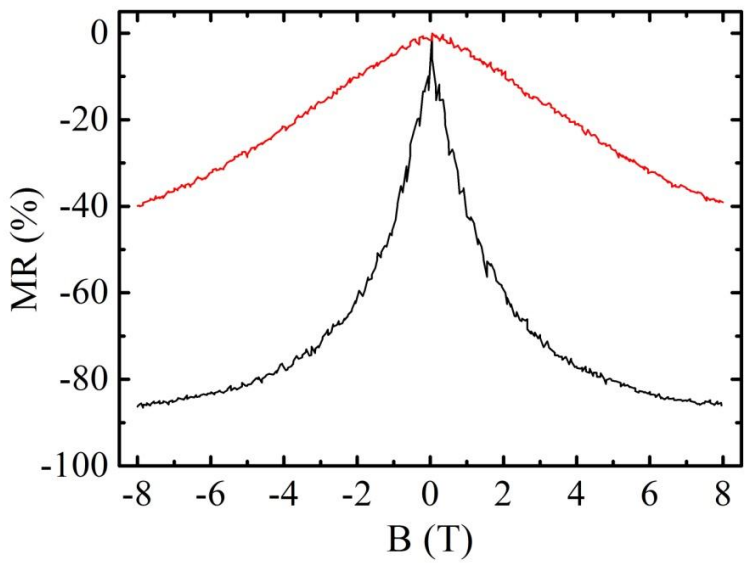

Figure 7.5: Magnetoresistance curve for a single $Ga_{1-x}Mn_xAs$: Zn NW (x = 5%) (black line) plotted together with data for a single $Ga_{1-x}Mn_xAs$ NW (x = 5%) (red line). All MR curves are taken with the magnetic field perpendicular to the NW at 1.6K [6].

Figure 7.6 shows meticulous resistance measurements for perpendicular orientation of the magnetic field relative to a $Ga_{1-x}Mn_xAs$: Zn NW (x = 5%). A comparison between both sweep directions reveals a small hysteresis. Similar magnetotransport measurements were carried out on similar NWs (x = 5%)

without Zn doping for which no hysteresis effect was observed [5]. This important result is interpreted as the presence of a weak ferromagnetic phase in the NWs. For both samples, $Ga_{1-x}Mn_xAs$ and $Ga_{1-x}Mn_xAs$: Zn NWs (x = 5%), the transport data are interpreted in terms of strongly spin-dependent hopping mechanisms involving magnetic polarons and large partially ordered intermediate regions of Mn impurity spins.

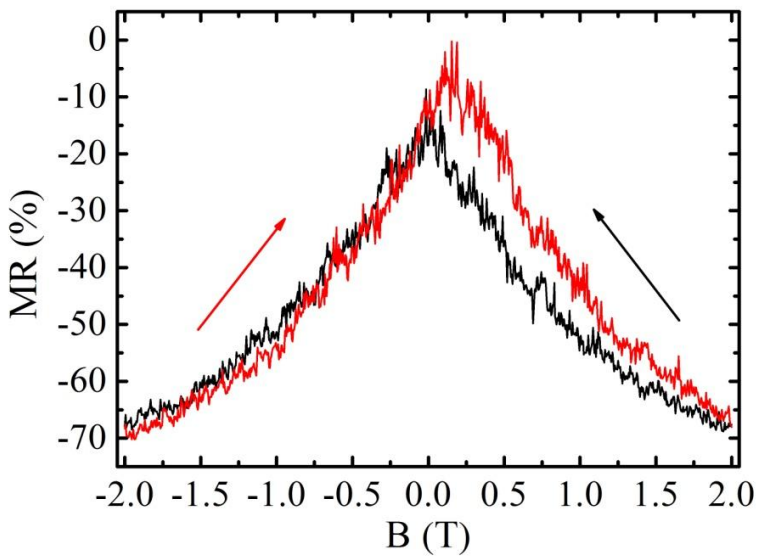

Figure 7.6: Detailed magnetoresistance curves for a single $Ga_{1-x}Mn_xAs$: Zn NW (x = 5%), recorded for two sweep directions (red line: -2T→2T, black line: 2T→ -2T) revealing a weak hysteresis. All MR curves are taken with the magnetic field perpendicular to the NW at 1.6K [6].

7.2 Small positive MR in GaAs: Zn and $Ga_{1-x}Mn_xAs$: Zn NWs (x = 0.0001%)

Another group of samples that are interesting to investigate are strongly diluted NWs. For this were fabricated and processed reference GaAs: Zn NWs

and strongly diluted $Ga_{1-x}Mn_xAs$: Zn NWs (x = 0.0001%), with a diameter of 80nm and a Zn-concentration of about 10^{19} cm^{-3} [6]. Figure 7.7 shows the $I-V$ characteristics for the two different sample types measured in a four-probe configuration at room temperature and at 1.6K. The linear behavior of the $I-V$ implies that when the Mn-concentration is much lower than the Zn-concentration, there are enough holes in the NWs to sustain a high conductivity. Both types of samples exhibit a weak, saturating positive MR of a few percent.

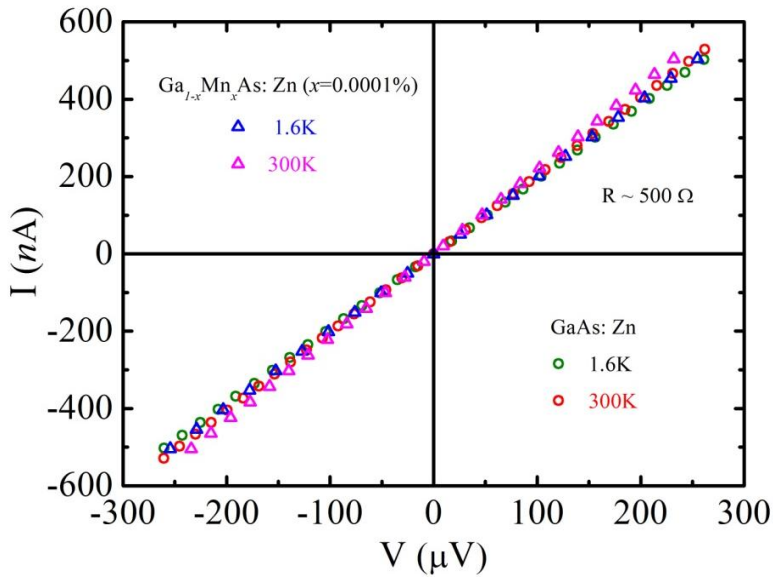

Figure 7.7: $I-V$ characteristics of GaAs: Zn (circles) and $Ga_{1-x}Mn_xAs$: Zn NWs with x = 0.0001% (triangles) at 1.6K and 300K, respectively.

To explain the positive MR, a two-band model is proposed that was previously invoked for magnetic bulk and thin-film semiconductors [100 - 102]. In this model, the positive MR originates from the effect of the Lorentz force on mobile carriers in a spin-split band, as schematically shown in Figure

7.8. In the present case, the spin-split band most likely originates from a Zn-related impurity band, formed by the high Zn-concentration, mixed with the heavy hole valence band. From temperature-dependent resistance measurements, it is concluded that the free holes do not significantly freeze out even at 1.6K at which kT << 30 meV (binding energy of the Zn-related acceptor in GaAs) [88].

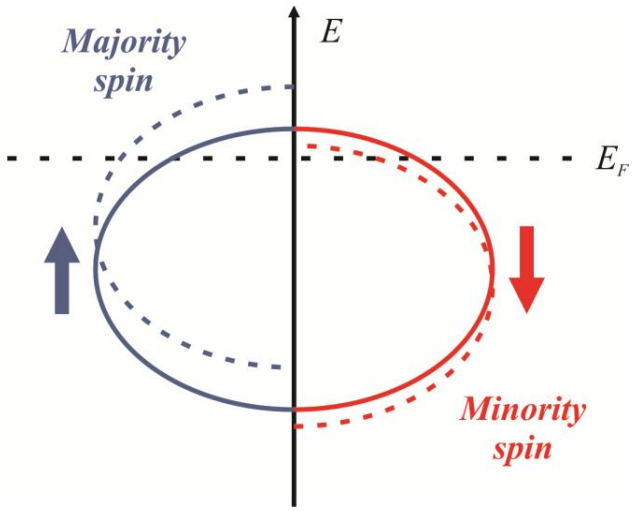

Figure 7.8: Schematic diagram of the Zeeman-split impurity band with indicated position of the Fermi level.

The field-induced change in density of states results in different populations of the two spin-split sub-bands with different conductivity and mobility for majority and minority spin carriers, respectively. Increased scattering of spin-polarized carriers due to band splitting leads to the observed positive MR. Analysis based on such a model shows that the positive MR is given by [100]

$$\frac{R-R_0}{R_0}=\frac{A_1^2B^2}{1+A_2^2B^2}, \tag{7.12}$$

where R_0 is the resistance at zero magnetic field, R is the resistance at magnetic field B, and the parameters A_1 and A_2 are related to the conductivity and mobility of carriers in the two sub-bands. The parameters A_1 and A_2 are

$$A_1^2 = \frac{\sigma_u \sigma_d (\mu_u + \mu_d)^2}{(\sigma_u + \sigma_d)^2}, \tag{7.13}$$

$$A_2^2 = \frac{(\sigma_u \mu_d - \sigma_d \mu_u)^2}{(\sigma_u + \sigma_d)^2}, \tag{7.14}$$

where μ_i and σ_i are the mobilities and conductivities of the carriers, and the subscripts u and d denote the majority-spin and minority-spin carriers. The relative population of carriers in these two bands is determined by the spin splitting, i.e., the magnetic field and the temperature [103].

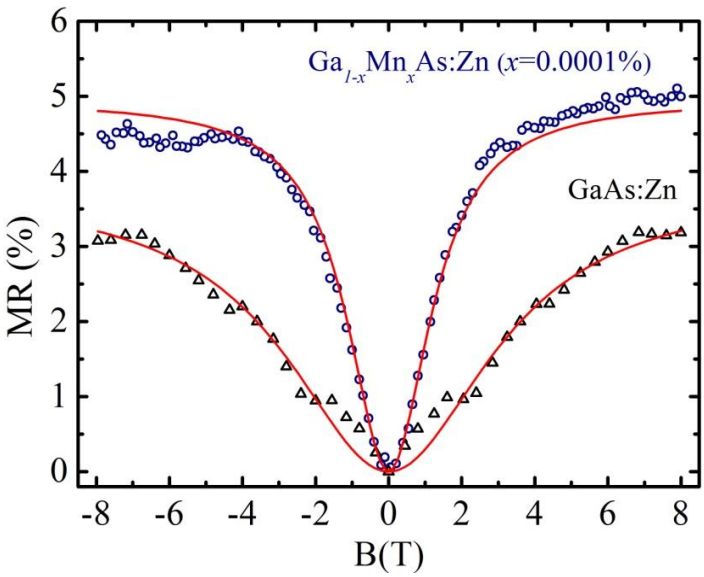

Figure 7.9: MR curves for GaAs: Zn and $Ga_{1-x}Mn_xAs$: Zn NWs (x = 0.0001%) at 1.6K. Black and blue symbols are the experimental data, while the red solid lines are theoretical fittings using Eq. (7.12).

The MR described by Eq. 7.12 is quadratic at low fields, and saturates at high fields. The data for samples GaAs: Zn and $Ga_{1-x}Mn_xAs$: Zn NWs (x = 0.0001%) fitted to Eq. 7.12 are shown in Figure 7.9. The positive MR observed in both cases amounts to a few percent and no hysteresis is observed.

7.3 High positive MR in $Ga_{1-x}Mn_xAs$: Zn NWs (x = 0.1%)

In order to understand the larger positive magnetoresistance exhibited by similar $Ga_{1-x}Mn_xAs$: Zn NWs with x = 0.1%, the magnetic compression of the wavefunctions of impurity states, available for carrier hopping conduction, must be taken into account. It is well known that, in a high magnetic field, the wavefunctions of impurities are compressed in the transverse direction leading to high positive MR in, e.g., *n*-GaAs [104 - 108]. Wavefunctions spherically symmetric in the absence of a magnetic field become cigar-shaped in a magnetic field, as schematically shown in Figure 7.10. Such a compression leads to a decrease in the overlap of the wavefunction "tails" for an average pair of neighboring impurities, and consequently to an exponential increase in resistivity. An exponential positive magnetoresistance is often considered as evidence for the importance of the "tails" of the wavefunctions, and of transport dominated by hopping [80].

Mikoshiba [109] was the first to demonstrate that the exponential magnetic field-dependence of the resistivity is different in the cases of strong and weak fields. Shklovskii [110 - 113] has presented a magnetoresistance theory based on the percolation method. In the weak field case, Shklovskii's results differ from those of Mikoshiba by a numerical factor in the resistivity exponent, whereas in the strong field case they lead to qualitatively different dependences on the magnetic field and on the impurity concentration.

Here is presented a brief overview of Shklovskii's MR results. The effect of the magnetic field on the wavefunctions is investigated by solving the Schrödinger equation for the electronic envelope wave function $\psi(r)$ in the Coulomb field of a donor and external magnetic field [114]:

$$-\frac{\hbar^2}{2m}\left[\frac{1}{\rho}\frac{\partial}{\partial\rho}\left(\rho\frac{\partial\psi(r)}{\partial\rho}\right)+\frac{\partial^2\psi(r)}{\partial z^2}+\frac{1}{\rho^2}\frac{\partial^2\psi(r)}{\partial\phi^2}\right]+\ldots$$
$$\ldots-\frac{ie\hbar B}{2mc}\frac{\partial\psi(r)}{\partial\phi}+\frac{eB^2}{8mc^2}\rho^2\psi(r)-\frac{e^2\psi(r)}{kr}=E\psi(r). \quad (7.15)$$

All terms containing $\partial/\partial\phi$ disappear for the ground state wavefunction due to its cylindrical symmetry in the presence of a magnetic field, leading to the simplified equation

$$-\frac{\hbar^2}{2m}\left[\frac{1}{\rho}\frac{\partial}{\partial\rho}\left(\rho\frac{\partial\psi(r)}{\partial\rho}\right)+\frac{\partial^2\psi(r)}{\partial z^2}\right]+\frac{\hbar^2\rho^2}{8m\lambda^4}\psi(r)-\frac{e^2}{kr}\psi(r)=E\psi(r), \quad (7.16)$$

where the magnetic length λ is

$$\lambda=\left(\frac{c\hbar}{eB}\right)^{1/2}. \quad (7.17)$$

The magnetic field introduces an additional magnetic potential energy term, $\hbar^2\rho^2/8m\lambda^4$, which acts as a spring pulling the electron to the z-axis (Figure 7.10).

For a sufficiently weak field, λ is large (Eq. 7.17) and equation (7.16) includes a small magnetic potential that does not significantly affect the electron wavefunction. Thus the magnetic field should not affect the ground state energy. In the opposite case, considering a strong magnetic field, λ is small and the magnetic potential is large enough to significantly alter the

electron wavefunction and localize an electron in a narrower region in the transverse direction.

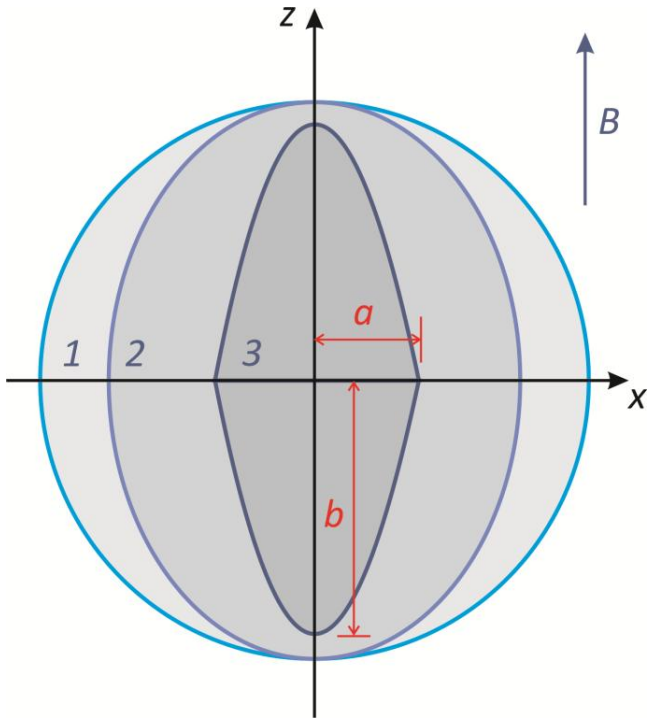

Figure 7.10: Evolution of the wavefunction surface as the magnetic field is varied: (*1*) $B = 0$; (*2*) weak magnetic field and (*3*) strong magnetic field [80].

At low temperatures, where hopping distances are large enough, a positive MR arises from the above-mentioned magnetic compression of the wavefunctions of impurity states available for hole-hopping events. This deformation of the wavefunctions leads to an effective increase in the hopping length, and thus to an increased resistance. The MR varies with magnetic field according to [80, 115, 116]:

$$R(B) = R(0)\exp(A \cdot B^{\gamma}). \tag{7.18}$$

where A is a constant and $\gamma = 2$ for low to moderate magnetic fields and $0.25 \leq \gamma \leq 0.6$ for strong magnetic fields.

As discussed in Chapter 6, $Ga_{1-x}Mn_xAs$: Zn NWs (x = 0.1%) are governed by hopping conduction mechanisms. Following the arguments above, a significant positive magnetoresistance is therefore expected with a field-dependence that agrees with Eq. 7.18. Figure 7.11 shows the experimental MR from – 8T to 8T. The MR increases with applied magnetic field without saturating even at 8T, and with no signs of any hysteresis effects. Figure (7.12) shows the same MR data plotted in a log-double log format. A quadratic dependence is readily observed up to B ~ 4T. At higher magnetic field strengths, the MR displays a pronounced deviation towards a weaker (linear) field-dependence [6].

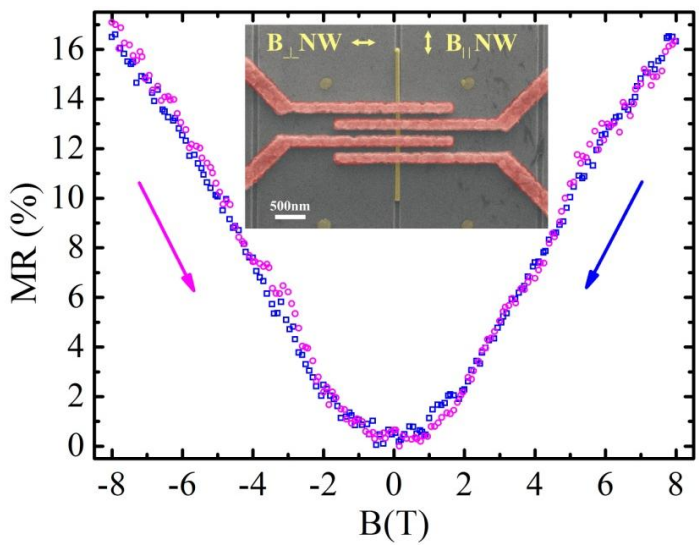

Figure 7.11: MR curves for a single $Ga_{1-x}Mn_xAs$: Zn NW (x = 0.1%) at 1.6K for two sweep directions (magenta circles: -8T→8T, blue squares: 8T→ -8T). Inset shows SEM image of single NW provided with contacts for 4-probe measurements.

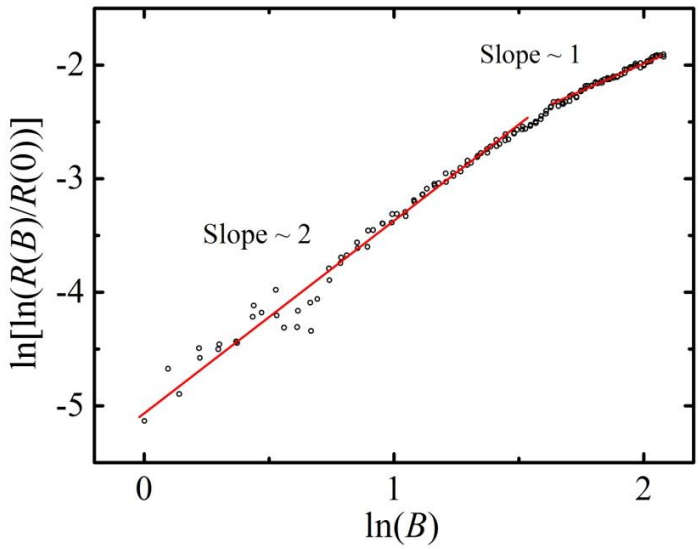

Figure 7.12: Log-double log plot of the resistance versus magnetic field for a single $Ga_{1-x}Mn_xAs$: Zn NW (x = 0.1%) at 1.6K, clearly showing a quadratic dependence at low magnetic field strengths and a weaker linear dependence at high magnetic field strengths.

Outlook

In this thesis were successfully demonstrated fabrication and characterization of a new type of very interesting spintronic nanomaterial compatible with silicon technology. To this point, however, the effective hole concentration is not large enough to form ferromagnetically ordered NWs. In the near future, the main emphasis will therefore be on optimizing the implantation, annealing and in-situ doping to enhance the hole concentration. Successfully developed ferromagnetic NWs opens up the possibility for electrically tuning the hole concentration, and thus the ferromagnetic ordering, by an effective wrap-gate around the NW. The possibility to tune the magnetic phase on demand between paramagnetic and ferromagnetic limits offers a completely new playground to study magnetic properties at the nanoscale. Such electrically gated NWs would provide the basis for semiconductor nanospintronics, e.g., solid-state memories and spin-FETs operating at elevated temperatures. Other interesting future research directions deal with the precise implantation of Mn-doped heterostructure segments/superlattices along NWs, as well as the implantation of single Mn ions into NWs with unprecedented spatial resolution for solotronics. A deeper understanding of the electronic structure of Mn incorporated into different crystal phases of GaAs, as well as into other III-V materials, e.g., InP and GaN, is also of great interest.

References

[1] Sze, S. M. *Semiconductor devices: Physics and Technology*. Wiley, New York, **2002**.

[2] Borschel, C.; Messing, M. E.; Borgström, M. T.; Paschoal Jr., W.; Wallentin, J.; Kumar, S.; Mergenthaler, K.; Deppert, K.; Canali, C. M.; Pettersson, H.; Samuelson, L. and Ronning C. *A New route toward semiconductor nanospintronics: Highly Mn-doped GaAs nanowires realized by ion-implantation under dynamic annealing conditions*. Nano Letters 11, 3935 – 3940, **2011**.

[3] Paschoal Jr., W.; Kumar, S; Borschel, C.; Wu, P.; Canali, C. M.; Ronning, C.; Samuelson, L.; and Pettersson, H. *Hopping conduction in Mn ion-implanted GaAs nanowires*. Nano Letters, 12, 4838 − 4842, **2012**.

[4] Wu, P.; Paschoal Jr., W.; Kumar, S.; Borschel, C.; Ronning, C.; Canali, C. M.; Samuelson, L.; Pettersson, H.; Linke, H. *Thermoelectric characterization of electronic properties of GaMnAs nanowires*. Journal of Nanotechnology, 2012, 480813, **2012**.

[5] Kumar, S.; Paschoal Jr., W.; Johannes, A.; Jacobsson, D.; Borschel, C.; Pertsova, A.; Wang, C-H; Wu, M-K; Canali, C. M.; Ronning, C.; Samuelson, L. and Pettersson, H. *Magnetic polarons and large negative magnetoresistance in GaAs nanowires implanted with Mn ions*. Nano Letters, 13, 5079 − 5084, **2013**.

[6] Paschoal Jr, W.; Kumar, S.; Jacobsson, D.; Johannes, A.; Jain, V.; Canali, C. M.; Pertsova, A.; Ronning, C.; Dick, K. A.; Samuelson, L. and Pettersson, H. *Magnetoresistance in Mn ion-implanted GaAs:Zn nanowires*. Submitted to Applied Physics Letters, February **2014**.

[7] Flory, F.; Escoubas, L.; and Berginc, G. *Optical properties of nanostructured materials: A review.* Journal of Nanophotonics, 5, 052502, **2011**.

[8] Wan, Y.; Sha, J.; Chen, B.; Fang, Y; Wang, Z; and Wang, Y. *Nanodevices based on silicon nanowires*. Recent Patents on Nanotechnology, 3, 1, **2009**.

[9] Guisbiers, G.; and Pereira, S. *Theoretical investigation of size and shape effects on the melting temperature of ZnO nanostructures*. Nanotechnology, 18, 435710, **2007**.

[10] Nawrocki, W. *Electrical and thermal properties of nanowires in quantum regime*. Reviews on Advanced Materials Science, 23, 107, **2010**.

[11] Chen, L.; Niebling, T.; Heimbrodt, W.; Stichtenoth, D.; Ronning, C.; and Klar, P. J. *Dimensional dependence of the dynamics of the Mn $3d^5$ luminescence in (Zn, Mn)S nanowires and nanobelts*. Physical Review B, 76, 115325, **2007**.

[12] Cui, Y.; Zhong, Z.; Wang, D.; Wang, W. U.; and Lieber, C. M. *High performance silicon nanowire field effect transistors*. Nano Letters, 3, 149, **2003**.

[13] Wallentin, J.; Anttu, N.; Asoli, D.; Huffman, M.; Åberg, I.; Magnusson, M. H.; Siefer, G.; Fuss-Kailuweit, P.; Dimroth, F.; Witzigmann, B.; Xu, H. Q.; Samuelson, L.; Deppert, K.; and Borgström, M. T. *InP nanowire array solar cells achieving 13.8% efficiency by exceeding the ray optics limit*. Science, 339, 6123, **2013**.

[14] Samuelson, L. *Self-forming nanoscale devices*. Materials Today, 6, 22, **2003**.

[15] Ohno, H.; Shen, A.; Matsukura, F.; Oiwa, A.; Endo, A.; Katsumoto, S.; and Iye, Y. *(Ga,Mn)As: A new diluted magnetic semiconductor based on GaAs*. Applied Physics Letters, 69, 363, **1996**.

[16] Ohno, H.; Munekata, H.; Penney, T.; Von Molnar, S.; and Chang, L. L. *Magnetotransport properties of p-type (In,Mn)As diluted magnetic III-V semiconductors*. Physical Review Letters, 68, 2664 – 2667, **1992**.

[17] Dietl, T.; Haury, A.; and d'Aubigne, M. *Free Carrier Induced Ferromagnetism in structures of diluted magnetic semiconductors*. Physical Review B, 55, R3347 – R3350, **1997**.

[18] Boeck, J. D.; Oesterholt, R.; Bender, H.; Esch, A. V.; Bruynseraede, C.; Hoof, C. V.; and Borghs, G. *Controlled formation of nanoscale MnAs magnetic clusters in GaAs*. Journal of Magnetism and Magnetic Materials, 156, 148, **1996**.

[19] Wellmann, P.; Garcia, J.; Feng, J. -L.; and Petroff, P. *Formation of nanoscale ferromagnetic MnAs crystallites in low-temperature grown GaAs*. Applied Physics Letters, 71, 2532, **1997**.

[20] Moreno, M.; Jenichen, B.; Kaganer, V.; Braun, W.; Trampert, A.; Däweritz, L.; and Ploog, K. *MnAs nanoclusters embedded in GaAs studied by x-ray diffuse and coherent scattering*. Physical Review B, 67, 235206, **2003**.

[21] Hai, P. N.; Takahashi, K.; Yokoyama, M.; Ohya, S.; and Tanaka, M. *Magnetic properties of MnAs nanoclusters embedded in a GaAs semiconductor matrix*. Journal of Magnetism and Magnetic Materials, 310, 1932, **2007**.

[22] Sadowski, J.; Dluzewski, P.; Kret, S.; Janik, E.; Lusakowska, E.; Kanski, J.; Presz, A.; Terki, F.; Charar, S.; and Tang, D. *GaAs:Mn nanowires grown by molecular beam epitaxy of (Ga,Mn)As at MnAs segregation conditions*. Nano Letters, 7, 2724, **2007**.

[23] Hai, P. N.; Ohya, S.; Tanaka, M.; Barnes, S. E.; and Maekawa, S. *Electromotive force and huge magnetoresistance in magnetic tunnel junctions*. Nature, 458, 489, **2009**.

[24] Martelli, F.; Rubini, S.; Piccin, M.; Bais, G.; Jabeen, F.; De Franceschi, S.; Grillo, V.; Carlino, E.; D'Acapito, F.; Boscherini, F.; Cabrini, S.; Lazzarino, M.; Businaro, L.; Romanato, F.; and Franciosi, A. *Manganese-induced growth of GaAs nanowires*. Nano Letters, 6, 2130, **2006**.

[25] Jeon, H. C.; Kang, T. W.; Kim, T. W.; Yu, Y. -J.; Jhe, W.; and Song, S. A. *Magnetic and optical properties of* $(Ga_{1-x}Mn_x)As$ *diluted magnetic semiconductor quantum wires with above room ferromagnetic transition temperature*. Journal of Applied Physics, 101, 023508, **2007**.

[26] Dluzewski, P.; Sadowski, J.; Kret, S.; Dabrowski, J.; and Sobczak, K. *TEM determination of directions of (Ga,Mn)As nanowires grown by MBE on GaAs(001) substrates*. Journal of Microscopy, 236, 115, **2009**.

[27] Kim, H. S.; Cho, Y. J.; Kong, K. J.; Kim, C. H.; Chung, G. B.; Park, J.; Kim, J. -Y.; Yoon, J.; Jung, M. -H.; Jo, Y.; Kim, B.; and Ahn, J. -P. *Room-temperature ferromagnetic $Ga_{1-x}Mn_xAs$ ($x \leq 0.05$) nanowires: dependence of electronic structures and magnetic properties on Mn content*. Chemistry of Materials, 21, 1137, **2009**.

[28] Rudolph, A.; Soda, M.; Kiessling, M.; Wojtowicz, T.; Schuh, D.; Wegscheider, W.; Zweck, J.; Back, C.; and Reiger, E. *Ferromagnetic GaAs/GaMnAs core-shell nanowires grown by molecular beam epitaxy*. Nano Letters, 9, 3860, **2009**.

[29] Wolff, M.; Görlitz, D.; Nielsch, K.; Messing, M.; and Deppert, K. *Synthesis and magnetic characterization of MnAs nanoparticles via nanoparticle conversion*. Nanotechnology, 22, 055602, **2011**.

[30] Ohno, H. *Properties of ferromagnetic III-V semiconductors*. Journal of Magnetism and Magnetic Materials, 200, 110, **1999**.

[31] Bürger, D.; Zhou, S.; Grenzer, J.; Reuther, H.; Anwand, W.; Gottschalch, V.; Helm, M.; and Schmidt, H. *The influence of annealing on manganese implanted GaAs films*. Nuclear Instruments and Methods in Physics Research B, 267, 1626, **2009**.

[32] Scarpulla, M. A.; Dubon, O. D.; Yu, K. M.; Monteiro, O.; Pillai, M. R.; Aziz, M. J.; and Ridgway, M. C. *Ferromagnetic $Ga_{1-x}Mn_xAs$ produced by ion implantation and pulsed-laser melting*. Applied Physics Letters, 82, 1251, **2003**.

[33] Scarpulla, M. A.; Farshchi, R.; Stone, P. R.; Chopdekar, R. V.; Yu, K. M.; Suzuki, Y.; and Dubon, O. D. *Electrical transport and ferromagnetism in $Ga_{1-x}Mn_xAs$ synthesized by ion implantation and pulsed-laser melting.* Journal of Applied Physics, 103, 073913, **2008**.

[34] Chen, C.; Niu, H.; Hsieh, H.; Cheng, C.; Yan, D.; Chi, C.; Kai, J.; and Wu, S. *Fabrication of ferromagnetic (Ga,Mn)As by ion irradiation.* Journal of Magnetism and Magnetic Materials, 321, 1130, **2009**.

[35] Stichtenoth, D.; Wegener, K.; Gutsche, C.; Regolin, I.; Tegude, F. J.; Prost, W.; Seibt, M.; and Ronning C. *P-type doping of GaAs nanowires*. Applied Physics Letters, 92, 163107, **2008**.

[36] Borschel, C. M. *Ion-Solid Interaction in Semiconductor Nanowires*. Dissertation, Jena University, Germany, **2012**.

[37] Ashcroft, N. M.; Mermin, N. D. *Solid state physics*. Saunders College, Philadelphia, **1976**.

[38] Neamen, D. A. *Semiconductor physics and devices: basic principles*. 4th edition, McGraw-Hill Higher Education, USA, **2012**.

[39] Duan, X. F.; Huang, Y.; Cui, Y.; Wang, J. F.; and Lieber, C. M. *Indium phosphide nanowires as building blocks for nanoscale electronic and optoelectronic devices*. Nature, 409, 66, **2001**.

[40] Li, Y.; Qian, F.; Xiang, J.; and Lieber, C. M. *Nanowire electronic and optoelectronic devices*. Materials Today, 9, 18, **2006**.

[41] Law, M.; Greene, L. E.; Johnson, J. C.; Saykally, R.; and Yang, P. *Nanowire dye-sensitized solar cells*. Nature Materials. 4, 455, **2005**.

[42] Zhou, F.; Seol, J. H.; Moore, A. L.; Shi, L.; Ye, Q. L.; and Scheffler, R. *One-dimensional electron transport and thermopower in an individual InSb nanowire*. Journal Physics: Condensed Matter, 18, 9651, **2006**.

[43] Cui, Y.; Wei, Q.; Park, H. and Lieber, C. M. *Nanowire nanosensors for highly sensitive and selective detection of biological and chemical species*. Science, 293, 1289, **2001**.

[44] Yeh, P. -H.; Li, Z.; and Wang, Z. *Schottky-gated probe-free ZnO nanowire biosensor*. Advanced Materials, 21, 4975, **2009**.

[45] Colombo, C.; Spirkoska, D.; Frimmer, M.; Abstreiter, G. and Fontcuberta i Morral, A. *Ga-assisted catalyst-free growth mechanism of GaAs nanowires by molecular beam epitaxy*. Physical Review B, 77 (15), 155326, **2008**.

[46] Messing, M. *Gold particles for growth of semiconductor nanowires*. Licenciate Thesis, Lund University, Sweden, **2009**.

[47] Jacobsson, D. *Crystal structure determination of III-V nanowires*. Licenciate Thesis, Lund University, Sweden, **2013**.

[48] Mårtensson, T. *Semiconductors nanowire: Epitaxy and applications*. Doctoral Thesis, ISBN 978-91-628-7572-5, **2008**.

[49] P. Nguyen, P.; Ng, H. T.; and Meyyappan, M. *Catalyst metal selection for synthesis of inorganic nanowires*. Advanced Materials, 17, 1773, **2005**.

[50] Xia, Y. N.; Yang, P. D.; Sun, Y. G.; Wu, Y. Y.; Mayers, B.; Gates, B.; Yin, Y. D.; Kim, F.; and Yan, Y. Q. *One-dimensional nanostructures: Synthesis, characterization, and applications*. Advanced Materials 15, 353, **2003**.

[51] Stringfellow, G. B. *Organometallic vapor-phase epitaxy: Theory and practice*. Academic Press, San Diego, 2nd edition, **1999**.

[52] Hochbaum, A. I.; Yang, P. *Semiconductor nanowires for energy conversion*. Chemical Reviews, 110, 527, **2010**.

[53] Ihn, T. *Semiconductor nanostructures.* Oxford University, Oxford, **2010.**

[54] Ghandhi, S. K. *VLSI Fabrication principles*. 2nd Edition, Wiley, New York, **1994**.

[55] Brodie, I.; and Muray, J. J. *The Physics of microfabrication.* Plenum, New York, **1982**.

[56] Matsukura, F.; Ohno, H.; and Dietl, T. *III-V Ferromagnetic semiconductors*. Handbook of magnetic materials. Chapter edited by K.H.J. Buschow, Elsevier Science, **2003**.

[57] Malfait, M. *Magnetic and transport properties of* $Ga_{1-x}Mn_xAs$ *diluted magnetic semiconductors*. Doctoral Thesis, KU Leuven, Belgium, **2005**.

[58] Furdyna, J. K.; and Samarth, N. *Magnetic properties of diluted magnetic semiconductors: A review (invited)*. Journal of Applied Physics, 61, 3526, **1987**.

[59] Szczytko, J.; Mac, W.; Twardowski, A.; Matsukura, F.; and Ohno, H. *Antiferromagnetic p−d exchange in ferromagnetic* $Ga_{1-x}Mn_xAs$ *epilayers*. Physical Review B, 59, 12935 – 12939, **1999**.

[60] Matsukura, F.; Ohno, H; Shen, A.; and Sugawara, Y. *Transport properties and origin of ferromagnetism in (Ga,Mn)As*. Physical Review B, 57, 2037 – 2040, **1998**.

[61] Ohno, H.; and Matsukura, F. *A ferromagnetic III–V semiconductor: (Ga,Mn)As*. Solid State Communications, 117**,** 179 – 186, **2001**.

[62] Van Esch, A.; Van Bockstal, L.; and De Boeck, J. *Interplay between the magnetic and transport properties in the III-V diluted magnetic semiconductor* $Ga_{1-x}Mn_xAs$. Physical Review B, 56, 13103 – 13112, **1997**.

[63] Lebedeva, N., *Spintronic semiconductor devices based on Mn doped GaAs*. Doctoral Thesis, ISBN 978-952-60-5390-5, **2013**.

[64] Blakemore, J. S. *Semiconducting and other major properties of gallium arsenide*. Journal of Applied Physics, 53, 123, **1982**.

[65] http://www.ioffe.ru/SVA/NSM/Semicond/GaAs/basic.html

[66] Ferry, D. K. *Semiconductors*. IOP science, chapter 2, 2 – 53, **2013**.

[67] Ruderman M. A.; and Kittel, C. *Indirect exchange coupling of nuclear magnetic moments by conduction electrons*. Physical Review, 96, 99 – 102, **1954**.

[68] Wang, K. Y.; Campion, R. P.; Edmonds, K. W.; Sawicki, M.; Dietl, T.; Foxon, C. T.; and Gallagher, B. L. *Magnetism in (Ga,Mn)As thin-films with* T_C *up to 173K*. AIP Conference Proceedings, 772, 333 – 334, **2005**.

[69] Madelung, O. (editor), *Semiconductors: Group IV elements and III-V compounds*. Data in Science and Technology: Springer-Verlag, **1991**.

[70] Magnusson, M. H.; Deppert, K.; Malm, J. -O.; Bovin, J. -O.; Samuelson, L. *Size-selected gold nanoparticles by aerosol technology*. Nanostructured Materials, 12, 45 – 48, **1999**.

[71] Lehmann, S.; Jacobsson, D.; Deppert, K.; and Dick, K. A. *High crystal quality wurtzite–zinc blende heterostructures in metal–organic vapor phase epitaxy-grown GaAs nanowires*. Nano Research, 5(7), 470 – 476, **2012**.

[72] Gutsche, C.; Regolin, I.; Blekker, K.; Lysov, A.; Prost, W.; and Tegude, F.J. *Controllable p-type doping of GaAs nanowires during vapor-liquid-solid growth*. Journal of Applied Physics, 105, 024305, **2009**.

[73] Borschel, C.; and Ronning, C. *Ion beam irradiation of nanostructures – A 3D Monte Carlo simulation code*. Nuclear Instruments and Methods in Physics Research B, 269, 19, 2133 – 2138, **2011**.

[74] Kumar, S.; Karmakar, S.; Bramanti, A.; Rinaldi, R.; and Maruccio, G. *Nanofabrication for molecular scale devices*. InTech Books - Nanofabrication, Dr. Yoshitake Masuda (Ed.), ISBN: 978-953-307-912-7, **2011**.

[75] Nilsson, H. A. *Electron transport in nanowire quantum devices*. Doctoral Thesis, ISBN 978-91-628-8125-2, **2010**.

[76] Wallentin, J.; Persson, J. M.; Wagner, J. B.; Samuelson, L.; Deppert, K.; and Borgstrom, M. T. *High-performance single nanowire tunnel diodes*. Nano Letters, 10, 974 – 979, **2010**.

[77] http://www.janis.com/Products/productsoverview/SuperconductingMagnetSystems.aspx

[78] Mott, N. F. *Conduction in glasses containing transition metal ions*. J. Non-Cristal. Solid 1, 1, **1968**.

[79] Abrahams, E.; and Miller, A. *Impurity conduction at low concentrations*, Physical Review, 120, **1960**.

[80] Shklovskii, B. I.; and Efros, A. L. *Electronic properties of doped semiconductors*. Springer-Verlag, Inc. New York, **1984**.

[81] Singh, J. *Physics of semiconductors and their heterostructures*. McGraw-Hill, Inc. New York, **1993**.

[82] Mott, N. F. *Conduction in non-crystalline materials, localized states in a pseudogap and near extremities of conduction and valence bands on crystalline materials, localized states*. Philosophical Magazine, 19, 835, **1969**.

[83] Lee, P. A. *Disordered electronic systems*. Reviews of Modern Physics, 57, 287 – 337, **1985**.

[84] Zabrodskii, A. G. *The Coulomb gap: the view of an experimenter*. Philosophical Magazine, 81, 9, 1131 – 1151, **2001**.

[85] Shahar, D.; and Ovadyahu, Z. *Dimensional crossover in the hopping regime induced by an electric field*. Physical Review Letters, 64, 2293 – 2296, **1990**.

[86] Yu, D.; Wang, C.; Wehrenberg, B. L.; and Guyot-Sionnest, P. *Variable range hopping conduction in semiconductor nanocrystal solids*. Physical Review Letters, 92, 216802, **2004**.

[87] Lee, C. H.; Yi, G. C.; Zuev, Y. M.; and Kim, P. *Thermoelectric power measurements of wide band gap semiconducting nanowires*. Applied Physics Letters, 94, 2, 022106, **2009**.

[88] Ohno, H. *Making nonmagnetic semiconductors ferromagnetic*. Science, 281, 5379, 951 – 956, **1998**.

[89] Osinniy, V.; Dybko, K.; Jedrzejczak, A.; Arciszewska, M.; Dobrowolski, W.; Story, T.; Radchenko, M. V.; Sichkovskiy, V. I.; Lashkarev, G.V.; Olsthoorn, S. M.; and Sadowski, J. *Thermoelectric studies of electronic properties of ferromagnetic GaMnAs layers.* Semiconductor Physics, Quantum Electronics and Optoelectronics, 11, 2, 257 – 265, **2008**.

[90] Mott, N. F.; and Davis, E. A. *Electronic processes in non-crystalline Materials*. Clarendon Press, Oxford, UK, **1979**.

[91] Benoit á la Guillaume, C. *Free magnetic polarons in three, quasi-two, and quasi-one dimensions*. Physica Status Solidi (b), 175, 369 – 380, **1993**.

[92] Devreese J. T. *Polarons*. Encyclopedia of Applied Physics, 14, 383 – 409, **1996**.

[93] Binder K.; and Young, A. P. *Spin glasses: Experimental facts, theoretical concepts, and open questions*. Reviews of Modern Physics, 58, 4, **1986**.

[94] Kaminski, A.; and Das Sarma, S. *Polaron percolation in diluted magnetic semiconductors*. Physical Review Letters, 88, 24, 247202, **2002**.

[95] Yuldashev, Sh. U.; Jeon, H. C.; Im, H. S.; Kang, T. W.; Lee, S. H.; Furdyna, J. K. *Anomalous Hall effect in insulating* $Ga_{1-x}Mn_xAs$. Physical Review B, 70, 193203, **2004**.

[96] Duan, F.; and Guojun J. *Introduction to condensed matter physics*. World Scientific, Singapore, **2005**.

[97] Oseroff, S.; and Keesom, P. H. *Dilute Magnetic Semiconductors*. Academic: New York, 73, **1988**.

[98] Kaminski, A.; Galitski, V. M.; and Das Sarma, S. *Ferromagnetic and random spin ordering in dilute magnetic semiconductors*. Physical Review B, 70, 115216, **2004**.

[99] Omiya, T.; Matsukura, F.; Dietl, T.; Ohno, Y.; Sakon, T.; Motokawa, M.; and Ohno, H. *Magnetotransport properties of (Ga,Mn)As investigated at low temperature and high magnetic field*. Physica E: Low-dimensional system and nanostructures, 7, 976 – 980, **2000**.

[100] Khosla, R. P.; and Fischer, J. R. *Magnetoresistance in Degenerate Cds: Localized Magnetic Moments*. Physical Review B, 2, 10 4084, **1970**.

[101] Watts, S. M.; Wirth, S.; von Molnar, S; Barry, A.; and Coey, J. M. D. *Evidence for two-band magnetotransport in half-metallic chromium dioxide*. Physical Review B, 61, 9621, **2000**.

[102] Ermanis, F.; and Wolfstirn, K. *Hall Effect and Resistivity of Zn-Doped GaAs*. Journal of Applied Physics, 37, 1963, **1966**.

[103] Peters, J. A.; Parashar, N. D.; Rangaraju, N.; and Wessels, B. W. *Magnetotransport properties of InMnSb magnetic semiconductor thin films*. Physical Review B, 82, 205207, **2010**.

[104] Halbo, L.; and Sladek, R. J. *Magnetoresistance of undoped n-type GaAs at low temperature*. Physical Review, 173, 794, **1968**.

[105] Emel'yanenko, O. V.; Lagunova, T. S.; Nasledov, D. N.; Nedeoglo, D. D.; and Timchenko, I. N. *Impurity conduction in n-type GaAs*. Soviet Physics – Semiconductors, 7, 1280, **1973**.

[106] Kahlert, H.; Landwehr, G; Schlachetzki, A.; and Salow, H. *Impurity conduction and magnetoresistance in lightly doped n-type GaAs*. Zeitschrift für Physik B, 276, 361 – 365, **1976**.

[107] Lemoine D.; Pelletier, C.; Rolland, S.; and Ganger, G. *Hopping conduction in epitaxial n-GaAs layers*. Physics Letters A, 56, 493 – 495, **1976**.

[108] Sites, J. R.; and Nedoluha, A. K. *GaAs impurity band transport in large magnetic field*. Physical Review, 24, 4309 – 4316, **1981**.

[109] Mikoshiba, N. *Strong-field magnetoresistance of impurity conduction in n-type germanium*. Physical Review, 127, 1962 – 1969, **1962**.

[110] Shklovskii, B. I. *Hopping conductivity of semiconductors in strong magnetic field*. Soviet Physics – JETP, 34, 1084, **1972**.

[111] Shklovskii, B. I. *Theory of exponential magnetoresistance in semiconductors*. Soviet Physics – Semiconductors, 8, 268, **1973**.

[112] Shklovskii, B. I. *Anisotropy of hopping conduction*. Soviet Physics – Semiconductors, 11, 1253, **1977**.

[113] Shklovskii, B. I.; and Van Lien, N. *Hopping magnetoresistance of n-type germanium*. Soviet Physics – Semiconductors, 12, 796, **1978**.

[114] Landau, L. D.; and Lifshitz, E. M. *Quantum Mechanics*. Pergamon, London, 2nd edition, **1965**.

[115] Shklovskii, B. I. *Positive magnetoresistance in the variable range hopping conduction regime*. Soviet Physics – Semiconductors, 17, 1311, **1983**.

[116] Shklovskii, B. I.; and Spivak, B. Z. *Hopping Transport in Solids,* edited by Pollak, M.; and Shklovskii, B. I. Elsevier, p. 271, **1991**.

Paper I

NANO LETTERS

LETTER

pubs.acs.org/NanoLett

A New Route toward Semiconductor Nanospintronics: Highly Mn-Doped GaAs Nanowires Realized by Ion-Implantation under Dynamic Annealing Conditions

Christian Borschel,[*,†] Maria E. Messing,[‡] Magnus T. Borgström,[‡] Waldomiro Paschoal, Jr.,[‡] Jesper Wallentin,[‡] Sandeep Kumar,[‡] Kilian Mergenthaler,[‡] Knut Deppert,[‡] Carlo M. Canali,[§] Håkan Pettersson,[‡,∥] Lars Samuelson,[‡] and Carsten Ronning[†]

[†]Institute for Solid State Physics, Jena University, Max-Wien-Platz 1, 07743 Jena, Germany

[‡]Solid State Physics/The Nanometer Structure Consortium, Lund University, Box 118, SE-221 00 Lund, Sweden

[§]Division of Physics, School of Computer Science, Physics and Mathematics, Linnæus University, 39233 Kalmar-Sweden

[∥]Department of Mathematics, Physics, and Electrical Engineering, Halmstad University, Box 823, SE-301 18, Halmstad, Sweden

Supporting Information

ABSTRACT: We report on highly Mn-doped GaAs nanowires (NWs) of high crystalline quality fabricated by ion beam implantation, a technique that allows doping concentrations beyond the equilibrium solubility limit. We studied two approaches for the preparation of Mn-doped GaAs NWs: First, ion implantation at room temperature with subsequent annealing resulted in polycrystalline NWs and phase segregation of MnAs and GaAs. The second approach was ion implantation at elevated temperatures. In this case, the single-crystallinity of the GaAs NWs was maintained, and crystalline, highly Mn-doped GaAs NWs were obtained. The electrical resistance of such NWs dropped with increasing temperature (activation energy about 70 meV). Corresponding magnetoresistance measurements showed a decrease at low temperatures, indicating paramagnetism. Our findings suggest possibilities for future applications where dense arrays of GaMnAs nanowires may be used as a new kind of magnetic material system.

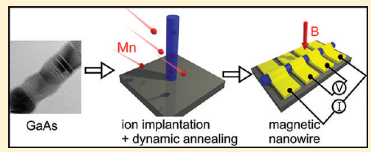

KEYWORDS: Nanowires, GaAs, doping, DMS, ion implantation, dynamic annealing

Ferromagnetic ordering is observed in highly Mn-doped GaAs, in bulk or as thin films, where Mn provides the uncompensated spins as well as p-doping, allowing hole-mediated ferromagnetism. Transition-metal solubility limits in III−V semiconductors are low, but the necessary Mn fractions for ferromagnetic dilute magnetic semiconductors (DMS) can be achieved, for example, by nonequilibrium growth using low temperature MBE at 250 °C.[1] Higher growth temperatures or subsequent annealing typically lead to higher doping levels in the semiconductor, but also segregation into MnAs clusters.[2,3]

Self-assembled semiconductor nanowires (NWs) have proven to be of interest as versatile building blocks of high functionality for various devices, such as field-effect transistors,[4] sensors,[5] and solar cells.[6] Moreover, the small footprint of semiconductor NWs facilitates direct growth on silicon wafers. Dilute magnetic semiconductor NWs would therefore offer a seamless integration of future spintronic devices with mainstream silicon technology, which is one of the main goals of "More than Moore".

Self-organized growth of epitaxial GaAs NWs of high-crystalline quality is possible via metal organic vapor phase epitaxy (MOVPE).[7−9] The relatively high growth temperatures for nanowire growth, typically 400−500 °C, inhibit the homogeneous incorporation of high Mn-concentrations during growth due to the low solubility limit.

Over the years, several attempts have been made to fabricate $Ga_{1-x}Mn_xAs$ NWs. Already in 2002, Sadowski et al. reported the successful growth of InGaMnAs NWs by migration enhanced epitaxy.[10] Later, they established growth of $Ga_{1-x}Mn_xAs$ NWs using MnAs nanoclusters as growth seeds.[11] The obtained NWs contained up to 7% of Mn and were strongly tapered with irregular side facets. The high Mn content led to a branching of the NWs.[12] Martelli et al. performed doping of GaAs NWs using Mn-assisted growth.[13] Recently, Kim et al. synthesized gold-seeded $Ga_{1-x}Mn_xAs$ NWs using a vapor transport method with low Mn content (<5%) exhibiting room-temperature ferromagnetism;[14] however, the magnetic properties are unclear due to lack of any mechanism which could explain the high T_C values.[15] An additional complication is that the Mn may not incorporate homogeneously in the NWs. In fact, it might be that the Mn accumulates in the form of a shell, as indicated by tomographic atom probe measurements for Ge NWs doped during VLS growth.[16] Jeon et al. reported on room-temperature ferromagnetism of GaMnAs NWs with a Mn content of 20%,[17] which is a metallic alloy rather than diluted Mn in a GaAs matrix.

Received: June 27, 2011
Revised: August 12, 2011
Published: August 17, 2011

ACS Publications © 2011 American Chemical Society

dx.doi.org/10.1021/nl2021653 | *Nano Lett.* 2011, 11, 3935–3940

Rudolph et al. exploited the possibility to change growth mode from axial to radial nanowire growth and fabricated ferromagnetic GaAs/GaMnAs core/shell NWs.[15] However, the growth of the GaMnAs shell leads to a morphological change from the perfect hexagonal GaAs core NWs toward roughened core/shell GaAs/GaMnAs NWs. A completely different approach was performed by Wolff et al.[18] who decorated GaAs NWs with Mn nanoparticles, which were then transformed into MnAs nanoparticles by thermal annealing in hydrogen and arsine.

Most of the reported attempts suffer from segregation of the MnAs phase during growth leading to nonideal nanowire morphologies. This can easily be exemplified by the morphological change from the perfect hexagonal GaAs core NWs toward totally roughened core/shell NWs after growth of the $Ga_{1-x}Mn_xAs$ shells around them.[15] Furthermore, the detection of segregated MnAs nanoclusters in GaAs with X-ray diffraction (XRD) or high-resolution transmission electron microscopy (HR-TEM) is reported to be rather challenging[19] and these clusters can easily be mistaken for a DMS. In conclusion, in situ Mn-doping of GaAs NWs turns out to be rather difficult to achieve by established growth methods. This observation is well in agreement with the phase diagram determined by Ohno for $Ga_{1-x}Mn_xAs$ layer growth via MBE:[20] For x in the order of 0.5−6%, MnAs forms above about 300 °C.

Postgrowth ion beam implantation is a nonequilibrium doping method that allows concentrations beyond solubility limits and is independent from the growth method of the crystal. It is a standard method for doping of large scale wafers in industry, but it has also been successfully applied for doping of semiconductor NWs.[21] The successful p-doping of GaAs NWs via ion beam implantation of Zn and subsequent annealing at 800 °C under tertiarybutylarsine atmosphere has been reported.[22] Ion beam implantation introduces defects in the target, making postimplantation annealing a necessity. For Mn-implanted GaAs thin films, standard thermal annealing (650 °C) has been reported to lead to MnAs cluster formation.[23] Only pulsed laser melting[24,25] and ion beam-induced epitaxial crystallization annealing[26] have shown promising results regarding the incorporation of Mn in GaAs to create DMS systems.

The annealing methods from bulk cannot directly be transferred to nanosized objects, because, due to their large surface-to-volume ratio, the equilibrium phases strongly differ from those for bulk material. For example, NWs exhibit lower melting points compared to their bulk counterparts.

In this Letter, we compare two approaches for preparation of Mn-doped GaAs NWs by (a) ion implantation at room temperature with subsequent annealing and (b) ion implantation at elevated temperatures making use of in situ dynamic annealing. Furthermore, we report on magnetotransport measurements that were done in order to study the magnetic properties of the implanted $Ga_{1-x}Mn_xAs$ NWs.

Single crystalline, epitaxial GaAs NWs were grown via MOVPE using monodisperse Au particles as catalyst. Details have been published elsewhere.[27] In order to optimize the implantation angle, the NWs were grown on GaAs(001) substrates leading to an inclined growth direction of 35° toward the substrate.[28] NWs were implanted with Mn ions using a general purpose implanter (High Voltage Engineering Europa). Implantation energies of typically 40−60 keV were selected. Results from computer simulations of the ion beam implantation show that these energies lead to a reasonably homogeneous concentration of Mn in the GaAs NWs. Frequently, these simulations

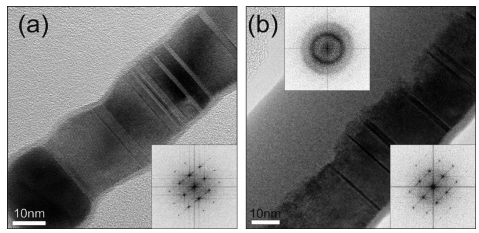

Figure 1. (a) HR-TEM image of an as-grown GaAs nanowire, with the FFT shown in the inset. (b) TEM micrograph of an implanted, nonannealed nanowire (with approx 2.5% Mn), that is partly amorphized and partly crystalline. The two insets show FFTs of the amorphous and crystalline parts, respectively.

are carried out with the widely used SRIM program.[29] However, SRIM assumes flat sample geometry and cannot accurately describe the distribution of implanted ions in NWs. Therefore, we used the new in-house developed code *iradina*,[30] which correctly takes into account the nanowire geometry.

NWs were implanted with Mn doses of 2×10^{15} to 1×10^{16} ions/cm^2 resulting in total Mn concentrations from 0.5 to 2.9% (corresponding to a stoichiometry of $Ga_{1-x}Mn_xAs$ with x from $x = 0.01$ to $x = 0.058$) as calculated with the *iradina* code. Detailed simulation results comparing SRIM and iradina for the given situation are shown in the Supporting Information Figure 1. The first set of samples (a) was implanted at room temperature and subsequently annealed for 30 min either under vacuum at temperatures up to 500 °C, or under AsH_3 atmosphere (molar fraction of 2.20×10^{-3}) from 350 to 650 °C. The second set of samples (b) was implanted at elevated temperatures ranging from 100 to 350 °C. The NWs were characterized by transmission electron microscopy (TEM) using a Jeol 3010 and a Jeol 3000F microscope. The Mn concentration was monitored via X-ray energy dispersive spectroscopy (XEDS).

For magnetotransport measurements, NWs were mechanically transferred onto a silicon substrate covered by a 210 nm thick silicon dioxide layer on which reference markers and macroscopic metal pads were predefined. Prior to transferring of the NWs, trenches were etched in the SiO_2 layer to align the wires for magnetotransport studies. Electron beam lithography was used to define contacts connecting individual NWs to the macroscopic contact pads. The samples were treated in HCl/H_2O solution for 15 s followed by a 2 min surface passivation in a heated (40 °C) NH_4S_x/H_2O solution. To investigate the influence of the contact resistance, 4 Pd(10 nm)/Zn(10 nm)/Pd-(35 nm) contacts were evaporated on each NW after passivation.[31] The sample processing was finalized by a lift-off process. The magnetotransport measurements were performed in a Janis VariTemp superconducting cryomagnet system (Model 8T-SVM).

Figure 1a shows an HR-TEM micrograph of a typical nonimplanted, as-grown, NW for comparison. The single-crystalline NWs of zinc blende (ZB) structure were grown in the ⟨111⟩ direction and exhibit twin planes perpendicular to the growth direction, as commonly observed for III−V semiconductor NWs.[32] Resulting from the implantation parameters at room temperature, the NWs were mostly amorphized, which is illustrated in Figure 1b. Depending on the Mn dose, the ion energy, and the exact diameter of the NWs, some parts that face away

dx.doi.org/10.1021/nl2021653 |*Nano Lett.* 2011, 11, 3935–3940

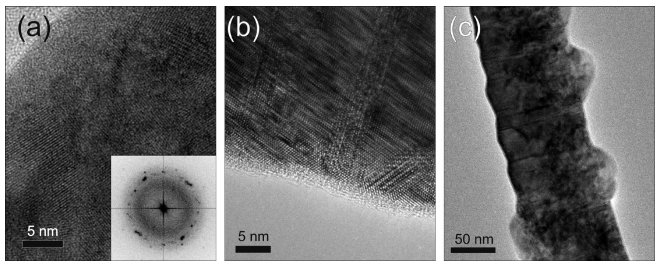

Figure 2. TEM micrographs of implanted and annealed NWs. (a) After annealing in vacuum at 400 °C, the FFT in the inset shows that the nanowire is not single crystalline. (b,c) After annealing in As atmosphere at 550 °C. (b) Nanowire is polycrystalline. (c) Bumps appear on nanowire, consisting of GaAs.

from the ion beam however remained crystalline as illustrated by the fast Fourier transform (FFT) diffraction pattern (inset in Figure 1b).

The NWs recrystallized under annealing in vacuum up to 400 °C, however not to single crystals. A typical polycrystalline nanowire is described by the HR-TEM image and its FFT pattern in Figure 2a. After annealing in vacuum at 500 °C or higher temperatures, we observed that the NWs disappeared, which we interpret as a temperature-induced decomposition of the GaAs NWs, mainly due to the high equilibrium As vapor pressure over GaAs. Therefore, annealing in AsH_3 atmosphere, as previously used to recrystallize Zn-implanted GaAs NWs,[22] was attempted. Within the investigated parameter space, the present Mn-doped NWs survived the treatment but although some recrystallization occurred, they did not become single crystalline (see Figure 2b). Additionally, they featured "bumps" on the sides, as illustrated in Figure 2c. Analysis of the FFT patterns and XEDS shows that these bumps consist of crystalline GaAs without measurable Mn content; the postimplantation annealing with arsine background pressure seems to initiate unwanted regrowth of crystalline GaAs on the amorphized NW.

At this point, we can conclude that room-temperature implantation and subsequent annealing is not suitable to create single crystalline GaAs NWs with a high Mn concentration under the parameter conditions investigated, neither in vacuum, nor in an arsine atmosphere.

During ion beam implantation, so-called dynamic annealing can occur.[33] Each ion induces a collision cascade in the material, producing a large number of point defects (at the order of 10^3 for the parameters used in this study). Additionally, a high amount of energy is deposited by the incident ion as lattice vibrations in the cascade region. Within this so-called "thermal spike", immediate annihilation of defects can occur. When collision cascades from subsequent ions overlap, defects that were created in the earlier cascade can be annihilated by the following ones. If this dynamic annealing is weak, the damage created by subsequent collision cascades is accumulated and ultimately amorphization of the material will occur, if a large fluence of ions is implanted, as observed in this study. Actually, dynamic annealing is enhanced in NWs compared to bulk[34,35] due to the confined geometry resulting into a slower dissipation of the impact energy. However, this annealing effect is not strong enough at room-temperature implantation of Mn into GaAs NWs, and is thus not able to prevent amorphization: the NWs became amorphous when implanted with x = 1% of Mn. Thus, the crystal orientation

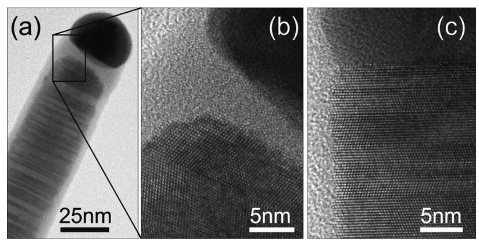

Figure 3. (a) GaAs nanowire implanted with x = 1% Mn at 100 °C. (b) HR image of the same wire showing the amorphous gap between crystalline nanowire core and Au tip. (c) GaAs nanowire implanted with x = 1% Mn at 200 °C.

was lost in the amorphous regions, and subsequent annealing lead to polycrystalline recrystallization, as was described above.

Dynamic annealing can further be enhanced by heating the target during ion implantation[33] due to increased phonon−phonon scattering resulting also into a slower dissipation of the impact energy. In order to make use of this enhanced dynamic annealing, samples were implanted at elevated temperatures. A maximum of 400 °C was used, because decomposition of the GaAs NWs was observed in vacuum at higher temperatures.

Figure 3a,b shows TEM micrographs of a nanowire implanted with Mn at a temperature of 100 °C. A large part of the nanowire remained crystalline during implantation, and the crystalline structure appears similar to the nonimplanted nanowire (Figure 1a). This is in contrast to room-temperature implantation at which the NWs were mostly amorphized. However, an amorphous "neck" close to the catalyst particle appeared after implantation at 100 °C, as illustrated in Figure 3b. This latter observation can be attributed to different efficiency of the dynamic annealing in the proximity of the catalyst particle. For most part of the nanowire, the energy within the thermal spike is sufficient to cause in situ removal of most defects, the crystal orientation is never lost and the material remains single-crystalline in ZB phase and oriented in the (111)B direction. However, when an ion hits the nanowire close to the Au particle, the energy of the thermal spike dissipates much faster, because the thermal conductivity of Au is about 5−6 times larger than of GaAs. Thus, less time is available for annihilation of defects, and amorphization of the material occurs in this area. Such a partial amorphization

dx.doi.org/10.1021/nl2021653 |*Nano Lett.* 2011, 11, 3935–3940

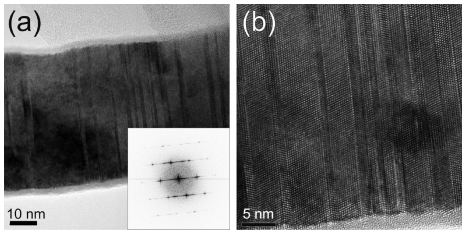

Figure 4. (a) HR-TEM micrograph of GaAs nanowire implanted with x = 5% Mn at 250 °C and FFT of the complete image as inset demonstrating excellent crystalline quality of the Mn-implanted wires. (b) HR-TEM micrograph with higher magnification.

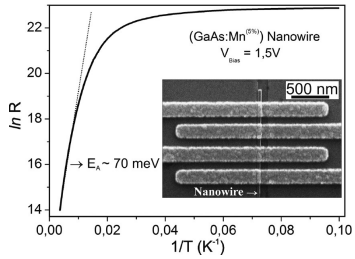

Figure 5. Plot of resistance versus reciprocal temperature with indicated activation energy. The inset shows an SEM micrograph of a nanowire supplied with contacts for 4-point measurements.

could be avoided by further increasing the implantation temperature to above 100 °C. Then, the dynamic annealing was sufficiently enhanced to maintain crystallinity of the complete nanowire, as illustrated for a nanowire implanted at 200 °C in Figure 3c. It should be noted that apart from dynamic annealing caused by the ion beam, normal "thermal healing" may also occur at the higher temperatures in between the ion impacts. However, it is not possible to separate the contributions from ion beam and temperature in the annealing.

From thin film growth of $Ga_{1-x}Mn_xAs$ it is known that phase separation of MnAs occurs above 250−300 °C depending on the Mn concentration.[20] However, due to their small size this limit may be lower for NWs. Therefore, we also examined implantation with high doses of Mn at 250 °C; the results are illustrated in Figure 4a, showing an HR-TEM image of a nanowire implanted with 10^{16} ions/cm^2, corresponding to a total Mn concentration of 2.9% (x = 0.058). Even at these high concentrations, the NWs were observed to remain single-crystalline and no secondary phases were observed. XEDS measurements were performed on several areas on these NWs (Supporting Information Figure 2). They confirmed a Mn concentration of about 2−3%, showing that Mn has not diffused out during implantation at elevated temperatures.

It should be noted at this point, that computer simulations of the ion beam implantation require that the correct nanowire geometry is taken into account. Simulations using SRIM[29] overestimate the implanted concentration of Mn in the NWs by about a factor of 1.7, while simulations using the *iradina* code[30] predict the Mn concentration more accurately to about 2.9%. The reason is that SRIM can only simulate flat targets and therefore cannot take into account ions leaving the nanowire from the sides.

A recovery stage for the electronic properties of GaAs around 250 °C has been reported by Thommen for high-energy electron-beam irradiated GaAs and subsequent annealing.[36] Thus, it seems useful to use at least 250 °C during implantation, although single-crystallinity was already observed at 150 °C. We further increased the implantation temperature to 350 °C and still obtained single crystalline NWs; however, the optimum temperature has to be balanced, since, as mentioned in the introduction, at higher temperatures the precipitation of MnAs nanoclusters becomes more likely.[37] We did not observe MnAs precipitates in the implanted NWs up to 350 °C, but nanometric inclusions of this phase are not easily detectable[19] and cannot be excluded.

Considering the upper and lower limitations, 250 °C was identified as the suitable temperature for creating GaMnAs nanowire with high Mn content via ion beam implantation. This is consistent with the temperature at which Ohno et al. have grown LT-MBE magnetic GaMnAs thin films.[1] Furthermore, 250 °C is also the same temperature Chen et al. used for ion-beam annealing of Mn implanted GaAs thin films.[26]

Transport measurements were carried out between 1.6 and 300 K. To investigate possible influence of contact resistance, 2-point and 4-point measurements were compared down to about 70 K where 4-point measurements became difficult to carry out due to a very high resistance. From these measurements, we conclude that the contact resistance is negligible compared to the NW resistance. The IV-characteristics are in general fairly linear down to about 100 K (Supporting Information Figure 3). At lower temperatures, a symmetrical nonlinear behavior becomes increasingly dominant. Figure 5 displays the resistance of a typical implanted NW versus reciprocal temperature from which we deduce an activation energy of about 70 meV. We have investigated several NWs that all show the same behavior. A similar behavior has previously been reported for planar GaMnAs films and attributed to thermal emission of holes from a Mn impurity band to the valence band.[38] The activation energy is smaller than the typical 100−110 meV observed for weakly doped GaAs:Mn, where the emission originates from isolated Mn impurities.[39] Interestingly, the room-temperature resistance is in the MΩ regime, which is unexpectedly high, considering the nominal x = 5.8% Mn incorporation. A plausible explanation for the apparent low hole concentration ($\sim 10^{17}$ cm^{-3} assuming a reduced mobility of 60 cm^2/(V s)[38] and 40 nm wire diameter) is a Fermi-level pinning at the GaAs surface, which effectively creates a radially depleted semiconductor wire. Also, most likely compensation occurs due to incorporation of interstitial Mn and substitutional As_{Ga} antisites, both acting as double donors. The resulting hole concentration is too low to create the necessary effective ferromagnetic coupling between Mn spins, which results in a paramagnetic state rather than in ferromagnetic ordering. The absence of the onset of any ferromagnetic order in our sample is also evident from the lack of any singularity in the derivative of the resistance as a function of temperature in the range of temperatures (40−190 K), which is expected to occur at the critical temperature.[40] Further understanding of the magnetic state of our implanted wires is obtained from magnetoresistance (MR) studies. In Figure 6, we plot the MR as a function of an external magnetic field applied in the direction parallel and perpendicular to the wire. The data readily shows a negative MR signal up to about 50 K. No evident trace of

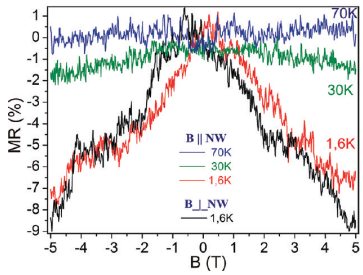

Figure 6. Plot of magnetoresistance versus temperature for parallel (∥) and perpendicular (⊥) orientation of magnetic field relative to nanowire (only one sweep direction is shown).

hysteresis effects was found in our measurements and additionally, the MR does not seem to saturate (up to 5 T). There is also no clear indication of any anisotropic MR changes at small magnetic fields that typically occur in ferromagnetic DMS due to reorientation of the magnetization relative to the current direction. While these MR results support the conclusion that our samples are not ferromagnetic, they are also a strong indication of a paramagnetic state of the system due to the presence of Mn impurities. Indeed, nonimplanted NWs display dramatically different electrical properties with very high resistance (∼200 GΩ) already at room temperature, which makes magnetotransport measurements virtually impossible. Negative MR traces are normally attributed to spin-disorder scattering in metallic samples[20] and to suppression of Anderson localization of holes in insulating or semiconducting samples.[41] Possibly, in the regime of low conductance of our sample, both mechanisms are contributing to some extent in reducing the resistance. The observed MR effect may reflect a decrease in resistance as a result of a Zeeman shift of the Fermi energy toward the Anderson mobility edge by the applied magnetic field, which furthermore reduces spin-disorder scattering by successively aligning the randomly oriented individual Mn spins along its direction. The Zeeman energy for a spin 5/2 is of the order of 20 K at 5 T. If we assume that the magnetization of the sample at a given temperature and magnetic field is proportional to the Brillouin function, the magnetization and consequently the MR should reach saturation at fields on the order of 8 T when the temperature is 1.6 K. On the other hand, as shown in Figure 6, at temperatures above 70 K and at a magnetic field of 5 T, the thermal energy totally randomizes the spin orientation which consequently quenches the MR.

The MR curves further indicate that the Mn is mainly diluted in the GaAs host and not incorporated in the form of ferromagnetic MnAs clusters; Michel et al. have theoretically studied the influence of ferromagnetic MnAs clusters in a paramagnetic GaMnAs host matrix on the MR behavior.[42] They find that a high density of MnAs clusters leads to a strong negative MR below 30 K and a very strong positive MR of several hundred percent between 30 and 100 K. The Mn-doped nanowires only show a weak negative MR below 70 K and no MR at higher temperatures, indicating that there are either no MnAs clusters or at least a very low density of them.

In conclusion, we have realized high-crystalline quality Mn-doped GaAs NWs via ion beam implantation, which allows incorporation of dopants into the target material far beyond the solubility limit. In order to minimize ion beam-induced defects different annealing routes were investigated. Postannealing was not successful for NWs, because the NWs either decomposed or became polycrystalline within the investigated parameter space. However, heating the sample to higher temperatures during implantation (250 °C) enabled increased dynamic annealing in addition to thermal healing, resulting in single-crystalline $Ga_{1-x}Mn_xAs$ NWs with high Mn content.

We also report on magnetotransport measurements on the Mn-implanted NWs, where a strong-temperature dependence of the resistance was observed in addition to a clear negative MR at low temperatures. These results indicate dilute Mn incorporation and, in combination with the observed high resistance of the NWs, support the hypothesis that the implanted NWs are paramagnetic due to a strong reduction in free hole concentration that stems from surface pinning effects and, possibly, from Mn interstitials and As_{Ga} antisites.

This study provides the groundwork to pursue further ion-implantation experiments, for example, in thicker NWs, and to develop novel technology for tuning the hole concentration in the NWs to facilitate an electrically controlled hole concentration and thus ferromagnetism. We believe that the work presented here demonstrates a promising route for future fabrication of complex integrated DMS nanostructures, where arrays of Mn-doped NWs may be functioning as a novel kind of material system for science as well as for applications.

■ ASSOCIATED CONTENT

Supporting Information. Additional information and figures. This material is available free of charge via the Internet at http://pubs.acs.org.

■ AUTHOR INFORMATION

Corresponding Author
*E-mail: christian.borschel@uni-jena.de.

■ ACKNOWLEDGMENT

We acknowledge support by the Swedish Research Council under Grant Number: 621-2010-3761.

■ REFERENCES

(1) Ohno, H.; Shen, A.; Matsukura, F.; Oiwa, A.; Endo, A.; Katsumoto, S.; Iye, Y. *Appl. Phys. Lett.* **1996**, *69*, 363.
(2) De Boeck, J.; Oesterholt, R.; Bender, H.; Van Esch, A.; Bruynseraede, C.; Van Hoof, C.; Borghs, G. *J. Magn. Magn. Mater.* **1996**, *156*, 148.
(3) Wellmann, P. J.; Garcia, J. M.; Feng, J.-L.; Petroff, P. M. *Appl. Phys. Lett.* **1997**, *71*, 2532.
(4) Cui, Y.; Zhong, Z.; Wang, D.; Wang, W. U.; Lieber, C. M. *Nano Lett.* **2003**, *3*, 149.
(5) Yeh, P.-H.; Li, Z.; Wang, Z. L. *Adv. Mater.* **2009**, *21*, 4975.
(6) Hochbaum, A. I.; Yang, P. *Chem. Rev.* **2010**, *110*, 527.
(7) Borgström, M.; Deppert, K.; Samuelson, L.; Seifert, W. *J. Cryst. Growth* **2004**, *260*, 18.
(8) Wagner, R. S.; Ellis, W. C. *Appl. Phys. Lett.* **1964**, *4*, 89.
(9) Wacaser, B. A.; Dick, K. A.; Johansson, J.; Borgström, M. T.; Deppert, K.; Samuelson, L. *Adv. Mater.* **2009**, *21*, 153–165.
(10) Sadowski, J.; Deppert, K.; Kanski, V.; Ohlsson, J.; Persson, A.; Samuelson, L. *Proceedings of the 7th International Conference on Nanometer-scale Science and Technology*, June 24−28, Malmö, Sweden, 2002.

(11) Sadowski, J.; Dłużewski, P.; Kret, S.; Janik, E.; Łusakowska, E.; Kanski, J.; Presz, A.; Terki, F.; Charar, S.; Tang, D. *Nano Lett.* **2007**, *7*, 2724.
(12) Dluzewski, P.; Sadowski, J.; Kret, S.; Dabrowski, J.; Sobczak, K. *J. Microsc.* **2009**, *236*, 115.
(13) Martelli, F.; Rubini, S.; Piccin, M.; Bais, G.; Jabeen, F.; Franceschi, S. D.; Grillo, V.; Carlino, E.; D'Acapito, F.; Boscherini, F.; Cabrini, S.; Lazzarino, M.; Businaro, L.; Romanato, F.; Franciosi, A. *Nano Lett.* **2006**, *6*, 2130.
(14) Kim, H. S.; Cho, Y. J.; Kong, K. J.; Kim, C. H.; Chung, G. B.; Park, J. *Chem. Mater.* **2009**, *21*, 1137.
(15) Rudolph, A.; Soda, M.; Kiessling, M.; Wojtowicz, T.; Schuh, D.; Wegscheider, W.; Zweck, J.; Back, C.; Reiger, E. *Nano Lett.* **2009**, *9*, 3860.
(16) Perea, D. E.; Hemesath, E. R.; Schwalbach, E. J.; Lensch-Falk, J. L.; Voorhees, P. W.; Lauhon, L. J. *Nat. Nanotechnol.* **2009**, *4*, 315.
(17) Jeon, H. C.; Kang, T. W.; Kim, T. W.; Yu, Y.-J.; Jhe, W.; Song, S. A. *J. Appl. Phys.* **2007**, *101*, 023508.
(18) Wolff, M. F. H.; Görlitz, D.; Nielsch, K.; Messing, M. E.; Deppert, K. *Nanotechnology* **2011**, *22*, 055602.
(19) Seo, S. S. A.; Noh, T. W.; Kim, Y.-W.; Lim, J. D.; Park, Y. D.; Kim, Y. S.; Khim, Z. G.; Jeon, H. C.; Kang, T. W.; Pearton, S. J. *J. Appl. Phys.* **2004**, *95*, 8172.
(20) Ohno, H. *J. Magn. Magn. Mater.* **1999**, *200*, 110–129.
(21) Ronning, C.; Borschel, C.; Geburt, S.; Niepelt, R. *Mater. Sci. Eng., R* **2010**, *70*, 30.
(22) Stichtenoth, D.; Wegener, K.; Gutsche, C.; Regolin, I.; Tegude, F. J.; Prost, W.; Seibt, M.; Ronning, C. *Appl. Phys. Lett.* **2008**, *92*, 163107.
(23) Bürger, D.; Zhou, S.; Grenzer, J.; Reuther, H.; Anwand, W.; Gottschalch, V.; Helm, M.; Schmidt, H. *Nucl. Instrum. Methods Phys. Res., Sect. B* **2009**, *267*, 1626.
(24) Scarpulla, M. A.; Dubon, O. D.; Yu, K. M.; Monteiro, O.; Pillai, M. R.; Aziz, M. J.; Ridgway, M. C. *Appl. Phys. Lett.* **2003**, *82*, 1251.
(25) Scarpulla, M. A.; Farshchi, R.; Stone, P. R.; Chopdekar, R. V.; Yu, K. M.; Suzuki, Y.; Dubon, O. D. *J. Appl. Phys.* **2008**, *103*, 073913.
(26) Chen, C. H.; Niu, H.; Hsieh, H. H.; Cheng, C. Y.; Yan, D. C.; Chi, C. C.; Kai, J. J.; Wu, S. C. *J. Magn. Magn. Mater.* **2009**, *321*, 1130.
(27) Mikkelsen, A.; Sköld, N.; Ouattara, L.; Borgström, M.; Andersen, J. N.; Samuelson, L.; Seifert, W.; Lundgren, E. *Nat. Mater.* **2004**, *3*, 519–523.
(28) Hiruma, K.; Yazawa, M.; Katsuyama, T.; Ogawa, K.; Haraguchi, K.; Koguchi, M.; Kakibayashi, H. *J. Appl. Phys.* **1995**, *77*, 447.
(29) Ziegler, J. F.; Biersack, J. P.; Littmark, U. *The stopping and ranges of ions in solids*; Pergamon Press: New York, 1985.
(30) Borschel, C.; Ronning, C. *Nucl. Instrum. Methods Phys. Res., Sect. B* **2011**, *269*, 2133.
(31) Wallentin, J.; Persson, J. M.; Wagner, J. B.; Samuelson, L.; Deppert, K.; Borgstrom, M. T. *Nano Lett.* **2010**, *10*, 974–979.
(32) Yazawa, M.; Koguchi, M.; Hiruma, K. *Appl. Phys. Lett.* **1991**, *58*, 1080.
(33) Williams, J. S. *Mate. Sci. Eng.* **1998**, *253*, 8.
(34) Dhara, S.; Datta, A.; Wu, C. T.; Lan, Z. H.; Chen, K. H.; Wang, Y. L.; Chen, L. C.; Hsu, C. W.; Lin, H. M.; Chen, C. C. *Appl. Phys. Lett.* **2003**, *82*, 451.
(35) Colli, A.; Fasoli, A.; Ronning, C.; Pisana, S.; Piscanec, S.; Ferrari, A. C. *Nano Lett.* **2008**, *8*, 2188.
(36) Thommen, K. *Radiat. Eff.* **1970**, *2*, 201.
(37) Ohno, H. *Science* **1998**, *281*, 951.
(38) Slupinski, T.; Caban, J.; Moskalik, K. *Acta Phys. Pol., A* **2007**, *112*, 325–330.
(39) Ilegems, M.; Dingle, R.; Rupp, L. W., Jr. *J. Appl. Phys.* **1975**, *46*, 3059.
(40) Novák, V.; Olejník, K.; Wunderlich, J.; Cukr, M.; Výborný, K.; Rushforth, A. W.; Edmonds, K. W.; Campion, R. P.; Gallagher, B. L.; Sinova, J.; Jungwirth, T. *Phys. Rev. Lett.* **2008**, *101*, 077201.
(41) Iye, Y.; Oiwa, A.; Endo, A.; Katsumoto, S.; Matsukura, F.; Shen, A.; Ohno, H.; Munekata, H. *Mater. Sci. Eng., B* **1999**, *63*, 88.
(42) Michel, C.; Elm, M. T.; Goldlücke, B.; Baranovskii, S. D.; Thomas, P.; Heimbrodt, W.; Klar, P. J. *Appl. Phys. Lett.* **2008**, *92*, 223119.

Paper II

NANO LETTERS

Letter

pubs.acs.org/NanoLett

Hopping Conduction in Mn Ion-Implanted GaAs Nanowires

Waldomiro Paschoal, Jr.,[†,‡,⊥] Sandeep Kumar,[†,⊥] Christian Borschel,[§] Phillip Wu,[†] Carlo M. Canali,[∥] Carsten Ronning,[§] Lars Samuelson,[†] and Håkan Pettersson*[,†,‡]

[†]Solid State Physics/The Nanometer Structure Consortium, Lund University, Box 118, SE-221 00 Lund, Sweden

[‡]Dept. of Mathematics, Physics and Electrical Engineering, Halmstad University, Box 823, SE-301 18, Halmstad, Sweden

[§]Institute for Solid State Physics, Jena University, Max-Wien-Platz 1, 07743 Jena, Germany

[∥]Division of Physics, School of Computer Science, Physics and Mathematics, Linneaus University, 39233 Kalmar, Sweden

S *Supporting Information*

ABSTRACT: We report on temperature-dependent charge transport in heavily doped Mn^+-implanted GaAs nanowires. The results clearly demonstrate that the transport is governed by temperature-dependent hopping processes, with a crossover between nearest neighbor hopping and Mott variable range hopping at about 180 K. From detailed analysis, we have extracted characteristic hopping energies and corresponding hopping lengths. At low temperatures, a strongly nonlinear conductivity is observed which reflects a modified hopping process driven by the high electric field at large bias.

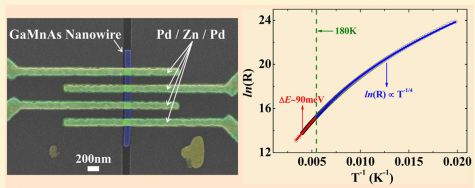

KEYWORDS: *Mott hopping, nanowires, self-assembly, ion-implantation, GaMnAs, spintronics*

A long-sought goal in electronics is the possibility to combine the two fundamental properties of spin and charge of electrons to create new devices that meet the expected requirements of computational power, data storage capacity, and communication performance in next-coming generations of electronic systems.[1] One of the most promising materials to realize such spintronic devices is $Ga_{1-x}Mn_xAs$. Mn ions incorporated into GaAs are not only responsible for magnetic moments, but they also act as acceptors providing holes that mediate ferromagnetic coupling between the Mn spins.[2−4] Most studies so far have focused on relatively high Mn concentrations to achieve a high Curie temperature, T_C. More recently, there has been an increasing interest in low-doped $Ga_{1-x}Mn_xAs$ motivated by ferromagnetic interactions in the Mott variable range hopping regime that are not well-described by any common local density carrier model.[5,6]

Semiconductor nanowires (NWs) have emerged as one of the key semiconductor technologies during recent years offering monolithic integration of III−V semiconductor nanodevices directly on a silicon chip. The flexibility in materials choice, reduced dimensions, and geometry of NWs provides unique possibilities to realize novel device families. NWs have already been considered as building blocks for nanoscale electronic and photonic devices, for example, single-electron transistors, biochemical sensors, light-emitting diodes, and solar cells.[7,8] Adding a magnetic degree of freedom to device design could potentially lead to the development of integrated 1D spintronic devices on silicon. Such a successful development requires access to high-quality single crystalline NWs with well-controlled electronic structure and magnetic properties. Up to now, it has been very difficult to realize such magnetic NWs due to segregation effects, leading to nonideal NW morphologies. Recently, we have successfully developed a new route toward heavily Mn doped single crystalline GaAs NWs via Mn^+-implantation under dynamic annealing conditions.[9] To further exploit these NWs in spintronic applications, a deeper understanding of their fundamental charge transport properties is necessary. One of the basic, yet least understood properties of $Ga_{1-x}Mn_xAs$ is the temperature dependence of the resistivity. Typical $Ga_{1-x}Mn_xAs$ samples exhibit a peak in resistivity around the Curie temperature, T_C, often with an additional weak increase in resistivity at low temperatures.[2] In less conductive samples, the aforementioned peak is less pronounced, and instead a broad resistivity shoulder is observed at T_C. While there are several reports on transport properties of bulk and thin film $Ga_{1-x}Mn_xAs$,[1,5,6,10] there is hardly any report on temperature-dependent transport measurements on $Ga_{1-x}Mn_xAs$ NWs. Previously reported quantum transport studies of ZnO[11] and InN[12] NWs showed that the conduction at low temperatures is dominated by a hopping mechanism. The absence of corresponding reports on $Ga_{1-x}Mn_xAs$ NWs most likely reflects the previously mentioned difficulties to grow single crystalline NWs with conventional techniques. In reduced-dimensional systems, it is expected that new features different from the bulk counterpart will arise. The Mn doped GaAs NWs are nearly ideal systems to investigate 1D transport mechanisms and localization related effects.

Received: June 21, 2012
Revised: August 3, 2012
Published: August 13, 2012

ACS Publications © 2012 American Chemical Society

In this Letter, we present significant insight into the hole transport properties of heavily doped Mn^+-implanted $Ga_{1-x}Mn_xAs$ NWs. From meticulous measurements of the temperature-dependent resistance, in combination with detailed analysis, it is shown that the transport is governed by different hopping mechanisms within an impurity band of localized Mn states. With decreasing temperature, there is a clear transition from nearest neighbor hopping (NNH) to Mott variable range hopping (VRH) conduction. It is also shown that electric field driven VRH dominates at low temperatures and high electric field strengths.

Single crystalline GaAs NWs of diameter 80 nm were grown by MOVPE using monodisperse Au particles as a catalyst.[13] To optimize the implantation angle, the NWs were grown on GaAs (001) substrates leading to an inclined growth direction of 35° toward the substrate. The as-grown NWs were subsequently implanted with 100 keV Mn^+ using a general purpose implanter (High Voltage Engineering Europa). The selected implantation dose of 1.8×10^{16} ions/cm^2 resulted in a Mn concentration of 2.5% (corresponding to a stoichiometry of $Ga_{1-x}Mn_xAs$ with $x = 0.05$) as determined by transmission electron microscopy (TEM)/energy-dispersive spectrometry (EDS). Results from computer simulations of the implanted ion profile, using our own developed *iradina* code,[14] show that this implantation energy leads to a fairly homogeneous concentration of Mn in the GaAs NWs. We have previously reported that the imposed dynamic annealing conditions during implantation lead to high crystalline quality and ideal NW morphology after implantation.[9] For transport measurements, NWs were mechanically transferred onto a silicon substrate covered by a 210 nm thick silicon dioxide layer on which reference markers and macroscopic metal pads were predefined. Electron beam lithography (EBL) was used to define contacts connecting individual NWs to the macroscopic contact pads. The NWs were etched in HCl/H_2O solution for 20 s, followed by a 2 min surface passivation in a heated (40 °C) NH_4S_x/H_2O solution. The Ohmic contacts to the NWs were made by evaporating Pd (2 nm)/Zn (20 nm)/Pd (83 nm) after etching and passivation. The sample processing was finalized by a lift-off process. To investigate the possible influence of contact resistance, 2-probe and 4-probe measurements were compared. From these measurements we conclude that the contact resistance is negligible compared to the NW resistance at all temperatures (Figure S1 of the Supporting Information). The transport measurements were performed in a Janis VariTemp superconducting cryomagnet system (model 8T-SVM).

Figure 1 shows current voltage ($I-V$) characteristics of a single $Ga_{0.95}Mn_{0.05}As$ NW. At room temperature, the slightly nonlinear and antisymmetric $I-V$ curve suggests that the transport could be governed by incoherent hole hopping between spatially adjacent energy states in the impurity band formed by the Mn^+ implantation.[15] The expected current versus bias relation for such a hopping process is given by

$$I \sim \sinh\left(\frac{AV}{k_B T}\right) \quad (1)$$

where A is a constant which depends on the hopping distance and the distance between the contacts on the NW. For $T > 50$ K, all $I-V$ curves could be perfectly fitted by eq 1 above. At lower temperatures, the $I-V$ curves become increasingly nonlinear, however with maintained antisymmetry with respect to the bias (Figure 1, lower inset). To further unravel the

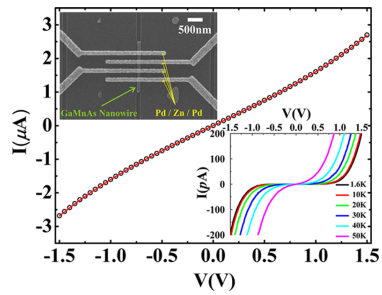

Figure 1. Current−voltage ($I-V$) characteristics of a single $Ga_{1-x}Mn_xAs$ NW ($x = 0.05$) at room temperature. Circles are the experimental data, while the red solid curve is a fitting to eq 1. The lower inset shows the strongly nonlinear $I-V$ characteristics at lower temperatures. The upper inset shows an SEM micrograph of a NW with contacts for 4-point resistance measurements.

electronic transport mechanism of the NWs, we study the temperature dependence of the resistance of our devices from 1.6 to 300 K. Figure 2 shows the resistance (R) versus

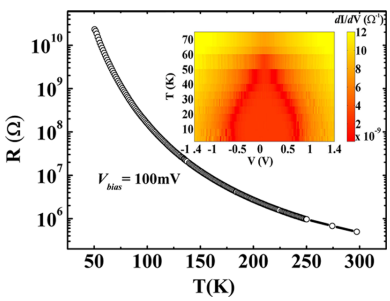

Figure 2. Resistance dependence on the temperature at a bias of 0.1 V. The inset shows the differential conductance (dI/dV) as a function of bias and temperature.

temperature (T) plot in the temperature range 50−300 K for a single $Ga_{0.95}Mn_{0.05}As$ NW at a constant bias $V = 0.1$ V within the linear region of the $I-V$ curve. The NWs exhibit a high resistance of about 0.5 MΩ at 300 K, which increases by 4 orders of magnitude as the temperature is decreased to 50 K. In a constant mobility drift model, the room temperature resistance of 0.5 MΩ corresponds to a hole concentration of 2.0×10^{17} cm^{-3}, assuming a reduced hole mobility of 30 cm^2·V^{-1}·s^{-1} [16] and a 80 nm NW diameter. This value of the hole mobility is taken from studies of p-doped GaAs NWs[14] with slightly larger NW diameters. We do not exclude the possibility that the effective hole mobility in our samples could be smaller, yielding a larger hole concentration than what stated above. Note however that the value reported here is consistent with the hole concentration extracted with a different method in $Ga_{1-x}Mn_xAs$ NWs similar to the ones studied in this work.[17] In our estimate, we have neglected any influence of, for example, Fermi level pinning at the surface of the NW. The hole density is much lower than expected considering the 2.5% Mn detected with EDS. Possible reasons for the low carrier

dx.doi.org/10.1021/nl302318f | *Nano Lett.* 2012, 12, 4838−4842

concentration include, for example, compensation due to interstitial Mn impurities and As antisites created by the ion implantation.

To investigate the bias dependence of the conductance more in detail, we plot the differential conductance dI/dV as a function of both T and applied bias V in Figure 2 (inset). The conductance due to thermally activated hopping falls below the detection limit at 0.1 V bias below 50 K. It is noted that no features revealing the metal-to-insulator transition, generally observed near T_C in weakly metallic $Ga_{1-x}Mn_xAs$, are observed in Figure 2. At all measured temperatures and applied biases, an insulating behavior ($dR/dT < 0$) is indeed observed. Different transport mechanisms have been proposed in the literature for doped semiconductors.[15] For a p-type semiconductor at low temperatures, most of the free holes are recaptured by the acceptors. As a result, hole conduction in the valence band becomes less important, and hole hopping directly between acceptors in the impurity band provides the main contribution to the conductivity. The hopping conduction is associated with hole jumping from occupied acceptors to empty ones. Hopping conductivity is governed by the hopping probability between impurity sites. A hopping hole will always try to find the lowest activation energy ΔE, given by the energy separation between adjacent Mn-related states, and the corresponding shortest hopping distance. There is an optimum hopping distance r, which maximizes the hopping probability. At thermal equilibrium (zero bias), the hopping probability is given by

$$P \sim \exp(-2r/a - \Delta E/k_B T) \tag{2}$$

where k_B is the Boltzmann constant and a is the localization length of the hole wave function in the impurity band. The hopping distance r, which can be much longer than the localization length at low temperatures,[18] depends on the temperature according to

$$r = [9a/(8\pi N(E_F)k_B T)]^{1/4} \tag{3}$$

for a 3D system. Here $N(E_F)$ is the density of states near the Fermi level. The corresponding activation energy is given by

$$\Delta E = 3/[4\pi r^3 N(E_F)] \tag{4}$$

At elevated temperatures, r eventually becomes equal to the nearest neighbor distance d. The hopping probability then becomes

$$P \sim \exp(-\Delta E_A/k_B T) \tag{5}$$

which resembles an Arrhenius relation describing a nearest-neighbor hopping mechanism with an activation energy ΔE_A. According to the theory of VRH proposed by Mott,[19,20] if the effect of electron−electron interactions is negligible, and a constant $N(E_F)$ is assumed, the temperature dependence of the resistance in the linear (Ohmic) region can be expressed as

$$R = R_0 \exp\left[\frac{T_0}{T}\right]^p \tag{6}$$

where $p = 1/4$, $1/3$, or $1/2$ for 3D, 2D, and 1D systems, respectively. Here R_0 and T_0 denote materials parameters. The exponent p in eq 6 is precisely determined by the slope of the double logarithmic plot of $W = d(\log(G))/d(\log(T))$ versus T, where $G = 1/R$ is the conductance of the NW.[21] As shown in the lower inset of Figure 3, a change of slope of $\log(d(\log(G))/d(\log(T)))$ versus $\log(T)$ is observed around 180 K. The value of p amounts to about 0.25 in the temperature region 50 K < T < 180 K and 0.9 above 180 K, respectively. A value $p = 0.25$ corresponds to 3D Mott VRH, whereas $p = 0.9$ is consistent with a NNH mechanism.

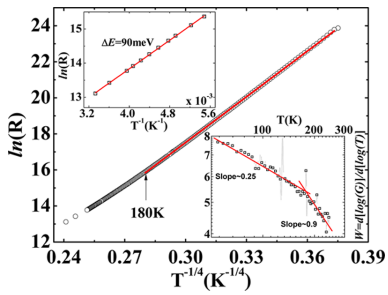

Figure 3. Resistance fitted (red solid line) to the Mott VRH model with $p = 1/4$ (eq 6) in the temperature range 50 K < T < 180 K. Upper inset: Arrhenius plot of the resistance data in the temperature interval 180 K < T < 300 K. Lower inset: Plot of d log(G)/d log(T) versus T, where the red solid fitting lines were used to extract the p-factors.

From the R versus T behavior, several characteristic parameters describing the charge transport in NWs can be extracted. The $\ln(R)$ versus $T^{-1/4}$ plot for $Ga_{0.95}Mn_{0.05}As$ NWs is shown in Figure 3. From the slope of the curve between 50 and 180 K, the fitting parameter T_0 can be estimated. T_0 is related to the hole localization length a and density of states near the Fermi level $N(E_F)$ according to

$$T_0 = 18/k_B a^3 N(E_F) \tag{7}$$

From the slope of the linear fit to $\ln(R)$ versus $T^{-1/4}$ curve in Figure 3, we deduce a value of $T_0 = 5.2 \times 10^7$ K, which corresponds to a $N(E_F) = 4.0 \times 10^{18}$ (eV·cm^3)$^{-1}$. The value of a is assumed to be of the same order as the acceptor Bohr radius for Mn in GaAs (~1 nm). From eqs 3 and 4 we deduce an average hopping energy ΔE of 34 meV and a hopping length of $r = 12.0$ nm at 50 K. At 180 K, ΔE increases to 90 meV while the hopping length decreases to 8.7 nm. The finding of such large hopping lengths, particularly at relatively high temperatures, is puzzling. Within a single-particle hopping scenario the hopping length r should eventually become of the order of the average impurity distance. At the moment we have no satisfactory explanation of this result. As already mentioned, the low carrier concentration, which at first hand indeed would imply a large distance between the hopping sites, most likely reflects efficient compensation due to interstitial Mn impurities and As antisites created by the ion implantation. More detailed investigations are needed to unravel the hopping processes through an impurity band influenced by these impurity states. Moreover, recent studies investigating the prototype ferromagnetic semiconductor $Ga_{1-x}Mn_xAs$ shows that our understanding of the electronic structure in samples in relatively high doping regimes is still far from complete.[22] In particular, some of these measurements seem to suggest that all of the acceptor holes might reside in states generated by the Mn impurities.[23] Hopping processes in the presence of many localized nearby holes might differ substantially from the usual single-particle hopping scenario, and correlation effects might not be excluded. Our consistent finding of larger than expected hopping distances might signal a problematic attempt of

dx.doi.org/10.1021/nl302318f | Nano Lett. 2012, 12, 4838−4842

analyzing a correlated system with a single-particle scheme. Similar indications occur also when studying thermoelectric effects in similar samples.[17] Above 180 K, the NNH mechanism dominates with activation energy of 90 meV. The Arrhenius plot is shown in Figure 3 (upper inset). The extracted p-factor of 0.9 for $T > 180$ K is close to 1 also valid for valence band conduction. We thus cannot exclude a contribution to the conductivity from holes excited to the valence band. The NWs used here have a diameter of ∼80 nm, which is much larger than the hopping length, so the hole transport reveals mainly three-dimensional character. At low temperatures (< 50 K) the conduction mechanism of VRH is modified at large biases. Under high electric field conditions, a hole can jump from a filled state to an empty state along the field direction with an activation energy reduced by an amount eEr.[24,25] When the electric field reaches a critical value E_C, such that the energy eE_Cr gained during a hop becomes comparable to the activation energy for hopping, holes can move along the field. The resistance which becomes temperature independent can then be expressed in the form

$$R = R_{0E} \exp\left[\frac{E_0}{E}\right]^p \tag{8}$$

where R_{0E} and E_0 are materials constants. E_0 is proportional to T_0 as

$$E_0 = (k_B T_0/2ea) \tag{9}$$

where a is the localization length as stated before.

In Figure 4, we have plotted ln R versus $E^{-1/4}$. It is readily observed that the curves at different temperatures merge on a single line at a temperature-dependent E_C. From the slope of this line, we deduce $E_0 = 2.0 \times 10^{12}$ V·m^{-1}. Inserting the values of E_0 and T_0 into eq 9 gives the localization length $a = 1.1$ nm, which is in very good agreement with the expected Mn acceptor Bohr radius.

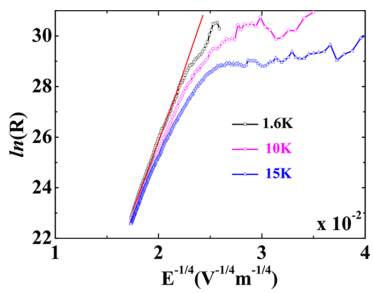

Figure 4. Resistance as a function of electric field and temperature. The red solid line is a least-squares fit to the high-field data.

In conclusion, we have reported on detailed temperature-dependent resistance measurements and $I-V$ characteristics of heavily Mn^+-implanted single crystalline $Ga_{0.95}Mn_{0.05}As$ NWs. Whereas TEM confirms that the NWs are single crystalline, the electrical data exhibit clear evidence of disorder. The transport is governed by variable range hopping at lower temperatures (50 K < T < 180 K) with a crossover to nearest neighbor hopping at about $T > 180$ K. The extracted values of optimal hopping distance are considerably larger than the average impurity separation, even at high temperatures ($T \sim 180$ K), suggesting that correlation effects beyond a single-particle picture might be at play. At low temperatures and high electric field strengths, signs of field-induced variable range hopping are revealed. These fundamental studies provide critical insight into the transport mechanisms likely to be found in next-generations of integrated nanoscale electronic devices compatible with main-stream silicon technology.

■ ASSOCIATED CONTENT

Ⓢ Supporting Information

Current−voltage characteristics measured with 2-probe and 4-probe geometry. This material is available free of charge via the Internet at http://pubs.acs.org.

■ AUTHOR INFORMATION

Corresponding Author

*E-mail: hakan.pettersson@hh.se.

Author Contributions

⊥These authors contributed equally to this work and are cofirst authors.

Notes

The authors declare no competing financial interest.

■ ACKNOWLEDGMENTS

The authors acknowledge financial support from the Swedish Research Council, the Knut and Alice Wallenberg Foundation, the Swedish National Board for Industrial, Technological Development, the Swedish Foundation for Strategic Research and the Nordforsk research network “Nanospintronics; theory and simulations”. One of the authors, W.P., Jr., gratefully acknowledges financial support from the Pará Education Secretary (SEDUC) and the Pará Government School (EGPA).

■ REFERENCES

(1) Ohno, H. *Science* **1998**, *281*, 951.
(2) Dietl, T. *Semicond. Sci. Technol.* **2002**, *17*, 377.
(3) MacDonald, A. H.; Schiffer, P.; Samarth, N. *Nat. Mater.* **2005**, *4*, 195.
(4) Ohno, H.; Chiba, D.; Matsukura, F.; Omiya, T.; Abe, E.; Dietl, T.; Ohno, Y.; Ohtani, K. *Nature* **2000**, *408*, 944.
(5) Dobrowolska, M.; Tivakornsasithorn, K.; Liu, X.; Furdyna, J. K.; Berciu, M.; Yu, K. M.; Walukiewicz, W. *Nat. Mater.* **2012**, *11*, 444.
(6) Sheu, B. L.; Myers, R. C.; Tang, J.-M.; Samarth, N.; Awschalom, D. D.; Schiffer, P.; Flatté, M. E. *Phys. Rev. Lett.* **2007**, *99*, 227205.
(7) Cui, Y.; Wei, Q.; Park, H.; Lieber, C. M. *Science* **2001**, *293*, 1289.
(8) Thelander, C.; Mårtensson, T.; Björk, M. T.; Ohlsson, B. J.; Larsson, M. W.; Wallenberg, L. R.; Samuelson, L. *Appl. Phys. Lett.* **2003**, *83*, 2052.
(9) Borschel, C.; Messing, M. E.; Borgström, M. T., Jr.; W., P.; Wallentin, J.; Kumar, S.; Mergenthaler, K.; Deppert, K.; Canali, C. M.; Pettersson, H.; Samuelson, L.; Ronning, C. *Nano Lett.* **2011**, *11*, 3935.
(10) Kyrychenko, F. V.; Ullrich, C. A. *Phys. Rev. B* **2009**, *80*, 205202.
(11) Ma, Y. J; Zhang, Z.; Zhou, F.; Lu, L.; Jin, A.; Gu, C. *Nanotechnology* **2005**, *16*, 746.
(12) Huang, L.; Li, D.; Chang, P.; Chu, S.; Bozler, H.; Beloborodov, I. S.; Lu, J. G. *Phys. Rev. B* **2011**, *83*, 245310.
(13) Mikkelsen, A.; Sköld, N.; Ouattara, L.; Borgström, M. T.; Andersen, J. N.; Samuelson, L.; Seifert, W.; Lundgren, E. *Nat. Mater.* **2004**, *3*, 519.
(14) Borschel, C.; Ronning, C. *Nucl. Instrum. Methods Phys. Res., Sect. B* **2011**, *269*, 2133.
(15) Singh, J. *Physics of semiconductors and their heterostructures*; McGraw-Hill, Inc.: New York, 1993.
(16) Ketterer, B.; Uccelli, E.; Morral, A. F. *Nanoscale* **2012**, *4*, 1789.

(17) Wu, P.; Paschoal, W., Jr.; Kumar, S.; Borschel, C.; Ronning, C.; Canali, C. M.; Samuelson, L.; Pettersson, H.; Linke, H. *J. Nanotechnol.*, submitted.
(18) Shklovskii, B. I.; Efros, A. L. *Electronic properties of doped semiconductors*, Springer-Verlag, Inc.: New York, 1984.
(19) Mott., N. F. *Philos. Mag.* **1969**, *19*, 835.
(20) Lee, P. A. *Rev. Mod. Phys.* **1985**, *57*, 287.
(21) Zabrodskii, A. G. *Philos. Mag.* **2001**, *81*, 1131.
(22) Ohya, S.; Takata, K.; Tanaka, M. *Nat. Phys.* **2011**, *7*, 342.
(23) Flatté, M. E. *Nat. Phys.* **2011**, *7*, 285.
(24) Shahar, D.; Ovadyahu, Z. *Phys. Rev. Lett.* **1990**, *64*, 2293.
(25) Yu, D.; Wang, C.; Wehrenberg, B. L.; Guyot-Sionnest, P. *Phys. Rev. Lett.* **2004**, *92*, 216802.

Paper III

Hindawi Publishing Corporation
Journal of Nanotechnology
Volume 2012, Article ID 480813, 5 pages
doi:10.1155/2012/480813

Research Article

Thermoelectric Characterization of Electronic Properties of GaMnAs Nanowires

Phillip M. Wu,[1] Waldomiro Paschoal Jr.,[1,2] Sandeep Kumar,[1] Christian Borschel,[3] Carsten Ronning,[3] Carlo M. Canali,[4] Lars Samuelson,[1] Håkan Pettersson,[1,2] and Heiner Linke[1]

[1] *Division of Solid State Physics and The Nanometer Structure Consortium (nmC@LU), Lund University, P.O. Box 118, 221 00 Lund, Sweden*
[2] *Department of Mathematics, Physics, and Electrical Engineering, Halmstad University, P.O. Box 823, 301 18 Halmstad, Sweden*
[3] *Institute for Solid State Physics, Jena University, Max-Wien-Platz 1, 07743 Jena, Germany*
[4] *Division of Physics, School of Computer Science, Physics and Mathematics, Linnæus University, 39233 Kalmar, Sweden*

Correspondence should be addressed to Phillip M. Wu, phillip.wu@ftf.lth.se

Received 21 June 2012; Accepted 23 August 2012

Academic Editor: Magnus T. Borgstrom

Copyright © 2012 Phillip M. Wu et al. This is an open access article distributed under the Creative Commons Attribution License, which permits unrestricted use, distribution, and reproduction in any medium, provided the original work is properly cited.

Nanowires with magnetic doping centers are an exciting candidate for the study of spin physics and proof-of-principle spintronics devices. The required heavy doping can be expected to have a significant impact on the nanowires' electron transport properties. Here, we use thermopower and conductance measurements for transport characterization of $Ga_{0.95}Mn_{0.05}As$ nanowires over a broad temperature range. We determine the carrier type (holes) and concentration and find a sharp increase of the thermopower below temperatures of 120 K that can be qualitatively described by a hopping conduction model. However, the unusually large thermopower suggests that additional mechanisms must be considered as well.

1. Introduction

Self-assembled semiconducting epitaxial nanowires are promising building blocks for field effect transistors [1], sensors [2], and solar cells [3]. An exciting new direction, which has recently been shown to be possible due to successful incorporation of magnetic Mn dopants into epitaxially grown GaAs nanowires (NWs) [4–11], is their use for proof-of-concept spintronics devices [12]. The doping techniques are advancing rapidly, and it has recently been shown that ion beam implantation can produce single crystalline, homogeneously doped GaMnAs NWs [13]. Furthermore, a recent study found that the Curie temperature of GaMnAs nanostrips could be enhanced to 200 K with nanostructure engineering [14], suggesting the possibility for nanowire-based devices to operate at higher temperatures compared to thin films or bulk. In addition to the exciting possibilities for application, from the fundamental point of view, ferromagnetic NWs will provide an opportunity to investigate the spin-Seebeck effect in reduced dimensions [15]. A deeper understanding of how spins and phonons couple thermodynamically could in turn lead to fundamentally new applications, such as spin-based cooling and magnetically sensitive thermoelectrics.

Here, we investigate the thermoelectric properties of $Ga_{0.95}Mn_{0.05}As$ NWs. Combining thermopower and conductance (or resistance) measurements can provide information on carrier density when conventional characterization techniques via the Hall effect and field effect are not possible [16]. We were able to estimate the hole carrier density from thermopower measurements to be $p \sim 10^{17}$-$10^{18}\,\mathrm{cm}^{-3}$ in our NW. In addition, we find a dramatic rise in the resistance and thermopower of the NW below 120 K [17–19]. The resistance versus temperature measurements point to the role of Mott variable range hopping (VRH) transport with activation energy 62 meV at 100 K and hopping lengths of 11 nm. We show that the addition of a term due to Mott variable range hopping (VRH) transport [20–22] can also

qualitatively describe the rise in thermopower observed in these $Ga_{0.95}Mn_{0.05}As$ NWs. However, our model suggests that a simple parabolic-band picture is not fully adequate, implying that more complex behavior is taking place.

2. Experimental Methods

GaAs NWs of 40 nm diameter were grown by MOVPE and subsequently implanted with Mn ions to doping concentrations of 0.5 to 2.9%, corresponding to $Ga_{1-x}Mn_xAs$ with $x = 0.01$ to 0.058 stoichiometry. Both simulations and transmission electron microscopy (TEM) showed that the NWs are of high crystalline quality after implantation and that the Mn is reasonably homogeneously distributed. In this work, we concentrate on the higher doped wires. The NW growth and implantation techniques were discussed in detail previously [13].

To prepare devices for thermoelectric characterization, NWs were collected from the growth substrate with cleanroom tissue paper and then brushed onto Si/SiO_2 chips with 110 nm thick oxide. A thick metallic plane was evaporated on the backside of the chip for voltage-gating measurements. We searched optically for suitable NWs for processing and determined the location of the NWs relative to predefined Au alignment marks on the SiO_2 chips. Contacts to the NWs were fabricated via standard e-beam lithography processes. Briefly, 950-A5 PMMA was spun onto the sample at 5000 rpm for 60 s and baked at 180°C for 5 minutes. After the contact pattern exposure, the resistance was developed in MIBK : IPA = 1 : 3 for 30 s. To ensure good ohmic contacts to the NWs, we performed the following procedures: the samples were treated in HCl/H_2O solution for 15 seconds followed by passivation in $(NH_4)_2S_x$ solution at 40°C for 2 minutes. Then metal contacts of Pd (10 nm)/Zn (10 nm)/Pd (35 nm) were evaporated followed by lift-off [23]. Measurements were done in a Janis Varitemp cryostat between 60 K and 190 K.

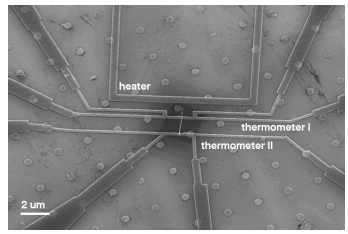

FIGURE 1: Scanning electron microscope image of a typical nanowire device with heater and thermometer metallic microstrip lines is shown. In a separate measurement, the contact electrodes can be independently used to probe the voltage drop along the nanowire or conductance. Image is of a device similar to the one that is measured.

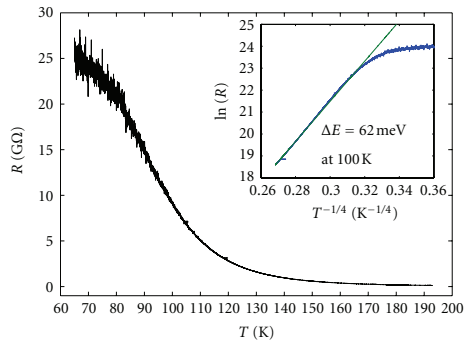

FIGURE 2: $Ga_{0.95}Mn_{0.05}As$ nanowire resistance as a function of temperature. The inset shows a plot of $\ln(R)$ versus $T^{-1/4}$, with the extracted activation energy of 62 meV at 100 K.

3. Results and Discussions

Figure 1 shows a scanning electron microscope (SEM) image of a typical device similar to the one measured. Current is driven through an on-chip metallic microstrip line to generate a temperature differential ΔT along the length of the NW. Metallic contacts to the NWs can be used to probe in separate measurements the voltage drop or conductance. The metal contacts also serve as thermometers, where we calibrate the four-probe resistance change of the metal against the cryostat temperature T; see thermometer I and II in Figure 1. The change in the resistance of the metallic thermometers as the cryostat temperature is changed allows for the determination of the temperature at the metal to nanowire contact point to within 0.1 K. Similar device geometries with patterned microstrip line heaters and thermometers have been used to study thermopower in, for example, carbon nanotubes [24, 25] and other materials [26]. We typically measured in the linear response regime, maintaining $\Delta T \ll T$. For the substrate temperatures shown, the gradient generated along the wire was typically $\Delta T \sim 1$ K. A metallic backgate was also available for field effect, but we found that the NW transport did not respond significantly to the applied gate voltages.

We discuss first the electronic transport of the NW as a function of temperature. In Figure 2, we show the resistance calculated from the measured two terminal conductances. The contact resistances obtained from our fabrication procedure were found to be from 500 Ω to 1 kΩ (for wires with 4 terminal contacts), and we conclude that the measured response is due to the wire itself [27]. The NWs show dramatic increase in the resistance for $T < 120$ K, and this rise saturates below $T \sim 80$–90 K. In order to obtain a better understanding of the transport mechanisms down to 60 K, we plot $\ln(R)$ versus $T^{-1/4}$ in the inset of Figure 2. The linearity of such a trace indicates that Mott variable range hopping may likely be in play [20, 27]. Deviation from linearity occurs around $T^{-1/4} = 0.32$ or $T \sim 95$ K. From the slope of this trace, we estimate the carrier density to be approximately $3 * 10^{18}$ cm^{-3} at 100 K with hopping lengths

of 11 nm. This allows a determination of an activation energy of $\Delta E = 62$ meV at 100 K. For larger 80 nm diameter wires, similar behavior was found though the hopping transport was found to persist down to $T \sim 50$ K [27].

Figure 3 shows the measured thermopower, which is defined as $S = -\Delta V/\Delta T$, where ΔV is the measured voltage drop across the nanowire. The positive sign of the measured thermopower indicates that the transport carriers are holes. This is expected for Mn-doped GaAs since substitutional Mn is an acceptor in GaAs. The thermopower is seen to increase dramatically for temperatures lower than 120 K, which is the temperature where the electrical resistance also begins to sharply increase. In order to understand why the thermopower rises to the rather large values of ~800 μV/K, we first consider the thermopower in the paramagnetic regime (without taking into account hopping transport) consisting of the following two terms:

$$S_{\text{tot}} = S_{\text{diff}} + S_{\text{exch}}. \tag{1}$$

The first term is essentially the semiclassical Mott relation for diffusive transport [16],

$$S = -\frac{\pi^2 k_B^2 T}{3|e|}\frac{d\ln\sigma}{dE}\bigg|_{E=E_F} = -\frac{\pi^2 k_B^2 m^*}{(3\pi^2)^{2/3}\hbar^2|e|}\frac{T}{p^{2/3}}. \tag{2}$$

Here, σ is the conductivity, k_B is the Boltzmann constant, e is the electron charge, $\hbar$ is Planck's constant, and p is the carrier density. The hole effective mass for GaMnAs is taken to be $m^* = 0.5 * m_e$, where m_e is the free electron mass [28]. The second term is from exchange mechanisms

$$S_{\text{exch}} = \frac{S_0 T}{T + T_0}, \qquad S_0 = \frac{4\pi^2 k_B}{e} D(E_F) I_{pd} V \frac{\rho_{\text{exch}}}{\rho}, \tag{3}$$

where $D(E_F)$ is the density of states at the Fermi energy, I_{pd} is the exchange integral between carriers and magnetic centers, V is the nonmagnetic scattering potential, and ρ_{exch}/ρ is the ratio between exchange contribution to resistivity to total resistivity. Here, T_0 is a material-dependent parameter with weak temperature and magnetic impurity dependence, and for thin films it is found to be $T_0 = 150$ K [21]. We utilize these functional forms to obtain a fit to the data above 120 K, where the thermopower is relatively flat, as seen in Figure 3 (blue dot dash curve). We find that the parameters that give the best fit to the curve are $p \sim 3 * 10^{17}$ cm^{-3} and $S_0 \sim 4$ mV/K, with $T_0 = 150$ K fixed based on the thin film value. Due to the limited number of data points, we believe our estimate for the density to be correct to within an order of magnitude. This is comparable to what has been observed for comparable nanowires [27] and is, within our accuracy, consistent with the estimate obtained from the resistance versus temperature curves above. Note that the value of S_0 is unusually large, a point that we will return to below. These results demonstrate that thermopower presents a powerful method for extracting carrier sign and density when conventional Hall effect and field effect techniques are not possible.

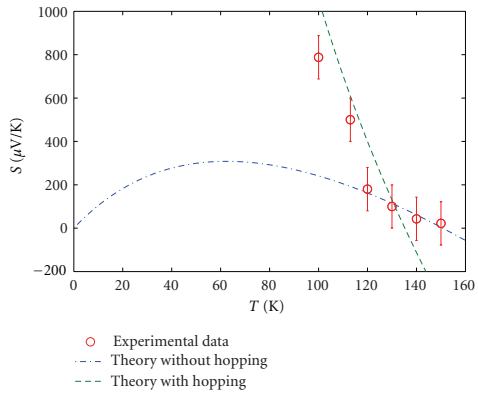

FIGURE 3: Thermopower for the $Ga_{0.95}Mn_{0.05}As$ nanowire device as function of temperature. The experimental data matches well at high temperature with values calculated using a model without hopping [21]. However, at temperatures below 120 K, the nanowire thermopower starts to rise far above the extrapolation. Addition of a hopping term qualitatively accounts for the rise in thermopower.

Below 120 K, it is clear that additional contributions to the thermopower must be considered to explain the observed data. Taking a cue from the temperature dependence of the resistance, we consider adding a term due to hopping conduction. We see below that this hopping contribution, S_{hop}, can qualitatively describe the observed experimental behavior. We start with a hopping term of the form [21]

$$S_{\text{hop}} = \left(F_{\text{corr}} * \frac{k_B}{e}\right)\left(\frac{\Delta E}{k_B T} + A\right), \tag{4}$$

where A does not have significant temperature dependence and includes an additional factor, F_{corr}, to account for electron correlations. Without F_{corr}, (4) expresses that, in the simple case of single particle, noninteracting transport, the thermopower of a device or material essentially measures the average energy (here assumed to be the activation energy ΔE) where transport takes place. By plotting the experimental data versus $1/T$, and taking the correlation factor, $F_{\text{corr}} \sim 5$, we can extract the activation energy $\Delta E \sim 63$ meV, in good agreement with that seen in the $R(T)$, as seen in Figure 4. Based on this, we can calculate the full theoretical trace including hopping mechanisms as shown in Figure 3 (green-dashed line). We see that inclusion of this hopping mechanism can describe the observed rise in thermopower. At 100 K, the theoretical trace seems to overshoot the experimental data. This is consistent with the fact that the $\ln(R)$ versus $T^{-1/4}$ trace starts to deviate from linearity around 95 K.

Comparing the results from thermopower to that obtained from the electrical resistance, we see that an activation energy of 62 meV at 100 K is deduced from Mott VRH theory [27]. In order for (4) to give a comparable extracted

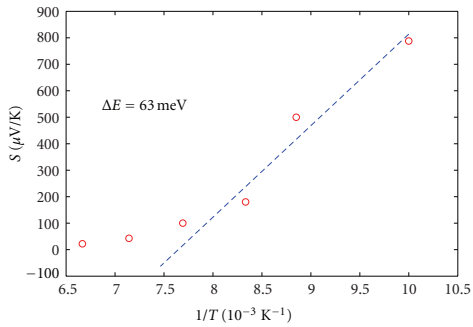

FIGURE 4: Extracted hopping activation energy, based on a hopping term $S_{hop} \sim \Delta E/T$. Further discussion can be found in the text.

activation energy, we required $F_{corr} \sim 5$. This implies strongly that correlation effects play a more significant role here. The fact that F_{corr} is much larger than one is not so surprising if we consider the unusually large measured thermopower. Indeed, colossal thermopowers have been seen in strongly correlated semiconductors such as FeSb [29], where the large thermopowers are presumed to be a result of the Fe 3d-states and Sb 5p-states hybridizing into a coherent, high mobility state. We note that compared to 2D GaMnAs films, which exhibit hole-mediated ferromagnetic coupling, these GaMnAs nanowires are clearly in the hopping regime, with a relatively low hole concentration and large hopping lengths. These observations are an indication of acceptor compensation from Mn interstitial impurities and As antisites, which were created by the ion beam implantation process. More analysis will be necessary to understand the relative importance of these two contributions. Clearly then, our results (i) highlight the important role that thermopower measurements can play as a characterization tool complementary to conductance measurements, and (ii) that our heavily Mn-doped nanowires exhibit more complex electronic behavior than is apparent from conductance measurements, leaving much room for further investigation.

4. Conclusions

In this work, we studied the thermopower and conductance of $Ga_{0.95}Mn_{0.05}As$ nanowires. We utilize thermopower measurements as a means to estimate the hole carrier concentration when Hall effect and field effect are not possible. We find from thermopower and from conductance measurements the hole density $p \sim 10^{17}$-10^{18} cm^{-3}. Furthermore, we observe dramatic increases in both thermopower and resistance at low temperature. The resistance versus temperature suggests that the NW is in the regime of variable range hopping transport. From the thermopower, we deduce that additional correlated phenomena must be taking place. These fundamental studies provide critical insight into the transport mechanisms likely to be found in next-generation GaMnAs and ferromagnetic NWs.

Acknowledgments

The authors acknowledge support from nmC@LU, Swedish Energy Council (Energimyndigheten) Grant no. 32920-1, the Swedish Research Council, the Strategic Foundation, and Knut and Alice Wallenberg Foundation. One of the authors, W. Paschoal Jr., gratefully acknowledges financial support from the Pará Education Secretary (SEDUC) and the Pará Government School (EGPA) of Brazil.

References

[1] Y. Cui, Z. Zhong, D. Wang, W. U. Wang, and C. M. Lieber, "High performance silicon nanowire field effect transistors," *Nano Letters*, vol. 3, no. 2, pp. 149–152, 2003.

[2] P. H. Yeh, Z. Li, and Z. L. Wang, "Schottky-gated probe-free ZnO nanowire biosensor," *Advanced Materials*, vol. 21, no. 48, pp. 4975–4978, 2009.

[3] A. I. Hochbaum and P. Yang, "Semiconductor nanowires for energy conversion," *Chemical Reviews*, vol. 110, no. 1, pp. 527–546, 2010.

[4] J. Sadowski, P. Dłuzewski, S. Kret et al., "GaAs:Mn nanowires grown by molecular beam epitaxy of (Ga,Mn)As at MnAs segregation conditions," *Nano Letters*, vol. 7, no. 9, pp. 2724–2728, 2007.

[5] F. Martelli, S. Rubini, M. Piccing et al., "Manganese-induced growth of GaAs nanowires," *Nano Letters*, vol. 6, no. 9, pp. 2130–2134, 2006.

[6] M. F. H. Wolff, D. Görlitz, K. Nielsch, M. E. Messing, and K. Deppert, "Synthesis and magnetic characterization of MnAs nanoparticles via nanoparticle conversion," *Nanotechnology*, vol. 22, no. 5, Article ID 055602, 2011.

[7] J. Adell, I. Ulfat, J. Sadowski, L. Ilver, and J. Kanski, "Electron spectroscopic studies of nanowires formed by (GaMn)As growth on GaAs(111)B," *Solid State Communications*, vol. 151, no. 11, pp. 850–854, 2011.

[8] H. C. Jeon, T. W. Kang, T. W. Kim, Y. J. Yu, W. Jhe, and S. A. Song, "Magnetic and optical properties of (Ga1-x Mnx) As diluted magnetic semiconductor quantum wires with above room ferromagnetic transition temperature," *Journal of Applied Physics*, vol. 101, no. 2, Article ID 023508, 2007.

[9] A. Rudolph, M. Soda, M. Kiessling et al., "Ferromagnetic GaAs/GaMnAs core-shell nanoWires Grown by Molecular Beam Epitaxy," *Nano Letters*, vol. 9, no. 11, pp. 3860–3866, 2009.

[10] H. S. Kim, Y. J. Cho, K. J. Kong et al., "Room-temperature ferromagnetic Ga1-x-MnxAs (X <= 0.05) nanowires: dependence of electronic structures and magnetic properties on Mn content," *Chemistry of Materials*, vol. 21, no. 6, pp. 1137–1143, 2009.

[11] P. Dluzewski, J. Sadowski, S. Kret, J. Dabrowski, and K. Sobczak, "TEM determination of directions of (Ga,Mn)As nanowires grown by MBE on GaAs(001) substrates," *Journal of Microscopy*, vol. 236, no. 2, pp. 115–118, 2009.

[12] D. D. Awschalom, N. Samarth, and D. Loss, *Semiconductor Spintronics and Quantum Computation*, Springer-Verlag, Heidelberg, Germany, 2002.

[13] C. Borschel, M.E. Messing, M.T. Borgstrom et al., "A new route toward semiconductor nanospintronics: highly Mn-doped GaAs nanowires realized by ion-implantation under dynamic annealing conditions," *Nano Letters*, vol. 11, no. 9, pp. 3935–3940, 2011.

[14] L. Chen, X. Yang, F. Yang et al., "Enhancing the curie temperature of ferromagnetic semiconductor (Ga,Mn)As to 200 K via nanostructure engineering," *Nano Letters*, vol. 11, no. 7, pp. 2584–2589, 2011.

[15] Y. Dubi and M. Di Ventra, "Thermospin effects in a quantum dot connected to ferromagnetic leads," *Physical Review B*, vol. 79, no. 8, Article ID 081302, 2009.

[16] C. H. Lee, G. C. Yi, Y. M. Zuev, and P. Kim, "Thermoelectric power measurements of wide band gap semiconducting nanowires," *Applied Physics Letters*, vol. 94, no. 2, Article ID 022106, 2009.

[17] Y. I. Ravich and S. A. Nemov, "Hopping conduction via strongly localized impurity states of indium in PbTe and its solid solutions," *Semiconductors*, vol. 36, no. 1, pp. 1–20, 2002.

[18] O. E. Parfenov and F. A. Shklyaruk, "On the temperature dependence of the thermoelectric power in disordered semiconductors," *Semiconductors*, vol. 41, no. 9, pp. 1021–1026, 2007.

[19] D. Gitsu, T. Huber, L. Konopko, and A. Nikolaeva, "Peculiarities of thermopower in Bi microwires at low temperatures," *Physica Status Solidi B*, vol. 242, no. 12, pp. 2497–2502, 2005.

[20] N. F. Mott and E. A. Davis, *Electronic Processes in Non-Crystalline Materials*, Clarendon Press, Oxford, UK, 1979.

[21] V. Osinniy, K. Dybko, A. Jedrzejczak et al., "Thermoelectric studies of electronic properties of ferromagnetic GaMnAs layers," *Semiconductor Physics, Quantum Electronics and Optoelectronics*, vol. 11, no. 2, pp. 257–265, 2008.

[22] B. L. Sheu, R. C. Myers, J. M. Tang et al., "Onset of ferromagnetism in low-doped Ga1-xMnxAs," *Physical Review Letters*, vol. 99, no. 22, Article ID 227205, 2007.

[23] J. Wallentin, J. M. Persson, J. B. Wagner, L. Samuelson, K. Deppert, and M. T. Borgström, "High-performance single nanowire tunnel diodes," *Nano Letters*, vol. 10, no. 3, pp. 974–979, 2010.

[24] J.P. Small, K.M. Perez, and P. Kim, "Modulation of thermoelectric power of individual carbon nanotubes," *Physical Review Letters*, vol. 91, no. 25, pp. 2568011–2568014, 2003.

[25] M. C. Llaguno, J. E. Fischer, A. T. Johnson, and J. Hone, "Observation of thermopower oscillations in the coulomb blockade regime in a semiconducting carbon nanotube," *Nano Letters*, vol. 4, no. 1, pp. 45–49, 2004.

[26] W. Liang, A. I. Hochbaum, M. Fardy, O. Rabin, M. Zhang, and P. Yang, "Field-effect modulation of seebeck coefficient in single PbSe nanowires," *Nano Letters*, vol. 9, no. 4, pp. 1689–1693, 2009.

[27] W. Paschoal Jr, S. Kumar, C. Borschel et al., "Hopping conduction in Mn ion implanted GaAs Nanowires," *Nano Letters*, vol. 12, no. 9, pp. 4838-4842, 2012.

[28] H. Ohno, "Making nonmagnetic semiconductors ferromagnetic," *Science*, vol. 281, no. 5379, pp. 951–956, 1998.

[29] A. Bentien, S. Johnsen, G. K. H. Madsen, B. B. Iversen, and F. Steglich, "Colossal seebeck coefficient in strongly correlated semiconductor $FeSb_2$," *Europhysics Letters*, vol. 80, no. 1, Article ID 17008, 2007.

Paper IV

NANO LETTERS

Letter

pubs.acs.org/NanoLett

Magnetic Polarons and Large Negative Magnetoresistance in GaAs Nanowires Implanted with Mn Ions

Sandeep Kumar,[†,■] Waldomiro Paschoal, Jr.,[†,‡,■] Andreas Johannes,[§] Daniel Jacobsson,[†] Christian Borschel,[§] Anna Pertsova,[∥] Chih-Han Wang,[⊥] Maw-Kuen Wu,[⊥,¶] Carlo M. Canali,[∥] Carsten Ronning,[§] Lars Samuelson,[†] and Håkan Pettersson[†,*,‡]

[†]Solid State Physics/The Nanometer Structure Consortium, Lund University, Box 118, SE-221 00 Lund, Sweden

[‡]Department of Mathematics, Physics and Electrical Engineering, Halmstad University, Box 823, SE-301 18, Halmstad, Sweden

[§]Institute for Solid State Physics, Friedrich-Schiller-University Jena, Max-Wien-Platz 1, D-07743 Jena, Germany

[∥]Department of Physics and Electrical Engineering, Linneaus University, SE-39233 Kalmar, Sweden

[⊥]Institute of Physics, Academia Sinica, Taipei, Taiwan

[¶]Department of Physics, National Donghwa University, Taiwan

ABSTRACT: We report on low-temperature magnetotransport and SQUID measurements on heavily doped Mn-implanted GaAs nanowires. SQUID data recorded at low magnetic fields exhibit clear signs of the onset of a spin-glass phase with a transition temperature of about 16 K. Magnetotransport experiments reveal a corresponding peak in resistance at 16 K and a large negative magnetoresistance, reaching 40% at 1.6 K and 8 T. The negative magnetoresistance decreases at elevated temperatures and vanishes at about 100 K. We interpret our transport data in terms of spin-dependent hopping in a complex magnetic nanowire landscape of magnetic polarons, separated by intermediate regions of Mn impurity spins, forming a paramagnetic/spin-glass phase.

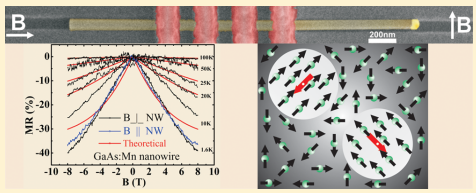

KEYWORDS: *Nanowires, ion-implantation, (Ga,Mn)As, spintronics, magnetic polarons, spin-glass, hopping transport, negative magnetoresistance*

The long-sought goal to engineer magnetic semiconductor systems on the nanometer scale poses challenges to understand magnetic properties and transport mechanisms in great detail at a fundamental level. Despite extensive studies, there is still a debate on the nature of ferromagnetic states in dilute magnetic III−V materials. Common models for (Ga,Mn)As alloys involve hole-mediated coupling of local magnetic Mn moments forming a ferromagnetic phase below a critical Curie temperature (T_C). The true nature of the states where holes provided by substitutional Mn reside, however, still remains controversial. Substitutional Mn has been proposed to strongly hybridize with the valence band states of GaAs,[1−3] or to form an impurity band[4−8] leading to the observed ferromagnetism through different exchange interactions.

Most theoretical and experimental studies so far have focused on dilute alloys with a sufficiently high concentration of Mn to achieve a high T_C.[1−8] More recently, there has been an increasing interest in semi-insulating semiconductor materials doped with magnetic elements.[9,10] Kaminski and Das Sarma[11] have proposed a magnetic polaron percolation model to explain the magnetotransport properties of dilute magnetic semiconductors (DMS) exhibiting a strong insulating character. This model assumes a heavily compensated material with both strongly localized charge carriers and a random spatial distribution of magnetic impurities. The strong exchange interaction between localized holes and magnetic impurities leads to the formation of bound spin-polarized magnetic polarons (BMPs). Yuldashev et al.[9] used this polaron model to estimate the critical concentration of holes required to form a ferromagnetic phase in (Ga,Mn)As thin films codoped with Te donors. It was demonstrated that an increased Te concentration (compensation) gradually reduces T_C, eventually replacing the long-range ordered ferromagnetic state with a paramagnetic-to spin-glass phase.

Dilute magnetic III−V nanowires (NWs) are fundamentally interesting not only for the expected new physics connected to their quasi-1D character but also because they can be monolithically integrated with silicon due to their small footprint.[12] Realizing (Ga,Mn)As NWs is thus an important step toward integration of spintronics with silicon in line with the "More than Moore" concept. ("More than Moore" implies new functionality added to conventional main-stream digital electronics beyond merely an increase in transistor density.)

Received: June 18, 2013
Revised: September 22, 2013
Published: October 4, 2013

ACS Publications © 2013 American Chemical Society

Because of low solubility of Mn in GaAs, it turns out to be extremely difficult to grow high-quality (Ga,Mn)As NWs with standard gas phase or molecular beam epitaxial techniques. Butschkow et al.[13] have studied the magnetotransport properties of core/shell NWs, which exhibit a different geometry than ours in that a thin ferromagnetic (Ga,Mn)As shell is grown around a nonmagnetic GaAs core at low temperature. These NWs exhibit a strong uniaxial anisotropy and a very pronounced negative magnetoresistance. The core/shell approach is an interesting way to circumvent the problem of growing (Ga,Mn)As NWs. Recently, we have reported on a different way to circumvent the growth problems by implanting the NWs with Mn ions after growth.[14] In this Letter, we report on magnetic properties and transport mechanisms in single-crystalline Mn-implanted GaAs NWs. Using electron beam lithography, we have fabricated contacts to individual nanowires facilitating well-controlled transport experiments. Combined with SQUID measurements on large ensembles of NWs, we present data consistent with spin-glass/paramagnetic nanowires involving bound magnetic polarons separated by intermediate unpolarized regions of Mn impurity spins.

The growth of NWs and subsequent Mn implantation were described previously.[15] Here, we summarize some key features along with improvements compared to our first implantation process described in ref 14. Single crystalline epitaxial GaAs NWs with 80 nm diameter and about 2 μm length were grown by MOVPE using monodisperse Au particles as catalysts. The NWs were grown on GaAs ⟨111⟩ substrates leading to perpendicular growth direction relative to the substrate. The NWs were implanted under an angle of 45° in respect to the nanowire axis with 100 keV Mn ions using a general purpose implanter (High Voltage Engineering Europa). The sample temperature was kept at 300 °C to facilitate efficient dynamic annealing during implantation. Using a Mn fluency of 1.8×10^{16} ions/cm^2 resulted in a total Mn concentration of about 2.5 atom % (corresponding to a stoichiometry of $(Ga_{1-x}, Mn_x)As$ with $x = 0.05$), confirmed by TEM/EDX. Figure 1 shows a two-dimensional (2D) plot of the predicted implanted Mn distribution in the NWs, numerically calculated using our own developed Monte Carlo "iradina" software.[16] From this modeling, we conclude that the distribution of Mn atoms in the NWs is expected to be fairly uniform using the implantation parameters described above. For transport measurements, NWs were mechanically transferred onto a silicon substrate covered by a 210 nm thick silicon dioxide layer on which reference markers and macroscopic metal pads were predefined. Prior to transferring of the NWs, trenches were etched in the SiO_2 layer to align the wires for magnetotransport studies. Electron beam lithography was used to define contacts connecting individual NWs to the macroscopic contact pads. The samples were treated in a HCl/H_2O solution for 15 s followed by a 2 min surface passivation in a heated (40 °C) NH_4S_x/H_2O solution. Low resistivity 4-point ohmic contacts to the nanowires were made by evaporation of Pd (10 nm)/Zn (10 nm)/Pd (35 nm) after passivation. The sample processing was finalized by a lift-off process. The magnetotransport measurements were performed in a Janis VariTemp superconducting cryomagnet system (Model 8T-SVM), with the magnetic field applied in the plane of the substrate (parallel or perpendicular to the NW as defined in the inset of Figure 2). For SQUID measurements, large ensembles of NWs ($\sim 5 \times 10^5$) were mechanically transferred to a Si/SiO_2 substrate. The magnetic properties were measured using a SQUID-VSM magnetometer manufactured by Quantum Design Corporation. The combination of SQUID and VSM technology provides superior sensitivity (standard deviation 10^{-8} emu) and fast measurement cycles. The magnetic field applied in the SQUID experiments was applied perpendicular to the substrate surface with randomly deposited NWs.

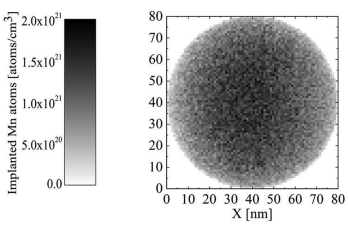

Figure 1. Cross-sectional plot of the simulated Mn distribution in a 80 nm NW implanted with 100 keV Mn^+ at an angle of 45° relative to the NW. The grayscale corresponds to a fluency of 1.8×10^{16} ions/cm^2, or a mean Mn concentration of 2.5%.

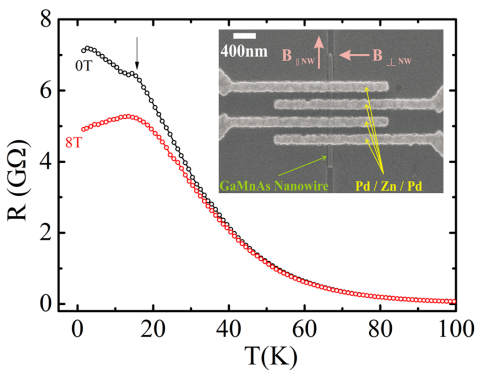

Figure 2. Magnetoresistance trace for a $(Ga_{1-x}Mn_x)As$ NW with x = 5% at 0 and 8 T, respectively. Arrow at 0 T trace indicates a transition from a high-temperature paramagnetic to low-temperature spin-glass phase. The local maximum observed in the 8 T trace possibly signals the onset of a weak ferromagnetic phase (see discussion in text). Inset shows an SEM micrograph of a NW with four electrodes for magnetotransport measurements.

Recently we have shown that Mn-implanted GaAs NWs are highly resistive even at room temperature.[15] The carriers (holes) are highly localized and Mott variable range hopping is the dominant transport mechanism at low temperatures. Figure 2 shows the temperature dependence of the resistance of a typical single NW. From the high resistance, it is evident that the hopping mechanism, associated with the overlap of wave function tails, indeed corresponds to a very low effective mobility. From the figure it is also evident that the resistance displays a small kink or shoulder at $T_C \sim 16$ K. A careful analysis of the curve shows that this feature is in fact a local maximum that was not observed in our previous studies,[14] most likely due to the use of thicker nanowires with less surface depletion in the present study. When a magnetic field of 8 T is applied, the

dx.doi.org/10.1021/nl402229r | Nano Lett. 2013, 13, 5079−5084

resistance at $T < 100$ K is typically smaller than the zero-field resistance. Interestingly, the resistance now exhibits a clear local maximum at the same temperature (T_C). The presence of a local maximum in the resistivity versus temperature in ferromagnetic metals and semiconductors is usually an indication of critical behavior and the temperature at which it occurs is identified with the Curie temperature. Its physical origin is scattering of carriers by spin fluctuations developing at the ferromagnetic transition. In the present case, this interpretation has to be confirmed with great care since our system is far from the metallic regime. The crucial quantity determining the transport properties of the sample is the effective hole concentration. A precise determination of this quantity is challenging, primarily due to uncertainties related to possible influence of surface depletion (leading to an effective channel width smaller than the NW diameter) and to unknown hole mobility. Estimates based on resistance measurements at room temperature,[15] as well as on thermoelectric measurements,[17] indicate that the effective hole concentration is less than 10^{18} cm^{-3}. This value is much smaller than the nominal Mn impurity concentration, estimated to be $\sim 10^{21}$ cm^{-3} for a 5% Mn-doped NW. The strong reduction of the hole concentration is most likely the result of compensation by remaining postimplantation point defects, such as Mn interstitials and As antisites.

The physical picture emerging from these considerations is the one of a system composed of relatively few quasi-localized holes, each surrounded by a large number of Mn impurities. In this regime, the possible onset of a ferromagnetic transition can be analyzed by means of a theoretical model of magnetic polarons, proposed by Kaminski et al.[11] According to this model, the exchange interaction between carriers (holes) and magnetic impurities leads to the formation of BMPs, consisting of individual localized holes surrounded by magnetic impurities, whose magnetic moment is antiferromagnetically coupled to the hole magnetic moment. The effective radius of a BMP is given by[11]

$$r_{\mathrm{pol}}(T) = \frac{a_{\mathrm{B}}}{2} \ln \frac{sS|J_0|}{k_{\mathrm{B}}T} \qquad (1)$$

where a_B is the Bohr radius of the hole, J_0 is the exchange energy between the magnetic ion and the localized hole, and T is the temperature. S and s are the absolute values of the impurity spin and hole respectively. Impurity spins that are not found inside a sphere of radius r_{pol}, centered at a localized hole, are essentially free. The radius of the BMP increases with decreasing temperature. When BMPs start to overlap, larger regions with the same magnetization orientation appear and eventually long-range ferromagnetic order can be established in the system via a percolation phase transition. The transition temperature will increase with the hole concentration n_h. More precisely, for a given value of n_h the condition for a magnetic percolation transition is given by

$$r_{\mathrm{pol}}(n_{\mathrm{h}})^{1/3} \approx 0.86 \qquad (2)$$

which expresses the simple fact that the average distance between two localized holes is approximately equal to the polaron radius. The critical temperature can be estimated from eq 1. In Figure 3, we plot the polaron radius as a function of temperature using eq 1 with $J_0 = 15$ meV, and $a_B = 1.39$ nm.[9] We can see that the polaron radius remains much smaller than the NW radius even at very low temperatures, justifying the use

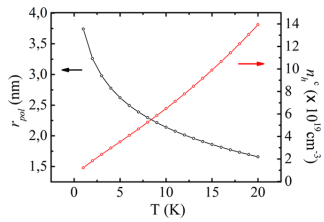

Figure 3. Black curve shows the theoretical estimate of the polaron radius obtained from eq 1. Red curve shows the critical hole density versus temperature, defined as the density satisfying the magnetic percolation transition condition given in eq 2 at a given temperature.

of the model by Kaminski et al. also for our quasi-1D systems. Figure 3 also shows the critical hole density, n_h^c, versus temperature that is the hole density satisfying eq 2 for a given temperature. This plot indicates quite definitely that the hole density required to trigger a magnetic percolation transition in the absence of an external magnetic field is much larger than the estimated hole density of the NWs for all accessible temperatures. In particular, the kink in the resistance observed at ~16 K can hardly be associated with a ferromagnetic transition. This conclusion is further supported by temperature-dependent zero-field-cooled (ZFC) and field-cooled (FC) magnetization measurements on large ensembles of NWs. Temperature-dependent ZFC and FC magnetization curves recorded at 3 mT are shown in Figure 4. In the temperature

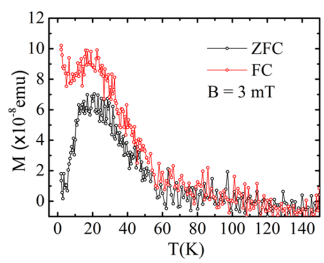

Figure 4. Temperature-dependent ZFC and FC magnetization curves of Mn implanted GaAs nanowire ensembles at an applied magnetic field of 3mT applied perpendicular to the substrate surface with deposited NWs.

range 20 K < T < 100 K, the magnetization is the same for both cases and it increases with decreasing temperature. Interestingly, the two curves start to diverge below 20 K and while the ZFC magnetization goes rapidly to zero the FC does not and in fact shows a hint of further increasing with decreasing temperature. Note that the peak in the ZFC curve occurs in the vicinity of the critical temperature where the resistance in Figure 2 exhibits a kink. We have also made the observation that the peak temperature (so-called blocking temperature) in ZFC curves decreases with increasing magnetic field strength. The divergence of FC and ZFC curves is less pronounced at increasing field strength, and completely vanishes at applied fields >20 mT.

This behavior is typically associated with a phase transition from a paramagnetic state to a spin-disordered or spin-glass

dx.doi.org/10.1021/nl402229r | Nano Lett. 2013, 13, 5079−5084

state in DMSs,[18] and it has been observed previously in semi-insulating $Ga_{1-x}Mn_xAs$ thin films.[9] In order to interpret this phenomenon, the BMP model must be somewhat modified[19] to the case of a very low hole concentration where the average distance between two localized holes, that is, distance between centers of two distinct adjacent polarons, is large. Clearly the radius of a BMP, containing magnetic impurities all aligned along the opposite direction of the hole spin, cannot increase indefinitely by decreasing T. Beyond a certain size L, the long-range exchange coupling between the hole spin and impurity spins far away from the polaron center becomes comparable to the relatively weaker direct exchange interaction between nearby impurities, which is typically antiferromagnetic. The interplay between these two competing interactions in the intermediate regions between magnetic polarons prevents the onset of long-range order and can result in a spin-disordered ground state. In this scenario, well-defined BMPs are still present, but they are separated by large intermediate unpolarized regions where the impurity spins at low-temperature freeze into a spin-glass-like state. Following ref 19, we can analyze the competition between the ferromagnetic and the spin-glass phase by introducing a parameter $P = (n_h^{1/3}a_B)/(n_i^{1/3}l)$, where l is the decay length of the antiferromagnetic interaction between magnetic impurities and n_i is the doping concentration. If $P \gg 1$, long-range ferromagnetic order is established via the magnetic percolation transition. On the other hand if $P \ll 1$, although magnetic polarons still form their interaction with the frustrated medium of magnetic impurity moments in the intermediate region leads to a spin-glass ground state. Using the estimates for the hole and impurity concentrations for the present NWs mentioned above, and further assuming l to be of the order of the impurity radius ~0.1 nm[19,20] and $a_B \sim 1.39$ nm, yields $P \leq 1$. These considerations support the picture of a ground state characterized by a spin-disordered phase. Note that in the presence of a strong magnetic field, the situation is different. This is already obvious from Figure 2, where the clear local maximum in resistance at 8 T indicates that the system is most likely in a phase close to ferromagnetic.

In the last part, we discuss magnetoresistance measurements and propose a phenomenological model that captures the experimental behavior remarkably well in the relevant temperature regime. The black and blue traces in Figure 5 show the temperature dependence of the magnetoresistance (MR) defined as $MR(\%) = [R(B,T) - R(0,T)]/[R(0,T)]$, where $R(B,T)$ is the resistance at magnetic field strength B and temperature T. Evidently, there is a remarkably large negative MR reaching 40% at 8 T with no hysteresis i.e. $R(B) = R(-B)$. We have studied six NW devices in great detail and they all display the same characteristic transport properties with a MR ratio between 40 and 50% and a kink/local resistance maximum at $T_C \sim 16$ K. MR data for magnetic fields applied perpendicular and parallel to a NW, respectively, display no significant differences as shown in Figure 5. The basic features of the negative MR curves plotted in Figure 5 can be understood in the context of the BMP model, which was used successfully in the first part of the paper to explain the observed transition to a spin disordered phase at low temperatures. Here, however, the magnetic polaron picture is adjusted to account for the presence of magnetic field and elevated temperatures. On the one hand, the BMP model suggests that as the applied magnetic field is increased, the magnetic moments of polarons successively become aligned with the field. This would facilitate an enhanced spin-dependent hopping between adjacent polarons, leading to a decrease of the resistance and hence to an increased MR as defined above. On the other hand, increasing the magnetic field also leads to an increased ordering of the random spin texture in the unpolarized region, which also enhances hopping from a polaron to a partially ordered intermediate site. Interestingly, the observed MR in our NWs is about 10 times larger than typically observed in metallic (Ga, Mn)As thin films,[21,22] pointing to strong spin-dependent scattering mechanisms involved in hopping transport in comparison to valence band transport. However, it is not obvious which of the possible mechanisms, for example, spin-dependent hopping between polarons whose magnetic moments align with field or hopping through partially ordered intermediate regions of Mn spins, provides the dominant contribution to the MR. Furthermore, both mechanisms are relevant for understanding the temperature dependence of the MR. Increasing the temperature causes progressive randomization of the orientation of magnetic polaron moments, in turn leading to a decreased MR. However, as the temperature is increased, the BMP radius decreases (see Figure 3) and therefore the intermediate regions between polarons become larger. Estimating the average number of Mn ions within the polaron volume shows that at temperatures above 16 K a typical polaron contains only a few Mn ions with the majority of impurity spins being in the intermediate region ($N_{Mn} \lesssim 4$ for $r_{pol} \approx 1$ nm taken as an average of the expression in eq 1 in the range 16 K < T < 100 K). The polaron radius is thus considerably smaller than the average separation between two polarons. This suggests that at elevated temperatures the paramagnetic behavior of Mn spins in the intermediate regions cannot be ignored.

We now propose a phenomenological model, incorporating the ideas above, which is able to capture the decrease of the resistance at finite magnetic fields and in addition provides insight into which mechanism is most likely responsible for the large negative MR. In the presence of magnetic field, the hopping of a hole is assumed to have an activation form

$$R \propto \exp\left(\frac{\Delta E}{k_B T}\right) \tag{3}$$

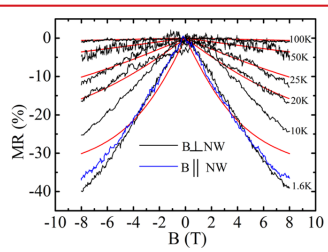

Figure 5. Magnetoresistance (black) traces recorded for a $(Ga_{1-x}, Mn_x)As$ NW with $x = 5\%$ with magnetic fields applied perpendicular to the NW (see inset of Figure 2 for definition of field directions). Red traces are theoretical MR curves calculated from eq 7 (10−100K). The blue trace shows the corresponding temperature dependence of the magnetoresistance with the magnetic field applied parallel to the NW (1.6 K).

dx.doi.org/10.1021/nl402229r | Nano Lett. 2013, 13, 5079−5084

where ΔE is the change of the hopping energy with magnetic field. We further postulate that ΔE is proportional to the interaction energy between the spin of the hole s and an average spin $\langle S_i \rangle$ of a magnetic object, which can represent a magnetic polaron or Mn ion in the unpolarized region. Since both mechanisms are relevant, we leave S, the spin angular momentum of the magnetic object, as a variable parameter in our model. Although the value of the interaction energy is also not known, we take it proportional to the only energy scale in our problem that is the exchange interaction between the hole and the magnetic object. To account for the presence of BMPs, we assume that the hopping distance might still be regulated by the effective hole (and indeed polaron) separation, and therefore ΔE will be proportional to n_h. The hopping event is also likely to be proportional to the typical interaction range of the hole wave function a_B. Finally, the average spin of the magnetic object in the presence of a magnetic field is given by

$$\langle S_i \rangle = S\mathcal{B}_S\left(\frac{Sg\mu_B B}{k_B T}\right) \tag{4}$$

where $\mathcal{B}_S\left(\frac{Sg\mu_B B}{k_B T}\right)$ is the Brillouin function and defined as[23]

$$\mathcal{B}_S\left(\frac{Sg\mu_B B}{k_B T}\right) = \frac{2S+1}{2S}\coth\left[\frac{2S+1}{2S}\left(\frac{Sg\mu_B B}{k_B T}\right)\right] - \frac{1}{2S}\coth\left[\frac{1}{2S}\left(\frac{Sg\mu_B B}{k_B T}\right)\right] \tag{5}$$

where S is the effective spin, $g = 2$ is the gyromagnetic ratio and μ_B is the Bohr magneton.

A possible form of ΔE is therefore

$$\Delta E = -A\frac{4\pi}{3}a_B^3 n_h J_0 s S\mathcal{B}_S\left(\frac{Sg\mu_B B}{k_B T}\right) \tag{6}$$

where A is constant. The resulting magnetic field dependence of the resistance is given by

$$R(B, T) = R(0, T)\exp\left(-\frac{A4\pi a_B^3 n_h J_0 s S}{3k_B T}\mathcal{B}_S\left(\frac{Sg\mu_B B}{k_B T}\right)\right) \tag{7}$$

In Figure 6 we show the result of fitting eq 7 to the measured resistance data for different values of the magnetic field. Interestingly, the best fitting for all relevant values of the magnetic field is obtained for $S = 5/2$ (spin of single Mn impurity) and $A \sim 2$. We also note that the fitting proposed here predicts that the decrease of the resistance as a function of field should saturate at $B \sim 20$ T. Furthermore, at 100 K all the MR signal has disappeared even in the presence of a magnetic field of 8 T. The fitting performs remarkably well in the temperature range roughly between 20 and 100 K but fails to predict the MR below 20 K where a glitch in the experimental data signals the aforementioned phase transition. Figure 6 suggests that above the spin-glass transition temperature, $R(B,T)$, can be described mainly by a paramagnetic state of magnetic impurities in the intermediate regions between BMPs, while below the transition temperature the system enters into a spin-glass state. In the presence of a strong magnetic field, the transition to a spin-glass state is transformed into a transition to a state that is most likely close to being ferromagnetic. This is brought about by the alignment of the impurity spins in the intermediate regions, as well as the magnetic moments of the polarons. Equation 7 can also be used to calculate the expected MR ratio versus magnetic field. In Figure 5, we include these MR curves at the corresponding temperatures. Evidently, there is a good agreement between experiment and theory for temperatures above 20 K. At lower temperatures, there is a significant deviation related to the phase transition discussed above.

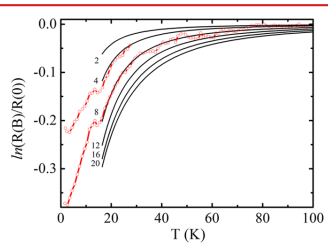

Figure 6. Red traces show experimental magnetoresistance ratios at 4 and 8T, respectively. Black lines are corresponding theoretical curves at different magnetic fields from 2 to 20T, calculated from eq 7.

In conclusion, we have performed magnetotransport measurements on single (Ga, Mn)As NWs. At $T < 100$ K, a large negative magnetoresistance associated with spin-dependent hopping transport is observed. In the absence of external field a spin-glass phase is formed below $T_C \sim 16$ K, as a result of the competition between the long-range hole-Mn and short-range Mn−Mn exchange interactions. When a strong magnetic field is present, the system below T_C is rather described by a phase close to being ferromagnetic. We interpret our transport data in terms of strongly spin-dependent hopping mechanisms involving magnetic polarons and large partially ordered intermediate regions of Mn impurity spins, forming a paramagnetic/spin-glass phase. Mn-implanted NWs represent an interesting novel type of nanometer-scale building blocks for miniaturized spintronic devices compatible with main-stream silicon technology.

AUTHOR INFORMATION

Corresponding Author

*E-mail: hakan.pettersson@hh.se.

Author Contributions

■S.K. and W.P. contributed equally to this work and are cofirst authors.

Notes

The authors declare no competing financial interest.

ACKNOWLEDGMENTS

The authors thank Magnus Borgström and Jesper Wallentin for help with providing GaAs nanowires and Maria Messing for TEM/EDX studies. Furthermore, the authors acknowledge financial support from nmC@LU, the Swedish Research Council (VR), the Knut and Alice Wallenberg Foundation, the Swedish National Board for Industrial, Technological Development, the Swedish Foundation for Strategic Research, the Nordforsk research network "Nanospintronics; theory and simulations", and the German Research Society (DFG) project Ro1198/14. One of the authors, W. P, gratefully acknowledges financial support from the Pará Education Secretary (SEDUC) and the Pará Government School (EGPA).

REFERENCES

(1) Dietl, T.; Ohno, H.; Matsukura, F.; Cibert, J.; Ferrand, D. *Science* **2000**, *287*, 1019.
(2) Neumaier, D.; Turek, M.; Wurstbauer, U.; Vogl, A.; Utz, M.; Wegscheider, W.; Weiss, D. *Phys. Rev. Lett.* **2009**, *103*, 087203.
(3) Masek, J.; Maca, F.; Kudrnovsky, J.; Makarovsky, O.; Eaves, L.; Campion, R. P.; Edmonds, K. W.; Rushforth, A. W.; Foxon, C. T.; Gallagher, B. L.; Novak, V.; Sinova, J.; Jungwirth, T. *Phys. Rev. Lett.* **2010**, *105*, 227202.
(4) Burch, K. S.; Shrekenhamer, D. B.; Singley, E. J.; Stephens, J.; Sheu, B. L.; Kawakami, R. K.; Schiffer, P.; Samarth, N.; Awschalom, D. D.; Basov, D. N. *Phys. Rev. Lett.* **2006**, *97*, 087208.
(5) Ando, K.; Saito, H.; Agarwal, K. C.; Debnath, M. C.; Zayets, V. *Phys. Rev. Lett.* **2008**, *100*, 067204.
(6) Dobrowolska, M.; Tivakornsasithorn, K.; Liu, X.; Furdyna, J. K.; Berciu, M.; Yu, K. M.; Walukiewicz, W. *Nat. Mater.* **2012**, *11*, 444.
(7) Rokhinson, L. P.; Lyanda-Geller, Y.; Ge, Z.; Shen, S.; Liu, X.; Dobrowolska, M.; Furdyna, J. K. *Phys. Rev. B* **2007**, *76*, 161201.
(8) Ohya, S.; Takata, K.; Tanaka, M. *Nat. Phys.* **2011**, *7*, 342.
(9) Yuldashev, Sh. U.; Jeon, H. C.; Im, H. S.; Kang, T. W.; Lee, S. H.; Furdyna, J. K. *Phys. Rev. B* **2004**, *70*, 193203.
(10) Sheu, B. L.; Myers, R. C.; Tang, J.-M.; Samarth, N.; Awschalom, D. D.; Schiffer, P.; Flatte, M. E. *Phys. Rev. Lett.* **2007**, *99*, 227205.
(11) Kaminski, A.; Das Sarma, S. *Phys. Rev. Lett.* **2002**, *88*, 247204.
(12) Krogstrup, P.; Popovitz-Biro, R.; Johnson, E.; Madsen, M. H.; Nygard, J.; Shtrikman, H. *Nano Lett.* **2010**, *10*, 4475.
(13) Butschkow, C.; Reiger, E.; Rudolph, A.; Geißler, S.; Neumaier, D.; Soda, M.; Schuh, D.; Woltersdorf, G.; Wegscheider, W.; Weiss, D. *Phys. Rev. B* **2013**, *87*, 245303.
(14) Borschel, C.; Messing, M. E.; Borgström, M. T.; Paschoal, W., Jr.; Wallentin, J.; Kumar, S.; Mergenthaler, K.; Deppert, K.; Canali, C. M.; Pettersson, H.; Samuelson, L.; Ronning, C. *Nano Lett.* **2011**, *11*, 3935.
(15) Paschoal, W., Jr.; Kumar, S.; Borschel, C.; Wu, P.; Canali, C. M.; Ronning, C.; Samuelson, L.; Pettersson, H. *Nano Lett.* **2012**, *12*, 4838.
(16) Borschel, C.; Ronning, C. *Nucl. Instrum. Methods, Sect. B* **2011**, *269*, 2133.
(17) Wu, P.; Paschoal, W., Jr.; Kumar, S.; Borschel, C.; Ronning, C.; Canali, C. M.; Samuelson, L.; Pettersson, H.; Linke, H. *J. Nanotechnol.* **2012**, *2012*, 480813.
(18) Oseroff, S.; Keesom, P. H. *Dilute Magnetic Semiconductors*; Academic: New York, 1988; p 73.
(19) Kaminski, A.; Galitski, V. M.; Das Sarma, S. *Phys. Rev. B* **2004**, *70*, 115216.
(20) Jungwirth, T.; Gallagher, B. L.; Wunderlich, J. In *Spintronics*; Dietl, T., Awschalom, D. D., Kaminska, M., Ohno, H., Eds.; Elsevier: Amsterdam, 2008.
(21) Matsukura, F.; Ohno, H.; Shen, A.; Sugawara, Y. *Phys. Rev. B* **1998**, *57*, R2037.
(22) Omiya, T.; Matsukura, F.; Dietl, T.; Ohno, Y.; Sakon, T.; Motokawa, M.; Ohno, H. *Phys. E* **2000**, *7*, 976.
(23) Kittel, C. *Introduction to Solid State Physics*, 8th ed.; Wiley: New York, 2004.

Paper V

Magnetoresistance in Mn ion-implanted GaAs:Zn nanowires

W. Paschoal Jr[1,2‡], Sandeep Kumar[1,2‡], D. Jacobsson[1], A. Johannes[3], V. Jain[1,2], C. M. Canali[4], A. Pertsova[4], C. Ronning[3], K. A. Dick[1,5] L. Samuelson[1] and H. Pettersson[1,2*]

[1]*Solid State Physics/The Nanometer Structure Consortium, Lund University, Box 118, SE-221 00 Lund, Sweden*

[2]*Dept. of Mathematics, Physics and Electrical Engineering, Halmstad University, Box 823, SE-301 18, Halmstad, Sweden*

[3]*Institute for Solid State Physics, Friedrich-Schiller-University Jena, Max-Wien-Platz 1, D-07743 Jena, Germany*

[4]*Department of Physics and Electrical Engineering, Linneaus University, SE-39233 Kalmar, Sweden*

[5] *Center for Analysis and Synthesis, Lund University, Box 124, S-221 00 Lund, Sweden*

Author Contributions

‡These authors contributed equally to this work and are co-first authors.

*Corresponding author: e-mail: hakan.pettersson@hh.se

Abstract

We have investigated the magnetoresistance (MR) in a series of Zn doped (p-type) GaAs nanowires implanted with different Mn concentrations. The nanowires with the lowest Mn concentration (~0.0001%) exhibit a low resistance of a few kΩ at 300K and a 4% positive MR at 1.6K, which can be well described by invoking a spin-split subband model. In contrast, nanowires with the highest Mn concentration (4%) display a large resistance of several MΩ at 300K and a large negative MR of 85% at 1.6K. The large negative MR is interpreted in terms of spin-dependent hopping in a complex magnetic nanowire landscape of magnetic polarons, separated by intermediate regions of Mn impurity spins. Sweeping the magnetic field back and forth for the 4% sample reveals a hysteresis that indicates the presence of a weak ferromagnetic phase. We propose co-doping with Zn to be a promising way to reach the goal of realizing ferromagnetic $Ga_{1-x}Mn_xAs$ nanowires for future nanospintronics.

Quasi-1D semiconductor nanowires (NWs) have gained great attention because of their interesting physical properties and potential application as building blocks for assembling functional integrated nanodevice systems[1]. NW-based electronic and photonic devices such as solar cells[2], light-emitting diodes and lasers[3,4], photodetectors[5] and transistors[6] have already been demonstrated. In current research, dilute magnetic semiconductor (DMS) nanostructures draw a lot of attention due to possible applications in spintronics and quantum information processing at the nanoscale[7]. In particular, theoretical studies concerning an increase in the Curie temperature (T_c) of $Ga_{1-x}Mn_xAs$ nanostructures have predicted that the long sought goal of spintronic devices operating at room temperature can be achieved[8]. Recently it was shown that the Curie temperature (T_C) of Mn-doped GaAs nanostrips could be enhanced to 200 K invoking nanostructure engineering[9], suggesting the possibility for nanowire-based spin devices to operate at higher temperatures compared to thin film counterparts. While several models, including carrier mediated exchange interactions[10] and bound magnetic polarons[11] (BMPs), have been proposed to explain the origin of ferromagnetism in semiconductor/insulator materials, the detailed physical mechanisms responsible for the ferromagnetic interaction are still under debate. The strong connection between hole concentration and ferromagnetism in thin $Ga_{1-x}Mn_xAs$ films has previously been demonstrated by several groups. Yuldashev *et al* reported on increased T_C in $Ga_{1-x}Mn_xAs$ films co-doped with Be acceptors to increase the hole concentration[12]. Modulation of the carrier density by an electric field[13] shows a similar direct correlation between hole concentration and change of T_C.

We have recently reported on fabrication of Mn-doped GaAs NWs by ion- implantation. Single-crystalline $Ga_{1-x}Mn_xAs$ NWs with a Mn composition of up to x=4% corresponding to 2.0 at.% have been realized by implanting at elevated temperatures to facilitate dynamic annealing[14,15]. GaAs NWs with high Mn content exhibit large resistance, even at room

temperature, resulting from strong hole compensation by defects, such as interstitial Mn as well as As antisites[15]. Since the ferromagnetic ordering depends strongly on the hole concentration, it appears promising to co-dope the NWs with additional acceptor impurites, such as Zn. Here we report on a series of synthesized single-crystalline p-type GaAs:Zn NWs implanted with Mn in a wide nominal concentration range from x = 0.0001% to 4%. The aim of the study is to investigate how co-doping with Zn influences the crystal quality, as well as the transport properties e.g. magnetoresistance (MR). In particular, we demonstrate that the MR can be tuned over a wide range from positive to large (85%) negative values. Moreover, NWs with 4% Mn exhibit a hysteresis when sweeping the magnetic field back and forth which signals the presence of a possible weak ferromagnetic ordering in the wires. We believe that the strategy of providing additional holes by in-situ acceptor doping is a very promising route towards the goal of realizing ferromagnetic GaAs nanowires.

Single-crystalline GaAs NWs of about 2 µm length and 90nm diameter were grown by metal-organic vapor phase epitaxy (MOVPE) using mono-disperse 80nm Au particles as catalysts and with trimethylgallium (TMGa) and arsine (AsH_3) as precursors. The NWs were grown on GaAs (111)B substrates leading to a perpendicular growth direction relative to the substrate. Prior to nucleation of the NWs, the samples were annealed in-situ at 650°C in an AsH_3/H_2 atmosphere to remove surface oxides. The NWs were grown with an initial nucleation step at 440°C for 1min with $\chi_{TMGa} = 6.49 \times 10^{-6}$ and $\chi_{AsH_3} = 2.2 \times 10^{-3}$. After the nucleation step, the supply of TMGa was closed and the temperature reduced to 400°C after which TMGa was reintroduced together with diethylzinc (DEZn) and HCl with molar fractions of 1.64×10^{-7} and 1.42×10^{-5}, respectively, to commence the growth of GaAs:Zn. The total growth time was 30min, after which the sample was cooled down in an AsH_3/H_2 atmosphere. The Zn concentration estimated from growth parameters, and confirmed by resistance measurements, on non-implanted NWs, amounts to about ~10^{19} cm^{-3} [16]. The as-

grown GaAs:Zn NWs were subsequently implanted on a rotating sample holder under an angle of 45° with respect to the NW axis with 40 keV Mn ions using a general purpose implanter (High Voltage Engineering Europa). The sample temperature was kept at 300°C to facilitate efficient dynamic annealing during implantation. A series of GaAs:Zn NWs were implanted with three different Mn ion fluencies of 2.65×10^{11} ions/cm^2 (sample I), 2.65×10^{14} ions/cm^2 (sample II) and 1.325×10^{16} ions/cm^2 (sample III) at 300°C, respectively, and subsequently kept at 300°C in vacuum for 12 hours after implantation. Results from computer simulations of the implanted ion profile using the *iradina* code[17] imply that the present implantation conditions lead to a fairly homogeneous concentration of x= 0.0001%, 0.1% and 4% Mn in $Ga_{1-x}Mn_xAs$ for samples I, II and III.

To assess the crystal structure and to verify the Mn content, NWs were broken off and transferred to a holey carbon grid and imaged with a JEOL 3000F transmission electron microscope (TEM). Figure 1(a) shows a low magnification TEM image of a typical NW from sample III, with less than 10 twin planes per µm. Figure 1(b) displays the corresponding diffraction pattern indicating an overall ZB crystal structure. The twin segments are responsible for the additional ZB diffraction spots. Between the few twin planes, the structure is pure ZB with no other polytype crystal structure as seen in the high resolution TEM image in Fig.1(c). X-ray energy dispersive spectroscopy (EDX) was carried out by switching to scanning TEM (STEM) mode with a probe size of 0.6nm. Overlaid on Figure 1(a) is a line scan of Ga (Kα), As (Kα) and Mn (Kα) signals along the full length of the NW. The signals are binned to a step size of 100nm to increase the signal-to-noise ratio. The average Mn content along the scan line is 1.9 (std. deviation 0.2) at% (stoichiometric $Ga_{0,96}Mn_{0,04}As$). In addition to the linescan, a map along 300nm and full width of the NW was recorded. From the map, blocks 200nm long and 7nm wide were used to calculate the Mn content using the Cliff-Lorimer algorithm. The width of the blocks were chosen to be larger than the beam

broadening (up to 3nm for the thickest part of the NW) within the sample and to give combined photon counts from Ga (Kα), As (Kα) and Mn (Kα) of at least 3500, which is enough to do quantitative calculations. A radially non-uniform Mn content was found with slightly higher Mn content close to the NW surface, as seen in Fig. 1(d). This slight non-uniformity, which stems from the use of a single ion energy in the implantation, agrees well with our *iradina* simulations. Additionally, a small decrease in As content is observed at the surface. Careful comparative analysis of the As distribution in as-grown GaAs NWs and annealed non-implanted reference NWs shows that the main reason for the As depletion in the implanted annealed NWs stems from selective sputtering of As versus Ga during implantation due to different surface binding energies. An additional smaller As surface depletion effect is caused by outgassing of As during the vacuum annealing and TEM investigations.

For transport measurements, implanted NWs were mechanically transferred onto a silicon substrate covered by a 210 nm thick silicon dioxide layer (SiO_2) on which reference markers and macroscopic metal pads were predefined. Prior to transferring of the NWs, trenches were etched in the SiO_2 layer to align the wires for magnetotransport studies. The transferred NWs are trapped inside the trenches, which are all located parallel or perpendicular to the applied magnetic field. Electron beam lithography (EBL) was used to define contacts connecting individual NWs to the macroscopic contact pads. An SEM image of a NW connected with electrodes is shown in Fig. 2(a). The samples were treated in HCl/H_2O solution for 20s, followed by a 2 min surface passivation in a heated ($40^{\circ}C$) NH_4S_x/H_2O solution. Low resistivity 4-point ohmic contacts to the nanowires were made by evaporation of Pd (2 nm)/Zn (30 nm)/Pd (63 nm) after passivation and finalized by a lift-off process. The magnetotransport measurements were performed in a Janis VariTemp superconducting cryomagnet system (Model 8T-SVM).

Figure 2(b) shows the current-voltage (I-V) characteristics for samples I, II and III measured in a four-probe configuration (see Fig. 2(a)) at room temperature. It is readily observed that the linear I-V observed for sample I with the lowest Mn concentration becomes strongly non-linear for higher Mn content (samples II and III). Moreover, sample I has a resistance R of ~500Ω, which increases to ~2 MΩ for sample III. The large resistance of sample III is comparable to the resistance of NWs without Zn doping investigated in our previous studies[15,18]. These results show that when the Mn concentration is much lower than the Zn concentration (sample I) there are enough holes in the NWs to sustain a high conductivity. As the Mn concentration becomes comparable to, or higher than the Zn doping (~10^{19} cm^{-3}), the NWs become highly resistive even at room temperature as observed for samples II and III. It is well known that heavily Mn-doped $Ga_{1-x}Mn_xAs$ thin films are strongly compensated with a residual free hole concentration of merely 10% of the nominal Mn concentration[10]. In the case of implanted NWs, we expect additional large potential fluctuations due to disorder and randomly distributed charged impurities leading to localization of holes, further increasing the resistance. Another possible reason for the unexpected high resistance in our co-doped NWs is the abovementioned depletion of As at the surface of the NWs due to sputtering which implies a high concentration of surface-near electrically active vacancies that increases the resistance.

Figure 3 shows the magnetoresistance (MR) of samples I,II and an unimplanted reference sample at 1.6K. The MR is defined as $MR(\%) = \frac{R(B)-R(0)}{R(0)} \times 100$, where $R(B)$ is the resistance at magnetic field B. Sample I displays a positive saturated MR~ 4 % at 4T with no hysteresis *i.e.* $R(B) = R(-B)$. A two-band model has been proposed to explain the origin of the positive MR in semiconductors[19,20]. Analysis based on such a model shows that the positive MR is given by[19]

$$\frac{\Delta R}{R_0} = \frac{A_1^2 B^2}{1+A_2^2 B^2} \quad . \qquad (1)$$

Here the parameters A_1 and A_2 are related to the conductivity and mobility of carriers in the two sub-bands. The MR described by Eq. (1) is quadratic at low fields, and saturates at high fields. The data for sample I fitted to Eq (1) is shown in Figure 3. In the present study, we attribute the two bands to a Zeeman-split impurity band, probably mixed with the heavy hole valence band, formed by the high Zn concentration (hole concentration ~ 10^{19}cm^{-3}). From temperature-dependent resistance measurements we conclude that the free holes do not significantly freeze out even at 1.6K at which kT<<30meV (binding energy of the Zn-related acceptor in GaAs). This observation is in agreement with previous studies on highly Zn-doped bulk GaAs[21], where the activation energy of hole emission from Zn acceptors was shown to strongly decrease with the concentration of Zn, and in fact found to disappear at degenerate concentrations. The field-induced change in population of the two sub-bands with different spin-dependent mobility and conductivity for majority and minority spin carriers leads to the observed positive MR. For sample II (0.1% Mn concentration), the MR increases with applied magnetic field without saturating even at 8T as shown in Fig. 3. Moreover, the resistance increases to about 2MΩ at room temperature due to compensation and localization of holes as discussed above. The charge transport is in this case governed by variable range hopping (VRH) mechanisms as we have reported earlier for Mn-implanted NWs without Zn co-doping[15]. At low temperatures, where hopping distances are large, a positive MR arises from magnetic compression of the wave functions of impurity states available for hole hopping events. This deformation of the wavefunctions leads to an effective increase of the hopping length, and thus to an increased resistance. The MR varies with magnetic field according to[22-24]:

$$\frac{R(B)}{R_0} = \exp(A \cdot B^{\gamma}), \qquad (2)$$

where A is a constant and γ=2 for low to moderate magnetic fields. The inset of Fig. 3 shows the MR of sample II plotted in a log-double log format. A quadratic dependence is readily observed up to B~4T. At higher magnetic field strengths, the MR displays a pronounced deviation towards a weaker (linear) field dependence. This trend of relaxed field-dependence was theoretically predicted in Ref. 22 (γ=0.6 at high fields) as well as in Ref. 24 (γ=0.25 at high fields). The small γ=0.25 was attributed to the role of intermediate scatterers, which effectively decrease the magnetic barrier caused by the magnetically deformed wavefunctions.

Interestingly, by increasing the Mn concentration to x=4%, we observe a drastic change from a modest positive MR to a very large negative MR (Fig. 4). For sample III, with the highest Mn concentration (~4%), the resistance decreases rapidly by about 50% at magnetic fields up to 1T. The resistance continues to decrease with increasing magnetic field, resulting in a more or less saturated negative MR of about 85% at 8T. The observed MR for heavily Mn-implanted Zn-doped GaAs NWs is almost twice as large as previously observed for NWs with similar Mn concentration but without Zn[18]. In contrast to the present samples, the MR for the previous Mn-implanted NWs without Zn did also not saturate even at 8T (compare present black MR trace to previous blue MR trace[18] in Fig. 4a). One interesting observation is that while the transport mechanism for sample II discussed above is also governed by hopping, the MR signatures are opposite. The basic features of the negative MR curves plotted in Fig. 4a can be understood in the context of the bound magnetic polaron (BMP) model proposed by Kaminski and Das Sarma[11], which was used successfully in our previous study to explain the observed MR at T>20K and the transition to a spin-disordered phase at lower temperatures[18]. This model assumes a heavily compensated material with both strongly localized charge carriers and a random spatial distribution of magnetic impurities. The strong exchange interaction between localized holes and magnetic impurities leads to the formation of bound spin-polarized magnetic polarons. The BMP model suggests that as the applied magnetic field

is increased, the magnetic moments of polarons, as well as the large partially ordered intermediate regions of Mn impurity spins[18], successively become aligned with the field. This alignment facilitates an enhanced spin-dependent hopping probability which leads to the observed negative MR. A comparison to sample II (positive MR), which in fact exhibits similar hopping lengths, points to the importance of magnetically active Mn-related hopping sites providing a negative MR, which strongly overcompensates the positive MR connected to magnetic compression of the wave functions.

In the absence of a magnetic field, the original BMP model proposed by Kaminski and Das Sarma[11] predicts a transition to a long-range ferromagnetic phase as the temperature is lowered, with the transition temperature governed by the hole concentration. In our previous work on Mn-implanted NWs without Zn co-doping[18] we developed a modified BMP model for the case of highly compensated samples. In particular, we showed that in these samples, due to insufficient hole concentration and competition between long-range and short-range exchange interactions in the intermediate regions between BMPs, the system most likely undergoes a transition to a spin-disordered phase with decreasing temperature. However, in the presence of a strong magnetic field and at very low temperatures, one might expect a weak ferromagnetic phase, and a signature of such a phase was indeed observed in the temperature dependence of the resistance at 8T, but, interestingly, no hysteresis effect was found. In the present NWs, we expect that the presence of additional holes due to the Zn co-doping can further strengthen the ferromagnetic behavior at large magnetic fields and low temperatures. Fig. 4b shows meticulous resistance measurements for perpendicular orientation of the magnetic field relative to the NW axis. A comparison between both sweep directions indeed reveals a small hysteresis. We thus interpret this important result in terms of a present weak ferromagnetic phase in the NWs.

In summary, we synthesized Mn-implanted GaAs NWs co-doped with Zn acceptors. The magnetoresistance changes from a small positive MR to a large negative MR (~85%) with increasing Mn concentration up to x=4%. The high Mn concentration also leads to a strong compensation of the hole concentration in the Zn-doped NWs, preventing the transition to fully ferromagnetically ordered NWs. Further studies of implantation and annealing strategies are required to resolve this issue. Nevertheless, the results presented here points to a possible route to successfully realize ferromagnetic $Ga_{1-x}Mn_xAs$ NWs of great potential for monolithic integration of III-V spintronics on silicon.

ACKNOWLEDGEMENTS

The authors acknowledge financial support from nmC@LU, the Swedish Research Council (VR), the Knut and Alice Wallenberg Foundation, the Swedish National Board for Industrial, Technological Development, the Swedish Foundation for Strategic Research, the Nordforsk research network "Nanospintronics; theory and simulations", and the German Research Society (DFG) project Ro1198/14. One of the authors, W. P. Jr, gratefully acknowledges financial support from the Pará Education Secretary (SEDUC) and the Pará Government School (EGPA).

REFERENCES

[1]L. Samuelson, Mater. Today **6,** 22 (2003).

[2]J. Wallentin, N. Antuu, D. Asoli, M. Huffman, I. Åberg, M. H. Magnusson, G. Siefer, P. Fuss-Kailuweit, F. Dimorth, B. Witzigmann, H. Q. Xu, L. Samuelson, K. Deppert, M. T. Borgström, Science **339**, 1057 (2013).

[3]M. H. Huang, S. Mao, H. Feick, H. Yan, Y. Wu, H. Kind, E. Weber, R. Russo, P. Yang, Science **292,** 1897 (2001).

[4]X. F. Duan, Y. Huang, R. Agarwal, C. M. Lieber, Nature **421,** 241 (2003).

[5]J. Wang, M. S. Gudiksen, X. Duan, Y. Cui, C. M. Lieber, Science **293,** 1455 (2001).

[6]C. Thelander, L. E. Fröberg, C. Rehnstedt, L. Samuelson, L. E. Wernersson, IEEE Electron Device Lett. **29,** 206 (2008).

[7]S. A. Wolf, D. D. Awschalom, R. A. Buhrman, J. M. Daughton, S. von Molna´r, M. L. Roukes, A. Y. Chtchelkanova, D. M. Treger, Science **294,** 1488 (2001).

[8]S. Sapra, D. D. Sarma, S. Sanvito, and N. A. Hill, Nano Lett. **2**, 605, (2002).

[9]L. Chen, X. Yang, F. H. Yang, J. H. Zhao, J. Misuraca, P. Xiong, S. von Molnár, Nano Lett. **11,** 2584(2011).

[10]H. Ohno, Science **281**, 951 (1998).

[11]A. Kaminski, S. D. Sarma, Phys. Rev. Lett. **88**, 247204 (2002).

[12]S. Yuldashev, H. Im, V. Yalishev, C. Park, T. Kang, S. Lee, Y. Sasaki, X. Liu, and J. Furdyna, Appl. Phys. Lett. **82**, 1206 (2003).

[13]D. Chiba, F. Matsukura, and H. Ohno, Appl. Phys. Lett. **89**, 162505(2006).

[14]C. Borschel, M. E. Messing, M. T. Borgström, W. Paschoal Jr., J. Wallentin, S. Kumar, K, Mergenthaler, K. Deppert, C. M. Canali, H. Pettersson, L. Samuelson, C. Ronning, Nano Lett. **11**, 3935 (2011).

[15]W. Paschoal Jr., S. Kumar, C. Borschel, P. Wu, C. M. Canali, C. Ronning, L. Samuelson, H. Pettersson, Nano Letters **12,** 4838 (2012).

[16]C. Gutsche, I. Regolin, K. Blekker, A. Lysov, W. Prost, F.J. Tegude, J App Phys **105**, 024305 (2009) .

[17]C. Borschel, C. Ronning, Nucl. Instr. Meth. B **269**, 2133 (2011).

[18]S. Kumar, W. Paschoal Jr., A. Johannes, D. Jacobsson, C. Borschel, A. Pertsova, C. H. Wang, M. K. Wu, C. M. Canali, C. Ronning, L. Samuelson, H. Pettersson, Nano Letters 13, 5079 (2013).

[19]R.P. Khosla, J.R. Fischer Phys. Rev. B, **2**, 4084(1970).

[20]S.M. Watts, S. Wirth, S. von Molnar Phys. Rev. B, **61**, 9621(2000).

[21]F. Ermanis and K. Wolfstirn J. Applied Phys. **37**, 1963 (1966).

[22] B. I. Shklovskii and A. L. Efros in *Electronic Properties of Doped Semiconductors*, edited by M. Cardona, P. Fulde and H-J Queisser, Springer, 1984.

[23] B. I. Shklovskii and B. Z. Spivak, in *Hopping Transport in Solids*, edited by M. Pollak and B. Shklovskii, Elsevier, 1991, p. 271.

[24] B. I.Shklovskii, Sov. Phys. Semicond. **17**, 1311 (1983)

FIGURES

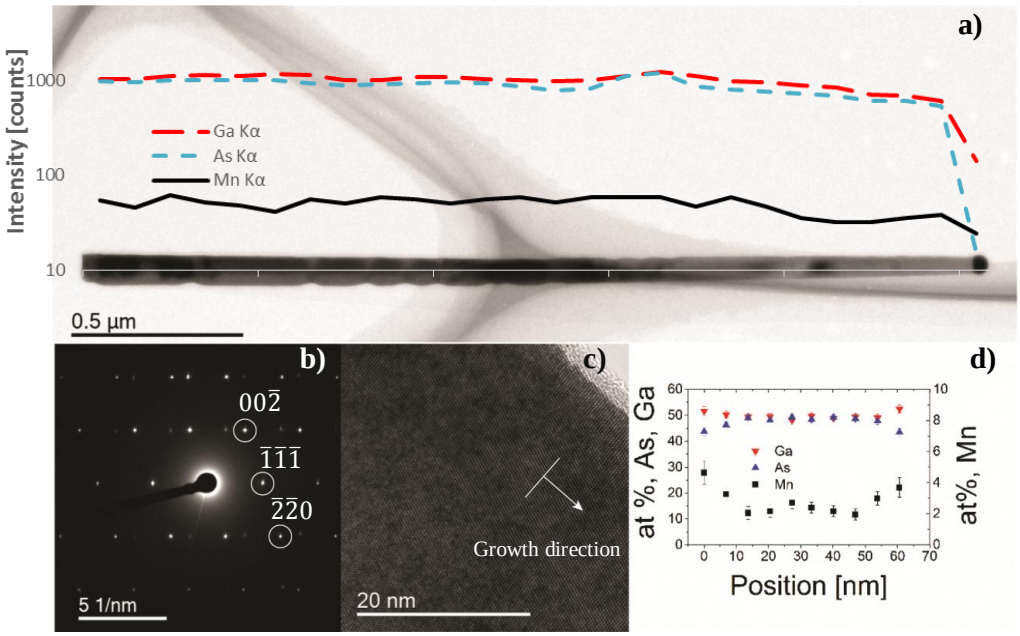

Figure 1: a) TEM image of a Mn-implanted NW with a nominal Mn composition of 4 %. An EDX line scan using the Ga(Kα), As (Kα) and Mn(Kα) peaks as references is inserted. The diffraction pattern in b) indicates a single-crystalline ZB structure with few twin planes. c) high-resolution TEM image and d) radial EDX line scans.

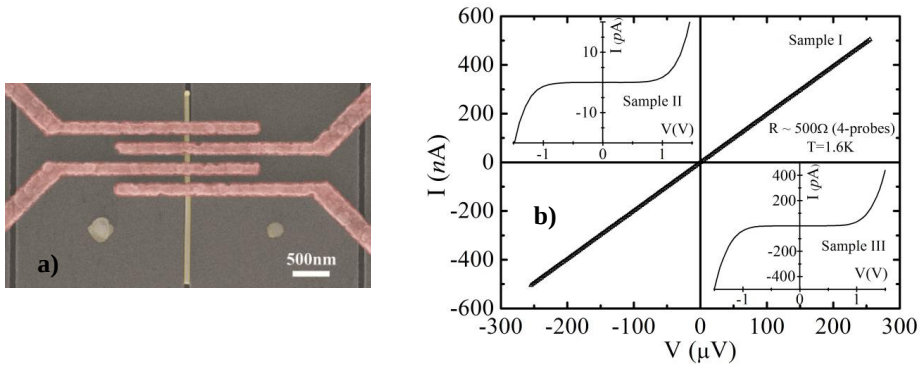

Figure 2: a) SEM image of a single NW provided with contacts for 4-probe measurements. b) Current-voltage (I-V) characteristics of Mn-implanted GaAs:Zn NWs. Main figure displays data for sample I, while corresponding data for samples II and III are shown as upper left and lower right inserts, respectively. T=1.6K.

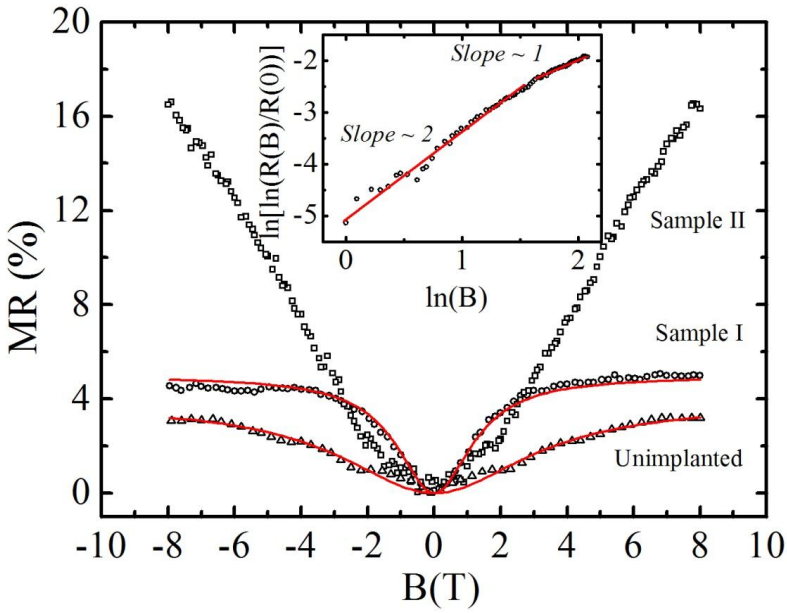

Figure 3: MR curves for sample I, II and an unimplanted reference sample at 1.6K. Black circles are the experimental data, while the red lines are theoretical fittings using Eq. (1). Inset shows a log-double log plot of the resistance versus magnetic field for sample II, clearly showing a quadratic dependence at low field strengths.

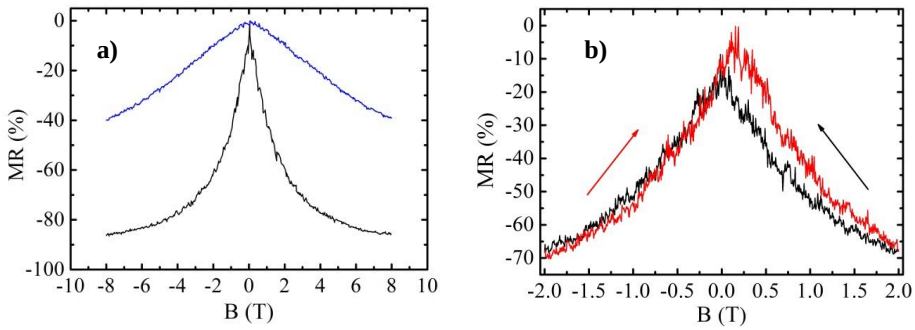

Figure 4: a) MR curve for sample III (black trace) plotted together with data for a 5% Mn-implanted GaAs NW without Zn (blue trace, data taken from Ref.18). b) Detailed MR curves for sample III in a) for two sweep directions (red trace: -2T→2T, black trace: 2T→ -2T) revealing a weak hysteresis. All MR curves are taken with the magnetic field perpendicular to the NW. T= 1.6K.